**Title**
Hemodynamics: From Developmental Mechano-transduction to Vascular Injury and Regeneration



**Author**
Baek, Kyung In

**Publication Date**
2019

Peer reviewed|Thesis/dissertation

UNIVERSITY OF CALIFORNIA

Los Angeles

# Hemodynamics: From Developmental Mechano-transduction to Vascular Injury and Regeneration

A dissertation submitted in partial satisfaction of the

requirements for the degree Doctor of Philosophy in Bioengineering

by

Kyung In Baek

2019

ABSTRACT OF THE DISSERTATION

**Hemodynamics: From Developmental Mechano-transduction to Vascular Injury and Regeneration**

by

Kyung In Baek

Doctor of Philosophy in Bioengineering

University of California, Los Angeles, 2019

Professor Tzung Hsiai, Chair

**Abstract**

Hemodynamic shear force is an important determinant of cardiovascular function and development. While mammalian models combined with next regeneration sequencing are essential for diagnosis and drug discovery, zebrafish has emerged as an important developmental model that combines *in vivo* analyses of cardiovascular phenotypes and the advantages of forward and reverse genomic engineering. The following studies in this thesis utilize an advanced imaging-based technique to characterize hemodynamic regulation in cardiovascular development and regeneration in embryonic zebrafish. Cardiogenesis involves a series of complex signaling pathways, while imaging cellular dynamics including cardiac trabeculation requires high spatiotemporal resolution. By using four-dimensional light-sheet fluorescent microscopy, we constructed four-dimensional moving domain models of the contracting myocardial

wall to investigate hemodynamic regulation of endocardial Notch signaling in facilitating cardiac trabeculation. *In vivo* modulations of hematopoiesis and atrial contraction, or ectopic expressions of Notch Intracellular Cytoplasmic Domain (NICD), suggested distinct flow patterns in myocardial geometry differentially activate endocardial Notch activity for trabecular organization and contractile function. Vascular disorders characterized by ischemic reperfusion injury, such as stroke, myocardial infarction, and peripheral vascular disease, remain the most frequent causes of incapacitating disease and death. Despite numerous efforts, structural and functional vessel recovery remains challenging, while molecular events underlying vascular injury and regeneration are largely unknown. A plethora of epidemiological studies consistently support a link between redox active ultrafine particles (UFP, *diameter* < 0.1 μm) in primary pollutants and cardiopulmonary disease. Due to the small size and the light weight of the particle, aspiration of UFP allows for penetration of pulmonary systems as well as the endothelial barrier. Once particles enter the circulatory system, they systematically affect endothelial homeostasis by promoting vascular oxidative and inflammatory responses. However, epigenetic and pathological effects underlying vascular regeneration upon particle exposure remains elusive. For the second part of this thesis, we investigated the importance of the Forkhead Box Sub-family O1 (FOXO1)/Notch activation complex upon UFP exposure in vascular regeneration. Finally, our vascular protective metabolomic profiles suggested hemodynamic shear forces is a central player in modulating the expression levels of glycolytic metabolites. In this context, we investigated the Vascular Endothelial Growth Factor Receptor (VEGFR)-Protein Kinase C isoform epsilon (PKCε) pathway and its role in promoting pro-glycolytic metabolites to help facilitate vascular regeneration.

The dissertation of Kyung In Baek is approved.

Dino Di Carlo

Stephanie Kristin Seidlits

Thao Phuong Nguyen

Paivi Elisabeth Pajukanta

Tzung Hsiai, Committee Chair

University of California, Los Angeles

2019

## DEDICATION

This dissertation is dedicated to my father, Dr. Sung Uhn Baek, my mother Dr. Hae Young Lee, my sister Soyae Baek, and my wife Jamie Jung Yoo.

## ACKNOWLEDGEMENT

First, I would like to give express my gratitude to Mrs. Heather Joanne Palmer at University of Utah. Studying abroad in the United States to achieve a higher level of education was not an easy task. Back then, I remember one of the challenges I faced was definitely limited cultural adaptation and difficulty digesting highly advanced content while simultaneously learning English. Mrs. Palmer was instrumental in developing my career skillset and improving my proficiency in English. Without her utmost support and love, it would have been very challenging to overcome obstacles to finish my undergraduate education, and I would not have been able to achieve what I have done at both University of Utah and UCLA. My interest in pursuing biomedical science and engineering was first inspired by my undergraduate scientific training under the mentorship of Dr. Gang Liu and Dr. Ping Men at the University of Utah. Under their guidance, I was able to build a foundation of molecular biology and biochemistry with pragmatic applications. They were always patient with my scientific progress and provided absolute support in pursuing graduate studies. I am grateful for their devotion in science and unfailing endeavor to advance the life-long career of their student. I would like to also show appreciation to those with whom I work with today. Dr. Yuchong Tai at California Institute of technology, a leader in sensor fabrication. His energy in communication and academic performance has been always inspirational. Dr. Linda Demer and Dr. Yin Tintut have been the source of inspiration and have always been supportive in my grant writing by serving as my professional references. Their heartwarming consultations made my Ph.D. training fruitful. In addition, I would like to give special thanks to those who serve on my committee for their efforts and energy : Drs. Stephanie Seidlits, Thao P. Nguyen, Dino Di Carlo and Paivi Pajukanta. Their leadership

and scientific advisory during my oral qualification exam shaped my focus in research. Their exciting and productive research work is truly inspirational. I am also grateful to have wonderful lab mates. Dr. Rene Packard is a talented researcher and has been a leader and amazing consultant. His contribution to science and his enthusiasm truly inspired me to pursue my long-term goals in academia. Dr. Jeffrey J. Hsu is a brilliant physician scientist. His mentorship to medical students and junior STAR fellows has been instrumental for leadership. Despite a busy schedule as a chief STAR fellow in cardiology, Jeff further provided unconditional support in scientific presentations and writing manuscripts. I appreciate Jeff for his friendship and for being a wonderful scientist in our lab. I cannot imagine how lucky I am to have met Dr. Yichen Ding and Chih-Chiang Chang. Not only are they specialists in physics and optical engineering, but they have also been my good friends. Their kindness and devotion to the whole lab is the core of the Hsiai Lab. My fellow Ph.D. candidates, Roy Chen, Mehrdad Roustaei, Zhaoqiang Wang and Cynthia Chen have been superb in research. Their dedications in molecular biology, optical imaging, computational biology and fluid dynamics were highly motivating to me. Our former lab members, Drs. Nelson Jen, Tyler J. Beebe, Juhyun Lee and Rongsong Li have been good mentors and friends, and they helped me learn how to conduct molecular biology experiments through their instruction on experimental design. Their fundamental contribution to science has led me to where I am at today. Further, I want to show my highest gratitude to my advisor Dr. Tzung K. Hsiai. His interest in collaborative research, communications skills and amazing performance in grant writing have been inspirational to me and have become my milestone for my life-long goal.

Finally, I wish to express my love and gratitude to my family. My father, Dr. Sung Uhn Baek, has been a general surgeon with a specialty in colorectal surgery for decades. Although he is close to retirement, he is still very active in both his clinic and his research. His dedication to his work throughout his life taught me the value of being humble and passionate. My mother, Dr. Hae Young Lee, has been my biggest supporter. Her unconditional love has driven me to become altruistic. My brilliant sister, So Yae Baek, has always brought vitality to my family. Last but not least, I would like to thank my wife, Jamie Yoo, for shining her light on me, and I cannot wait to see what awaits us in the next chapter of our lives.

## TABLE OF CONTENTS

**CHAPTER III. ULTRAFINE PARTICLE EXPOSURE REVEALS THE IMPORTANCE OF FORK HEAD BOX SUBFAMILY O1 / NOTCH ACTIVATION COMPLEX FOR VASCULAR REGENERATION**



**CHAPTER IV. FLOW-RESPONSIVE VASCULAR ENDOTHELIAL GROWTH FACTOR RECEPTOR-PROTEIN KINASE C ISOFORM EPSILON SIGNALING MEDIATED GLYCOLYTIC METABOLITES FOR VASCULAR REPAIR**

## LIST OF FIGURES

### CHAPTER I

## LIST OF TABLES

## CURRICULUM VITAE

### EDUCATION

**2010-2014** University of Utah
Salt Lake City, Utah
Bachelors of Science in Biomedical Engineering

### PROFESSIONAL SOCIETIES

**2015-Present** American Association of Anatomist (AAA)
**2016-Present** American Heart Association (AHA)
**2016-Present** Biomedical Engineering Society (BMES)
**2017-Present** Arteriosclerosis, Thrombosis, and Vascular Biology (ATVB)
**2017-Present** North American Vascular Biology Organization (NAVBO)

### RELATED PUBLICATIONS

Lee J, Fei P, Sevag Packard RR, Kang H, Xu H, **Baek KI**, Jen N, Chen J, Yen H, Kuo CC, Chi NC, Ho CM, Li R, Hsiai TK. 4-dimensional light-sheet microscopy to elucidate shear stress modulation of cardiac trabeculation. *The Journal of clinical investigation*. 2016;126:3158

Li R, Yang J, Saffari A, Jacobs J, **Baek KI**, Hough G, Larauche MH, Ma J, Jen N, Moussaoui N, Zhou B, Kang H, Reddy S, Henning SM, Campen MJ, Pisegna J, Li Z, Fogelman AM, Sioutas C, Navab M, Hsiai TK. Ambient Ultrafine particle ingestion alters gut microbiota in association with increased atherogenic lipid metabolites. *Scientific reports*. 2017;7:42906

Lee J[#], Chou T[#], Kang D, Kang H, Chen J, **Baek KI**, Wang W, Di Carlo D, Tai YC, Hsiai TK. A Rapid Capillary-Pressure Driven Micro-Channel to Demonstrate Newtonian Fluid Behavior of Zebrafish Blood at High Shear Rates. *Scientific Reports.* 2017; 7:1980

Sevag Packard RR, **Baek KI**, Beebe T, Jen N, Ding Y, Shi F, Fei P, Kang BJ, Chen PH, Gau J, Chen M, Tang J, Shih YH, Ding Y, Li D, Xu X, Hsiai TK, Automated Segmentation of Light-Sheet Fluorescent Imaging to Characterize Experimental Doxorubicin-Induced Cardiac Injury and Repair, *Scientific Reports*. 2017; 7:8603

Chang SS, Tu S, **Baek KI**, Pietersen A, Liu YH; Savage V, Hwang SP, Hsiai TK; Roper M, Optimal occlusion uniformly partitions red blood cells fluxes within a microvascular network, *PLOS Computational Biology.* 2017; 13: e1005892

Ding Y, Abiri A, Li S, Abiri P, Lee J, Chang CC, **Baek KI**, Sideris E, Li E, Bui A, Segura T, Nguyen TP, Packard RS, Fei P, Hsiai TK. Integrating light-sheet imaing with virtual reality to recapitulate developmental cardiacs, *Journal of Clinical Investigation Insight.* 2017; 2: e97180

**Baek KI,** Li R, Jen N, Choi H, Kaboodrangi A, Ping P, Liem D, Beebe T, Hsiai TK. Flow-

Responsive VEGFR-PKCε Signaling Mediates Glycolytic Metabolites for Vascular Repair, *Antioxidant & Redox Signaling.* 2018; 28: 31-43 (Cover page)

**Baek KI,** Sevag Packard RR, Hsu J, Saffari A, Ma Z, Luu A, Pietersen A, Yen H, Ding Y, Ren B, Sioutas C, Li R, Hsiai TK, Exposure to Ultrafine Particles Reveals the Importance of FOXO1/Notch Cooperation to Restore Vascular Regeneration, *Antioxidant & Redox Signaling*. 2018; 28: 1209-1223 (Cover page)

Ding Y, Lee J, Hsu JJ, Chang CC, **Baek KI**, Ranibarvaziri S, Ardehali R, Packard RS, Hsiai TK, Light-sheet Imaging to elucidate Cardiovascular Injury and Repair, *Current cardiology report.* 2018; 20:35

Messerschmidt V, Bailey Z, **Baek KI**, Bryant R, Li R, Hsiai TK, Lee J. Light-sheet Fluorescence Microscopy to Capture 4-Dimensional Images of the Effects of Modulating Shear Stress on the Developing Zebrafish Heart. *Journal of Visualized Experiments,* 2018

**Baek KI**[#], Ding Y[#], Chang CC[#], Packard RRS, Hsu JJ, Chang M, Fei P, Hsiai TK. Application of Light-Sheet Fluorescence Microscopy in Zebrafish Models of Cardiovascular Injury and Regeneration, *Progress in Biophysics and Molecular Biology*, 2018 ([#] **equally contributed to this work**)

Lee J[#], Vedula V[#], **Baek KI**[#], Chen J, Hsu JJ, Ding Y, Chang CC, Kang H, Small A, Fei P, Choung CM, Li R, Packard RS, Marsden AL, Hsiai TK, Spatial and Temporal Variations in Hemodynamic Forces Regulate Cardiac Trabeculation: Implication for Ventricular Contraction, *Journal of Clinical Investigation Insight*. 2018 ([#] **equally contributed to this work**)

Li R, **Baek KI**, Chang CC, Zhou B, Hsiai TK. Mechanotransduction in the Zebrafish Model in Cardiovascular Development and Regeneration, *Pan publishing group*, 2018 (Book Chapter)

Hsu JJ, Vedula V, **Baek KI**, Chen C, Chou MI, Lam J, Subhedar S, Lee J, Ding Y, Demer LL, Tintut Y, Marsden AL, Hsiai TK, Coordination between Contractile and Hemodynamic Forces in Notch1b-mediated Outflow Track Valve Morphology, *Journal of Clinical Investigation Insight*. 2019

**Baek KI**, Chang CC, Chang SS, Roper M, Li R, Hsiai TK, Non-newtonian flow activates endothelial Notch-ephrinb2/Ephb4 axis to promote vascular regeneration, 2019, (*In preparation*)

# CHAPTER I

## SPATIAL AND TEMPORAL VARIATIONS IN HEMODYNAMIC FORCES INITITATE CARDIAC TRABECULATION

Lee J*, Vedula V*, Baek KI*, Chen C, Hsu JJ, Ding YC, Chang CC, Kang H, Small A, Fei P, Choung CM, Li R, Demer L, Packard RS, Marsden AL, Hsiai TK

* Equal Contribution

Original article, published in ***Journal of Clinical Investigation Insight***, 2018 July 12, 8;3(13):e96672

## Introduction

Biomechanical forces intimately influence cardiac morphogenesis [1]. During development, the myocardium differentiates into two layers, an outer compact zone and an inner trabeculated zone. In response to hemodynamic shear stress [2], Notch receptor-ligand interaction is implicated in the initiation and organization of trabeculation [3, 4]. Both trabeculation and compaction are essential for normal contractile function during cardiac development [5-8]. A significant reduction in trabeculation is associated with ventricular compact zone deficiencies (hypoplastic wall), whereas hypertrabeculation is associated with left ventricular non-compaction cardiomyopathy (LVNCC) [9, 10]. The former condition predisposes patients to heart failure with depressed ejection fraction (EF), and the latter to heart failure with preserved EF and arrhythmia [11, 12]. LVNCC is the third most common cardiomyopathy after dilated and hypertrophic cardiomyopathy in the pediatric population [13]. Its prevalence was estimated at 4.5 to 26 per 10,000 adult patients referred for echocardiographic diagnosis [13, 14]. During cardiac morphogenesis, the initial site of endocardial protrusion into the cavity occurs at the site of flow impingement directly opposite the atrioventricular (AV) valve, leading to elevated WSS and thus providing a mechanotransductional basis to link shear stress with trabeculation [5]. Ventricular trabeculation produces a complex network of muscular ridges and grooves. Although Notch signaling activated by blood flow and cardiac contraction have been reported previously, the detailed mechanisms by which spatial and temporal variations in wall shear stress (WSS) coordinate this process are not yet known [7, 15].

Several molecular pathways for trabeculation have been found to regulate cardiomyocyte proliferation and differentiation [16-18]. Mutations in Notch signaling pathways result in congenital heart defects in humans and other vertebrates [19]. Using RBPJ-k and Notch1

mutants, Grego-Bessa *et al.* and others demonstrated that the Notch-EphrinB2-Nrg1-ErbB2 pathway initiates differentiation of trabeculation [5, 16, 17]. We further demonstrated that hemodynamic shear forces mediate endocardial Notch-Nrg1-ErbB2 signaling, which promotes contractile function [7, 20].

To spatially and temporally characterize endocardial WSS during cardiac morphogenesis in this study, we integrated advanced light-sheet imaging with 4-D computational fluid dynamics (CFD) to elucidate the mechanotransduction underlying the formation of trabecular ridges and grooves. We hypothesized that spatial ($\partial\tau/\partial x$) and temporal variations ($\partial\tau/\partial t$) in WSS modulate endocardial Notch signaling to drive formation of trabecular ridges and grooves for optimal ventricular contractile function during development. Using light-sheet fluorescence microscopy (LSFM) for rapid image acquisition and high-axial resolution, together with moving-domain CFD, we determined the hemodynamic forces across the AV valve and at the site of impingement on the opposing wall where the endocardial trabecular ridges first form in live zebrafish embryos. Results quantify the biomechanical forces underlying the initiation of trabeculation [5]. 4-D CFD simulations revealed pulsatile shear stress (PSS) along the trabecular ridges and oscillatory shear stress (OSS) in the grooves during trabeculation. Accompanying gain- and loss-of-function experimental analyses corroborated sequential upregulation of Notch activity from the endocardium to the trabecular grooves, resulting in cardiomyocyte proliferation. The oscillatory shear index (OSI), defined as the extent of oscillation of the direction of wall shear stress vector at any point on the ventricular wall during the cardiac cycle, was elevated in the trabecular grooves in association with prominent Notch activity.

Genetic manipulations to reduce endocardial WSS attenuated trabeculation and Notch activity [5, 7, 21, 22]. Furthermore, our *in silico* simulation predicted that ventricular trabeculation promotes kinetic energy (KE) dissipation, whereas non-trabeculated ventricle lacks KE dissipation, resulting in ventricular remodeling and contractile dysfunction. Thus, the integration of advanced light-sheet imaging with 4-D computation and zebrafish genetics demonstrate that spatiotemporal variations in WSS modulate Notch activity to coordinate the initiation of trabecular ridges and grooves, with physiological implications in optimizing cardiac structure and function during cardiac development.

## Methods

### Zebrafish Embryos

Zebrafish were bred and maintained at the UCLA Zebrafish Core Facility, and experiments were performed in compliance with UCLA IACUC protocols [48]. Transgenic *Tg(cmlc2:gfp)* and *Tg(;tp1:gfp;cmlc2:mCherry*) zebrafish lines were used under the following conditions: **1)** control (wild type), **2)** *gata1a* MO, and **3)** AG1478 treated groups [29]. *Gata1a* MO reduced hematopoiesis and blood viscosity by 90% as previously reported [21, 26]. *Wea* (courtesy of Dr. Deborah Yelon, UCSD, La Jolla, CA) were used to inhibit the development of atrioventricular gradients. FUCCI (fluorescent Ubiquitylation-based cell cycle indicator) zebrafish (courtesy of Dr. Ken Poss, Duke University, Durham, NC) was used to visualize the number of cardiomyocyte proliferation for each condition. The two transgenic lines used in the FUCCI system were *Tg(cmlc2:mCherry)* and *Tg(cmlc2:Venus-hGeminin)*$^{pd58}$. To maintain transparency of zebrafish embryos, we added 0.003% phenylthiourea (PTU) in E3 medium to suppress pigment formation at 10 hours post fertilization (hpf).

## 4-D Cardiac SPIM Imaging with Synchronization Algorithm

We integrated our in-house 4-D LSFM imaging system with post-processing synchronization to visualize dynamic ventricular motion in the embryos [7, 35, 49, 50]. By LSFM, we scanned *in vivo* zebrafish hearts from the rostral to the caudal end. Each section was captured with 500 x-y planes (frames) at 10 ms exposure time (100 frames per second) via a sCMOS camera (Hamamatsu Photonics, ***Hamamatsu*** City, Japan). The thickness of the light-sheet was tuned to 5 μm to provide a high axial (Z-axis) resolution for adequate reconstruction of the 4-D cardiac image, and the Z-step was set to 2 μm for lossless digital sampling according to the Nyquist sampling principle [34]. To synchronize with the cardiac cycle, we determined the cardiac periodicity on a frame-to-frame basis by comparing the pixel intensity from the smallest ventricular volume during peak systole to the largest volume during end-diastole [33, 35]. The reconstructed 4-D images were processed using Amira software (Berlin, Germany).

## Computational Modeling

The reconstructed 4-D zebrafish images were processed to extract the wall motion of a beating zebrafish ventricle. A detailed account of the computational modeling framework from zebrafish images to blood flow simulation and wall shear stress computation was presented in Vedula *et al* [22]. Briefly, 3-D images at mid-diastole were segmented using 3-D level set segmentation in SimVascular (http://www.simvascular.org) to create a triangulated surface of the ventricle. Next, to extract ventricular motion, we used an efficient non-rigid deformable B-spline-based image registration [36] with a source image (e.g. at mid-diastolic phase) registered to a target image (e.g. at end-diastole) by

minimizing a similarity function. A cubic B-spline transformation was used to deform the control points on the source image during registration. A Laplacian-based smoothing operator weighted by a regularization coefficient was added to the similarity function to ensure that the deformations were smooth and non-intersecting. These deformations were used to morph the initial segmented surface to extract the motion of the ventricle. A tetrahedral volume mesh was then created using TetGen (http://wias-berlin.de/software/tetgen/) open source meshing library that is integrated into SimVascular.

**Moving Domain CFD Modeling**

A detailed description of the methodology to perform moving domain CFD modeling in zebrafish embryos is provided in Lee *et al.* and Vedula *et al.* Briefly, the individual developmental stages were captured using SPIM technique and the video frames were processed using ImageJ (National Institutes of Health, Bethesda, MD, USA) [4, 22]. We performed image segmentation using 3-D level set methods in the SimVascular open source software at one selected cardiac phase to extract the ventricular morphology [51]. The endocardial surface in direct contact with the blood was subsequently extracted as a triangulated surface. The extracted surface was further processed for segmentation related artifacts such as hole filling, smoothing, extrusion, and surface remeshing in MeshMixer (Autodesk Research Inc.). We then employed a non-rigid deformable image registration technique to extract the motion of the endocardial boundary [22, 52]. In this approach, a source image (e.g. at end-systolic phase) is registered to a target image (for e.g. at end-diastole) by minimizing a similarity function. A cubic B-spline transformation is used to deform the control points on the source image during registration. A Laplacian

based smoothing operator weighted by a regularization coefficient is added to the similarity function to ensure that the deformations are smooth and non-intersecting. These computed deformations are then used to morph the initial segmented endocardium boundary and the process is repeated sequentially on all the images spanning the cardiac cycle. Based on the wall motion determined by image registration over the cardiac cycle, the triangulated mesh was then deformed accordingly during the CFD simulation as described below.

We model blood flow on moving domains as an incompressible and Newtonian fluid governed by the Navier-Stokes equations written in arbitrary Lagrangian-Eulerian (ALE) formulation as,

$$\rho\left(\frac{\partial \bar{v}}{\partial t} + (\bar{v} - \hat{v}).\nabla\bar{v}\right) = -\nabla p + 2\mu\nabla^2\bar{v}$$

$$\nabla.\bar{v} = 0,$$

where, $\bar{v}$ and $p$ are the fluid velocity and pressure, respectively, $\hat{v}$ is the endocardial wall velocity, and $\rho$ and $\mu$ are the fluid density and viscosity, respectively. We solve the above equations using an in-house parallelized finite element solver that employs stabilized linear finite elements for spatial discretization [25], the stable and second-order accurate generalized-$\alpha$ method for time integration, and a modified Newton-Raphson method for linearization of the governing equations [25]. The solver has been thoroughly validated [4, 53] and was previously employed to simulate cardiac hemodynamics in zebrafish embryos [4] and in studies of congenital heart disease in humans [22, 54, 55]. The computed velocity field is then post-processed to extract wall shear stress (WSS) and oscillatory shear index (OSI) defined as,

$$WSS := \bar{\tau}_w = \bar{\tau}_n - (\bar{\tau}_n.\hat{n})\hat{n}$$

and

$$OSI = \frac{1}{2}\left(1 - \frac{\left|\int_t^{t+T_c} \bar{\tau}_w \, dt\right|}{\int_t^{t+T_c} |\bar{\tau}_w| dt}\right),$$

where, $\bar{\tau}_n = \mu \nabla^s \bar{v} \hat{n} \stackrel{\text{def}}{=} \mu(\nabla \bar{v} + (\nabla \bar{v})^T)\hat{n}$ is the stress vector. We also extract the volume averaged kinetic energy ($\overline{KE}$) and rate of energy dissipation ($\bar{\Phi}$) defined as,

$$\overline{KE} = \frac{1}{V_d} \int_\Omega \rho |\bar{v}|^2 d\Omega$$

and

$$\bar{\Phi} = \frac{1}{V_d} \int_\Omega \mu \nabla^s \bar{v} : \nabla^s \bar{v} d\Omega,$$

where, $V_d$ is the ventricular volume and $T_c$ is the duration of the cardiac cycle. While OSI quantifies the change in the direction of the shear vector during the cardiac cycle normalized between 0 and 0.5, the energy dissipation ($\bar{\Phi}$) quantifies the rate at which the kinetic energy is being dissipated to heat due to viscosity [22].

**AG1478 and DAPT Treatment**

*ErbB* signaling inhibitor, AG1478, at 5 μM (Sigma–Aldrich, St. Louis, MO) in 1% DMSO was diluted in E3 medium at 30 hpf. DAPT (Sigma–Aldrich, St. Louis, MO), Y-Secretase Inhibitor, at 100 μM was also administered at 30 hpf.

**NICD mRNA and MO injection**

Gata1a MO were re-suspended in nuclease-free water and injected at 8 ng/nL at 1-4 cell stages. NICD mRNA at 10 ng was injected at 1-4 cell stages to rescue Notch signaling and to restore the trabeculation.

**Preparation of *NICD* mRNA**

Rat *NICD* cDNA was amplified from donor plasmids and cloned into the plasmid pCS2+ at the BamH I/EcoR I site. Clones with the insert of interest were selected by PCR screening and validated with sequencing. mRNA was prepared using the mMessage SP6 kit (Invitrogen, CA) following the manufacturer's instructions. The *in vitro* transcribed mRNA was purified using a total RNA isolation kit (Bio-Rad, CA) for *in vivo* rescue experiments.

**Confocal Imaging**

The transgenic *Tg(cmlc2:mCherry)* and *Tg(cmlc2:Venus-hGeminin)*$^{pd58}$ zebrafish lines were crossbred to visualize proliferating cardiomyocytes during cardiac morphogenesis. Embryonic zebrafish were randomly picked and immobilized in neutralized 0.02% tricaine solution (Sigma-Aldrich, St. Louis, MO). After movements of the pectoral fin stopped, embryos were anesthetized and mounted in 1-2% low-melting agarose (Sigma-Aldrich, St. Louis, MO) on a glass coverslip to perform imaging with dual channel confocal microscopy (Leica TCS-SP8-SMD). Images of newly proliferating cardiomyocytes and the variations of the cardiac morphology were taken with 3 μm interval in the Z-direction.

**Statistics**

For statistical comparisons between two experimental conditions, unpaired t-test was used. $P$ values $< 0.05$ were considered significant. Comparisons of multiple mean values were performed by one-way analysis of variance (ANOVA), and statistical significance among multiple groups was determined using Tukey's method.

### Study approval

Zebrafish were maintained in accordance with University of California Los Angeles (UCLA), Los Angeles, California Institutional Animal Care and Use Committee (IACUC) protocols under a project license also approved by the UCLA IACUC (ARC no. 2015-055).

## Results

### ErbB2 signaling mediates trabeculation

A transgenic zebrafish line, *Tg(cmlc2:gfp),* with the reporter transgene expressing green fluorescent protein (GFP) in cardiomyocytes, was used to demonstrate initiation of trabeculation. After cardiac looping from a peristaltic heart tube [23], endocardial trabeculation was initially absent (**Figure. 1A**). At 3 days post-fertilization (dpf), trabecular ridges (white arrows) developed across the atrioventricular (AV) canal, where atrial contraction generated pulsatile flow impacting on the site of initial trabeculation (**Figure. 1B: white arrow**) [4]. At 4 dpf, these ridges were prominent throughout the endocardium (**Figure. 1C**) [24]. At 5 dpf, they organized into an interconnected network (**Figure. 1D**) [5]. As a corollary, inhibiting *ErbB2,* downstream of Notch, with AG1478 inhibited the initiation of trabecular ridges from 2 dpf to 5 dpf (**Figure. 1E-H**). These findings indicate that myocardial *ErbB2* inhibition abrogates trabeculation.

### Genetic manipulations alter the interplay between 4-D (3-D + time) wall shear stress and Notch-mediated trabeculation

LSFM image data acquired from the transgenic *Tg(cmlc2:gfp)* embryos was used to perform 4-D CFD simulations to quantify wall shear stress (WSS). We reconstructed

spatial and temporal variations in WSS by solving the Navier-Stokes equations governing the incompressible blood flow with an imposed moving-wall boundary condition (ventricular wall motion) implemented in an arbitrary Lagrangian Eulerian (ALE) framework [7] with linear tetrahedral elements. We applied our in-house, stabilized, second-order, finite element method-based flow solver to simulate blood flow using large-scale, multi-core, high-performance computing clusters [25]. We first determined the 4-D WSS over the entire ventricular cavity, which we segmented from light-sheet scanning of the zebrafish ventricle (**Figure. 2, Video S1-S3**). 4-D CFD simulations revealed that *gata1a* MO injection, which lowered blood viscosity, resulted in reduction of area-averaged wall shear stress (AWSS) and subsequent trabeculation (n=3 vs. wild type; **Figure. 2A**) [7, 21, 26]. Using the same approach, we re-simulated for *gata1a* MO injected zebrafish using the viscosity of the wild type (WT) zebrafish blood and compared results [27]. The simulation revealed normalization to WT AWSS (**Figure. 2B**). These simulation results support the notion that viscosity (hemodynamics) is an important contributor to initiate trabeculation [7]. Furthermore, *wea* mutation, which inhibits atrial contraction, reduced blood flow across the AV valve, resulting in a significant reduction in AWSS and, subsequently, a non-trabeculated ventricle [7]. However, *ErbB2* inhibitor treatment only slightly reduced AWSS as compared to *gata1a* MO and *wea* mutants (**Figure. 2B**). Nonetheless, there was still a lack of trabeculae due to inhibition of *ErbB2,* downstream of Notch, despite of conserved hemodynamic forces [5, 16] (**Figure 2A-B**). Co-injection of *gata1a* MO with *NICD* mRNA rescue restored ventricular trabeculation; however, AWSS remained substantially lower (**Figure. 2A-B**). Quantifying WSS over one cardiac cycle, we observed that time-averaged WSS (TWSS) in *gata1a* MO, *gata1a* MO combined with *NICD* mRNA, and *wea* mutants, were also substantially lower compared to WT and *ErbB2* inhibitor (n=5 vs. WT

and *ErbB2* inhibitor) (**Figure. 2C**). Thus, CFD simulations using 4-D images of genetically modified embryos support that AWSS and TWSS were higher in trabeculated compared to non-trabeculated ventricles.

**Spatio-temporal variations in WSS develop in trabecular ridges and grooves**

Moving domain 4-D CFD simulations further demonstrated that trabecular ridges and grooves influenced the characteristics of shear stress during development (n=3) (**Figure. 3A, B**). Findings from previous 4-D WSS simulations (**Figure. 2A**) indicated that myocardial contraction promoted pulsatile shear stress (PSS) acting on the trabecular ridges, whereas flow recirculation in the trabecular grooves generated oscillatory shear stress (OSS) at 4 dpf in the WT (**Figure. 3C**). Time-dependent AWSS was 8.5-fold higher along the trabecular ridges than in the grooves during systole (**Figure. 3D**).

With respect to WSS-coordinated trabeculation, we demonstrated that OSS upregulated endothelial Notch signaling-related mRNA expression to a greater extent than PSS in human aortic endothelial cells (HAEC) (**Figure. 3E**). In addition, Notch1 mRNA expression was significantly elevated in response to OSS (0±3 $dyn \cdot cm^{-2}$ without a net forward flow) (**Figure. 3F**), whereas the levels of Notch1 mRNA expression were gradually reduced in response to the incremental forward flow components (0±3, 1±3, 2±3, 3±3, and 5±3 $dyn \cdot cm^{-2}$). Thus, spatial ($\partial\tau/\partial x$) and temporal variations ($\partial\tau/\partial t$) in WSS are implicated in modulating Notch activity in the trabecular ridges and grooves; OSS without net forward flow significantly induced Notch-related genes.

**WSS mediates sequential Notch activity from endocardium to trabecular grooves**

Using our rapid LSFM imaging with high-axial resolution, we captured sequential Notch activity (GFP) from endocardium to trabecular grooves in the transgenic *Tg*(*tp-1:gfp;cmlc:mCherry*) line. At 3 dpf, Notch activity was prominent in the endocardial layer and AV canal **(Figure. 4A-E and Figure. S1A-C).** At 4 dpf, TP-1, Notch promoter signal, for Notch activity appeared more prominent in the trabecular grooves than in the endocardium **(Figure. 4F-J and Figure. S1E-F)**. At 5 dpf, Notch activity in the grooves was interspersed with the trabecular ridges **(Figure. 4K-O and Figure. S1G-I).** As trabeculae organized to form a network, Notch activity was prominent in both the epicardium and trabecular grooves. Prominent Notch activity remained present in the AV canal for valve formation at 5 dpf [28]. In reference to the previous **Figure 3F**, OSS mediated up-regulation in Notch1-related mRNA expression is consistent with the prominent Tp-1 signal in the trabecular grooves (**Figure. 4I and 4N**). Thus, these findings suggest flow-mediated Notch activity progressed from endocardium at 3dpf to trabecular grooves at 4dpf.

In response to γ-secretase inhibitor, DAPT, to inhibit proteolytic release of Notch Intracellular Domain (NICD), endocardial TP-1 signal for Notch activity was absent at 3 dpf (**Figure. 5A-E**). Notch activity remained absent at 4 dpf **(Figure. 5F-J)**. Notch activity slightly appeared at 5 dpf while the ventricle remained non-trabeculated **(Figure. 5K-O)**. Notch activity at the AV canal also remained prominent at 5 dpf, reminiscent of the WT. These observations support endocardial Notch signaling initiation of trabeculation and subsequent Notch activity in the trabecular grooves.

In response to *NICD* mRNA injection to rescue Notch activation and trabeculation in the DAPT-treated transgenic *Tg*(*tp-1:gfp;cmlc:mcherry*) embryos, TP-1 signal for Notch activity was restored in the endocardium at 3 dpf (**Figure. 6A-E**). Similar to wild type,

Notch activity was also restored in the trabecular grooves at 4 dpf **(Figure. 6F-J)**. Notch activity became pronounced in the trabecular grooves and epicardium at 5 dpf (**Figure. 6K-O**). In addition, the TP-1 signal in the trabecular grooves (**Figure. 6I and 6N**) was reminiscent of the oscillatory flow-medicated Notch activation shown for WT in **Figure. 3A-C**. These findings further support spatiotemporal variations in shear stress underlying sequential upregulation of Notch activity to coordinate trabecular organization.

As a corollary, injection with *NICD* mRNA at 1-4 cell stage to the WT induced over-expression of Tp-1 signal in the endocardium at 3 dpf, with a notably larger ventricular wall thickness compared to WT (**Figure. S2A**). Notch activity became prominent in both the endocardium and epicardium with pronounced trabeculation at 4 dpf (**Figure. S2B**). Prominent Notch activity developed with an accentuated trabecular network at 5 dpf, as notable by the interconnecting bridges between the endo- and epi-cardium (**Figure. S2C, white arrows**). Therefore, *NICD* mNRA injection to the WT further corroborated the role of Notch activation in promoting trabecular network formation.

**FUCCI system localizes WSS-mediated cardiomyocyte proliferation in the trabecular ridges**

To localize WSS-mediated proliferating cardiomyocytes, we used the fluorescent ubiquitylation-based cell cycle indicator (FUCCI) system [29]. The two transgenic lines used in the FUCCI system employed two fusion proteins, *Tg(cmlc2:mCherry)* and *Tg(cmlc2:Venus-hGeminin)*$^{pd58}$, which were expressed in the myocardium and cyclically in the S/G2/M phase, respectively [29]. The Venus-hGeminin signal (arrowheads) indicated the proliferating cardiomyocytes (green$^{+}$ nuclei) (**Figure. 7**). At 4 and 5 dpf in WT, the number of proliferating cardiomyocytes was significantly higher

than the *gata1a* MO treated group (**Figure. 7A-D, G, and Video S4-S5**). Co-injecting *NICD* mRNA with *gata1a* MO partially restored the number of proliferating cardiomyocytes at 4 dpf and 5 dpf (**Figure. 7 E-G and Video S6**). Thus, the FUCCI system localized WSS-mediated cardiomyocyte proliferation in the trabecular ridges.

**Elevated oscillatory shear index (OSI) developed in the trabecular grooves**

We further quantified the extent of OSS in terms of direction of the shear vector over a period of time at any point on the ventricular wall called oscillatory shear index (OSI) which ranges from 0 to 0.5 [30]. An OSI of zero indicates a unidirectional net forward flow, whereas 0.5 reflects a 180º change in direction of the shear vector during the cardiac cycle. OSI equal to 0.5 with net forward flow.. In **Figure 3E-F**, OSS without a net forward flow (0±3 $dyn \cdot cm^{-2}$) significantly up-regulated endothelial Notch signaling-related genes. In the trabecular grooves in the X-Z plane (ventricular bottom view), CFD simulation showed high OSI values for each hemodynamic condition (n=3) (**Figure. 8)**. At 2 and 3 dpf, prominent trabecular ridges and grooves resulted in increased OSI. At 4 and 5 dpf, formation of the complete trabecular network further elevated OSI. In response to *ErbB2* inhibition, the non-trabeculated ventricle attenuated OSI except for the regions posterior to the inlet from the atrium (n=3) (**Figure. 8C, white asterisk**). In both the WT and *ErbB2* inhibition groups, high OSI developed in the low pressure region opposite the outflow tract and posterior to the AV canal to induce backflow [31]. As a corollary, the OSI profiles were also reduced in response to both *gata1a* MO and *wea* mutation (**Figure. 8J and 8L**). Rescue with *NICD* mRNA injection to the *gata1a* MO-treatment restored OSI in the trabecular grooves (**Figure. 8M**). Therefore, we recapitulated endocardial flow recirculation in terms of changes in OSI values, and high OSI co-localized in trabecular

groove where epicardial Notch was expressed during development. In accordance with our *in vitro* cell study (**Figure. 3E-F**), this supports our hypothesis that OSS activates epicardial Notch to develop trabecular grooves.

**Trabeculation contributed to kinetic energy dissipation**

4-D CFD simulations revealed that trabeculation introduces distinct area-averaged shear stress (AWSS) profiles (**Figure. 3D**). Next, we assessed the role of trabeculation in kinetic energy (KE) dissipation using our genetic models. In the aorta, it is well-recognized that KE of blood flow is converted into potential energy in the artery wall in the form of elastic recoil [32]. In the developing ventricle, our 4-D CFD simulations showed that pulsatile flow across the AV valve produces high KE impacting the endocardium (**Figure. 9A and Video S2)**, followed by increased KE dissipation (**Figure. 9B**). Both inhibition of atrial contraction in the *wea* mutants and reduction in viscosity in the *gata1a* MO group reduced the KE intensity **(Figure. 9A and 9C)** and subsequently reduced KE dissipation throughout the cardiac cycle (**Figure. 9B and 9D**). Notably, the *wea* mutation resulted in the most profound reduction in both KE and energy dissipation **(Figure. 9C-D)**. We previously demonstrated that the shear stress-mediated Notch-Nrg1-ErbB2 pathway contributes to the initiation of trabeculation and subsequent contractile function [7]. Here, our *in silico* analysis further revealed the key role of trabeculation for ventricular energy dissipation.

**Trabeculation influenced ventricular remodeling and cardiac strain**

By integrating light-sheet imaging with the synchronization algorithm for the cardiac cycles [7], followed by segmentation to extract the changes in 3-D ventricular morphology, we recapitulated the time-dependent changes in geometrical fluid domains in response

to *ErbB2* inhibition, *gata1a* MO, and *wea* mutation [7, 33-35]. Registration was performed on the 4-D image data using B-spline-based deformable registration methods [36], and the computed deformation field was used to morph the segmented ventricular surface to extract the period of ventricular contraction [22]. We quantified the dynamic changes in ventricular volume in response to 1) AG1478 treatment to inhibit *ErbB2* (n=3), 2) *gata1a* MO injection to reduce viscosity (n=3)[7, 21], and 3) the *wea* mutants to arrest atria contraction (n=3) (**Figure. 10A**) [5, 7]. We compared changes in mean end-diastolic volumes (WT = $5.5\times10^5$ $\mu m^3$; AG1478 = $8.0\times10^5$ $\mu m^3$; *gata1a* MO = $4.4\times10^5$ $\mu m^3$) and mean end-systolic volumes (WT = $2.3\times10^5$ $\mu m^3$; AG1478 = $2.9\times10^5$ $\mu m^3$, *gata1a* MO = $1.6\times10^5$ $\mu m^3$) (**Figure. 10B**) in relation to cardiac strain (**Figure. 10C**). In response to the *wea* mutation, both systolic ($0.8\times10^5\mu m^3$) and diastolic ventricular volume ($0.7\times10^5\mu m^3$) remained relatively unchanged as a result of the non-contractile ventricle. Analysis of ventricular axial strain also showed reduction in contractile function in the non-trabeculated ventricle (**Figure. 10C**). Altogether, changes in hemodynamic forces in the non-trabeculated ventricle were associated with increased end-systolic and end-diastolic volumes and reduced ventricular axial strain. These findings suggest a dual role for trabeculation to provide both enhanced contractile force and kinetic energy dissipation.

## Discussion

In this study, we demonstrate the quantification of hemodynamic forces inducing trabeculation via Notch signaling during cardiac development. Using a combination of light-sheet imaging and 4-D CFD, we recapitulated the initiation of trabeculation opposite to the AV valve where hemodynamic forces drive endocardial protrusion into the cardiac lumen via Notch-Nrg1-ErbB2 signaling [5, 7]. Our genetically altered zebrafish models

showed the role of 4-D WSS in trabeculation formation. While both PSS and OSS activated endothelial Notch signaling, OSS, even without net forward flow (0±3 dyn·cm$^{-2}$), induced the greatest upregulation of Notch-related genes. Using transgenic *Tg*(*tp-1:gfp;cmlc:mcherry*) embryos, our accompanying gain- and loss-of-function experiments showed sequential Notch activation from the endocardium to trabecular grooves in an alternating pattern (**Figure. 3C**). The use of a FUCCI system further localized WSS-mediated proliferating cardiomyocytes in the trabecular ridges. Our moving domain CFD simulations further demonstrated high OSI and increased KE dissipation in the trabeculated ventricles, and low OSI and reduced KE dissipation in the non-trabeculated ventricles and the ventricle underwent remodeling and reduced contractile function (16).

We assessed whether hemodynamic forces modulate trabecular ridges and grooves as well as cardiomyocyte proliferation. We used 3 genetic manipulations: (1) micro-injection of *gata1a*-MO at 1- to 4-cell stage to reduce hematopoiesis and subsequent viscosity by 90% [21, 26], (2) *wea* mutation to arrest atrial contraction, and (3) *ErbB2* inhibition. These manipulations reduced both AWSS and TWSS, and attenuated trabeculation at 5 dpf, leading to ventricular remodeling and reduced contraction. As demonstrated in 4-D CFD simulations, our *in silico* input of normal blood viscosity from WT zebrafish into ventricular wall boundaries from *gata1a* MO-injected zebrafish returned the WSS nearly to the level of WT, supporting the notion that WSS initiates trabeculation. When Notch signaling was inhibited with γ-secretase, DAPT, the ventricular wall remained non-trabeculated despite the presence of endocardial WSS, further supporting the role of endocardial Notch signaling in activating myocardial *ErbB2* and its initiation of trabeculation.

4-D CFD simulations also predicted spatiotemporal variations in WSS that may coordinate formation of trabecular ridges and grooves. While PSS induces endocardial

Notch to initiate trabecular ridge formation, OSS develops in the grooves to activate Notch (**Figure. 11A-B**). Of note, the Notch pathway is subject to many levels of regulation with both positive and negative feedback [37, 38]. The precise outcome of Notch activation is often sensitive to the combination of lateral inhibition and induction, and the tissue-specific ligand (Dll1 and Dll4, Jag1 and Jag2)-receptor interactions may influence the alternating pattern of trabecular ridges and grooves during cardiac development [39, 40]. For instance, Han *et al.* reported that Notch ligand Jag2b inhibits the neighboring ErbB2 signaling to prevent cardiomyocyte sprouting and trabeculation in the zebrafish embryos [6]. We previously showed that hemodynamic shear stress induces endocardial Notch-Nrg1-ErbB2 signaling to initiate trabeculation [7]. Our gain- and loss-of-function analyses further corroborated the sequential Notch activity from endocardium to trabecular grooves. These findings provide a biomechanical basis to further investigate whether PSS activates Delta-Notch "lateral induction" to initiate the ridge-like trabecular endocardium, whereas OSS induces Jag2b-Notch lateral inhibition on the neighboring ErbB2 signaling, resulting in the groove-like endocardium (**Figure. 11C**).

Our findings also support a role of trabeculation in dissipating KE of flow from atrial contraction during the early stages of cardiac development. Trabeculation is known to facilitate oxygenation and nutrient transport and to enhance cardiac contractile function [23]. Lack of dissipation in non-trabeculated hearts was associated with adverse ventricular remodeling and contractile dysfunction. The concept of KE dissipation is commonly applied to hydrodynamics of dam spillway protection, where steps are designed into dam spillways to prevent structural damage from fluid forces [41, 42]. Similar concepts are used to protect the lungs in mechanical respiratory systems [43]. During early cardiac morphogenesis, the thin ventricular wall may not withstand the KE transfer of atrial inflow,

and thus trabeculation may be desirable for ensuring enough dissipation to minimize momentum transfer to the ventricle walls. KE dissipation was reduced by almost half in non-trabeculated hearts, which are predisposed to heart failure and fetal demise [44]. The KE of atrial inflow is particularly important in zebrafish, where atrial contraction (A-wave) dominates over the early passive filling of the ventricle (E-wave) as evidenced by pulsed-wave Doppler velocity measurements (**Figure. S3**).[45] Ultimately, the series of events, including recirculatory flow in the grooves, may confer protection from ventricular remodeling and dysfunction (**Figure. 11C**) [6].

Non-trabeculated ventricles had reduced axial strain and ventricular remodeling (**Figure. 10**). Axial strain and ejection fraction were also reduced by *ErbB2* inhibition, whereas *Nrg1* mRNA rescue restored ventricular strain and EF [7]. Although *ErbB2* inhibition had little effect on KE, the non-trabeculated endocardium resulted in less KE dissipation, supporting the role of trabeculation in cushioning the forces of atrial inflow.

We previously used particle image velocimetry (PIV) to validate 4-D CFD code for spatiotemporally varying WSS and pressure gradients $\Delta P$ across the AV canal [4]. Inlet boundary velocities were acquired from the *Tg(gata1:dsred)* transgenic zebrafish in which the movement of red blood cells (RBC) was tracked (Mathworks, Natick, MA). While PIV is commonly used to validate CFD, it is entirely dependent on particle movement that may be inaccurate near the wall surface [46]. Furthermore, the small embryonic zebrafish poses an optical challenge. Mickoleit *et al*. and our laboratory has developed a rigorous method for reconstruction of zebrafish RBC movement in 3-D with a high spatiotemporal system [35]; however, modeling the circulating RBC remains unresolved. Further optimization of the 4-D light-sheet imaging methods may allow improved 4-D volume mapping techniques in future work [47].

In summary, by integrating advanced light-sheet imaging with *in silico* simulation and zebrafish genetics, we obtained insights into the role of hemodynamic forces in Notch-mediated trabeculation and demonstrated the importance of trabeculation in contractile function, kinetic energy dissipation, and cardiac morphogenesis, with relevance to human left ventricular non-compaction and hypotrabeculation.

**Acknowledgements**

The authors would like to express gratitude to Dr. David Traver from UCSD for providing *Tg(tp-1:gfp)*, and to Dr. Deborah Yelon from UCSD for providing the *wea* mutants. This study was supported by the National Institutes of Health HL118650 (T.K.H.), HL083015 (T.K.H.), HL111437 (T.K.H.), HL129727 (T.K.H., A.L.M.) AHA Scientist Development Grant 16SDG30910007 (R.R.S.P.), AHA Pre-Doctoral Fellowship 15PRE21400019 (J.L.), and AHA Institutional Research Enhancement Award 18AIREA33960193 (J.L.). Chapter I is a reprint of the article: Lee J*, Vedula V*, Baek KI*, Chen C, Hsu JJ, Ding YC, Chang CC, Kang H, Small A, Fei P, Choung CM, Li R, Demer L, Packard RS, Marsden AL, Hsiai TK. Spatial and temporal variations in hemodynamic forces initiate cardiac trabeculation. J Clin Invest insight. 3(13): e96672, 2018 (https://doi.org/10.1172/jci.insight.96672). Reprint was reproduced with permission from the publisher and all of the co-authors of the publication.

## FIGURES

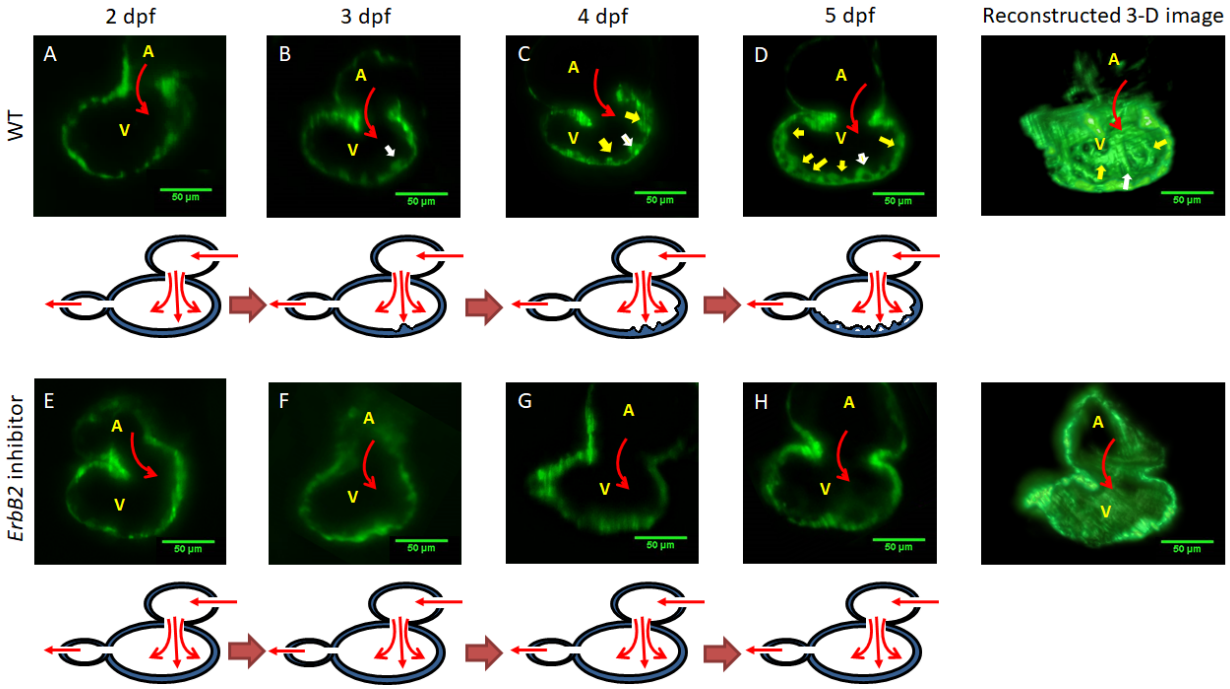


**Figure. 1.** *ErbB2*-dependent trabeculation during cardiac morphogenesis. **(A)** In the wild type (WT), trabecular ridges were absent at 2 dpf. **(B)** A prominent trabecular ridge developed across the atrioventricular (AV) canal at 3 dpf. Atrial blood flow (red arrow) through the AV canal directly impacted onto the endocardium. **(C)** Additional trabecular ridges (yellow arrows) developed on both sides of the initial trabecular ridge at 4 dpf. **(D)** Trabeculation organized to form an interwoven network at 5 dpf. (E-H) In response to *ErbB2* inhibitor (AG1478), trabeculation remained absent in the ventricular wall throughout the cardiac developmental stages. The ventricular wall thickness in response to *ErbB2* inhibitor was reduced as compared to the WT. A, atrium; V, ventricle. Reproduced in this dissertation with permission from Lee, Vedula, Baek *et al*.

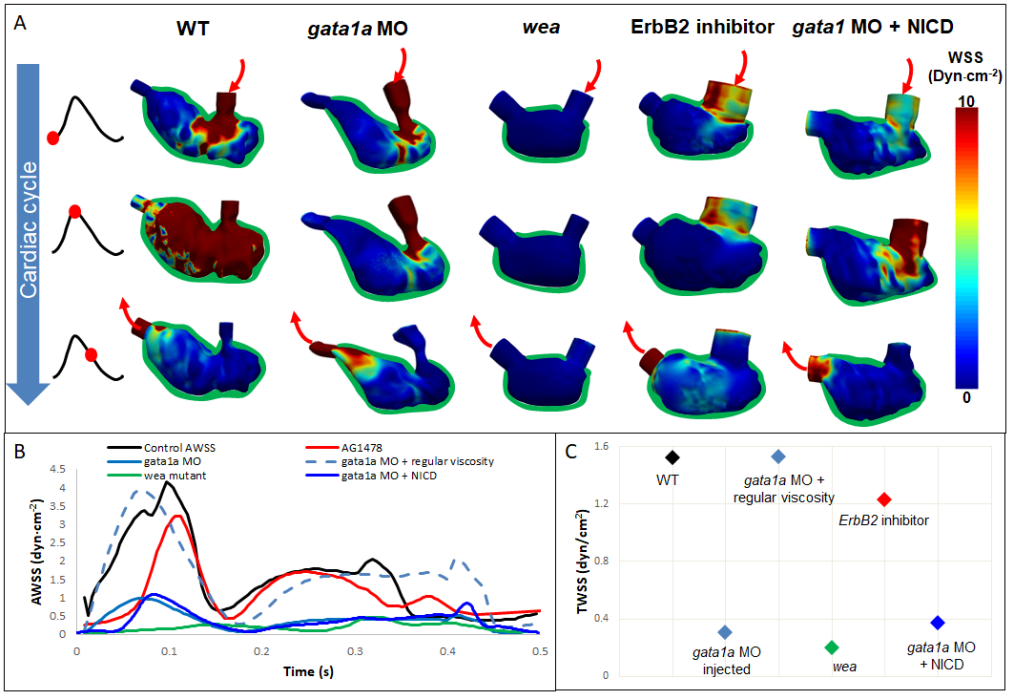


**Figure. 2.** Time-dependent 3-D computational fluid dynamics (CFD) simulation of the endocardial wall shear stress (WSS). **(A)** CFD simulation (3-D + time) was constructed from light-sheet imaging of zebrafish embryos in response to 4 genetic manipulations: *gata1a* morpholino (MO), *wea* mutants, *ErbB2* inhibitor, and co-injection of *gata1a* MO with *NICD* mRNA. The CFD simulation revealed spatial and temporal variations in ventricular WSS in synchrony with the changes in ventricular morphology during a cardiac cycle. **(B)** Over the entire ventricle of WT embryos, averaged WSS (AWSS) was higher than that in non-trabeculated ventricles from the 3 other groups. Despite the *ErbB2* inhibitor treatment, AWSS was still higher than those of *gata1a* MO-injected and *wea* mutant. When the ventricular cavity of *gata1a* MO-injected model was demarcated to simulate WSS with WT blood viscosity, AWSS value was restored to that of WT. **(C)** Time-averaged WSS (TWSS) in the WT embryos was higher than that of the *gata1a* MO-injected (lower blood viscosity) and *wea* mutants (lower cardiac contractility), whereas the *ErbB2*-inhibited embryos developed a similar TWSS as compared with the WT. *In silico* simulation to restore to the WT blood viscosity in the *gata1a*-MO injected embryos normalized the TWSS to that of the WT. Reproduced in this dissertation with permission from Lee, Vedula, Baek *et al*.

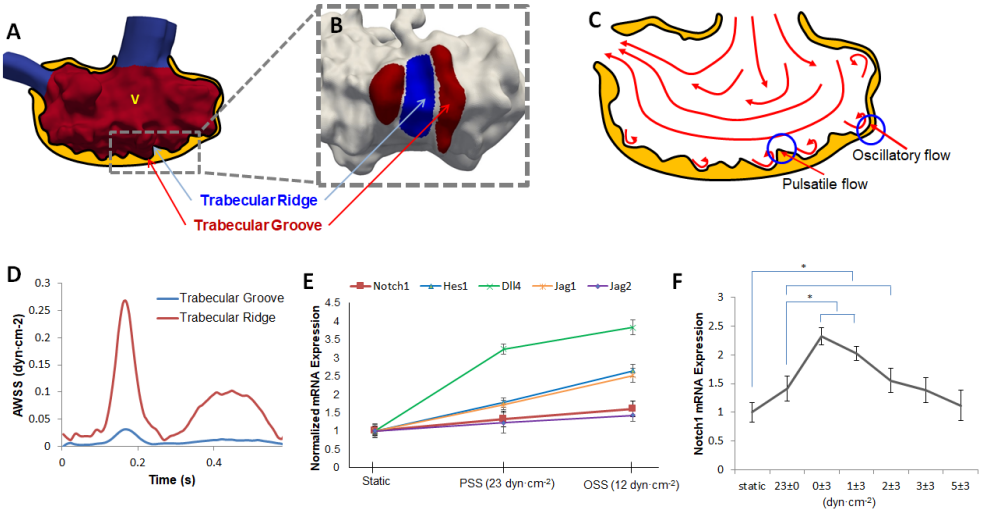


**Figure. 3.** Spatio-temporal variations in WSS in trabecular ridges and grooves modulate Notch-related gene expression. **(A)** Time-dependent 3-D CFD simulation revealed distinct spatial variations in ventricular WSS as highlighted in red color. **(B)** Distinct shear stress profiles developed in the trabecular ridges vs. grooves. **(C)** Trabecular ridges were exposed to pulsatile shear stress (PSS) while trabecular grooves were exposed to oscillatory shear stress (OSS). An elevated oscillatory shear index (OSI) developed as a result of flow trapped between the two trabecular ridges. **(D)** Trabecular ridges were exposed to significantly higher AWSS than trabecular grooves. This observation prompted the investigation into the initiation of trabecular ridges in response to high WSS. (E) Using a previously reported dynamic flow system [56], we demonstrated that OSS induced Notch-related mRNA expression to a greater extent than did PSS. **(F)** Notch1 receptor expression was highest under oscillatory shear stress (0±3 dyn·cm$^{-2}$ with zero net flow). Notch1 expression was attenuated in response to a gradual increase in net forward flow (1±3, 2±3, 3±3, and 5±3 dyn·cm$^{-2}$) (t-test *$P$ < 0.05, n=3). Reproduced in this dissertation with permission from Lee, Vedula, Baek *et al*.

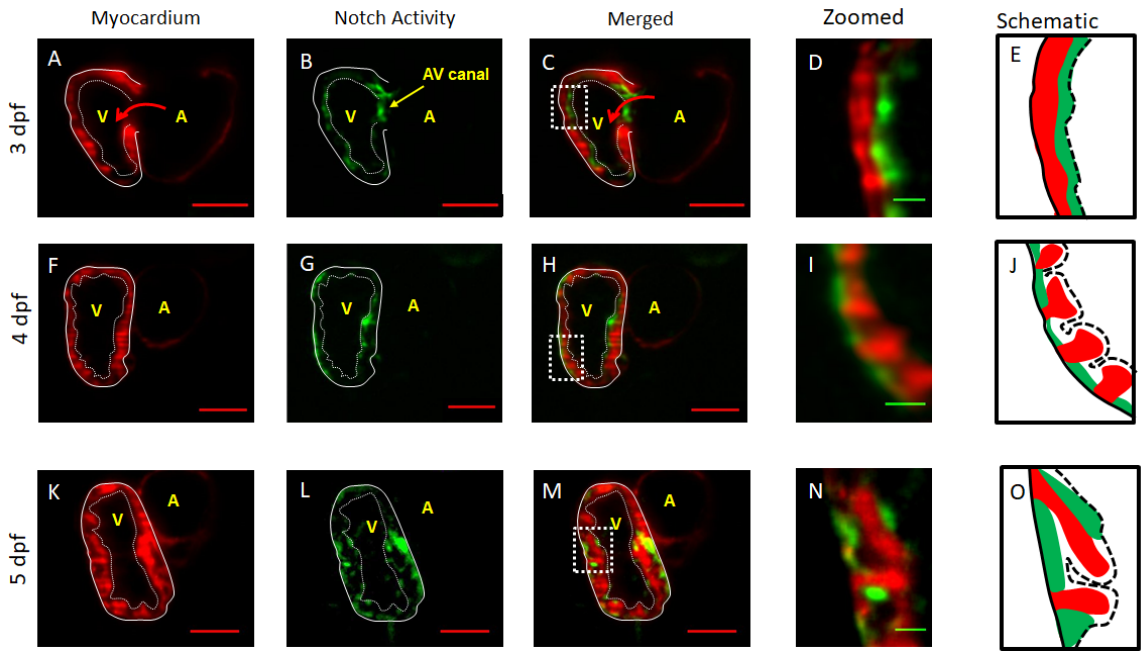


**Figure. 4.** Sequential Notch activity from endocardium to trabecular grooves in the WT. Our 4-D LSFM imaging captured sequential Notch1b activation (green) from endo- to epicardium in the transgenic *Tg(Tp-1:GFP;cmlc:mcherry)* line. **(A-E)** At 3 dpf, Notch1b activity localized to the endocardial layer and AV canal. **(F-J)** At 4 dpf, Notch activity located primarily in the epicardium than in the endocardium. Epicardial Notch1b activity and trabecular ridges organized into an alternating pattern. **(K-O)** At 5 dpf, trabeculae developed into a network structure, Notch activity was prominent in both the endocardium and trabecular grooves. Red scale bar: 50 μm. Green scale bar: 10 μm. Dotted line (E, J, O): endocardium. Solid line (E, J, O): epicardium. (n=3). Reproduced in this dissertation with permission from Lee, Vedula, Baek *et al*.

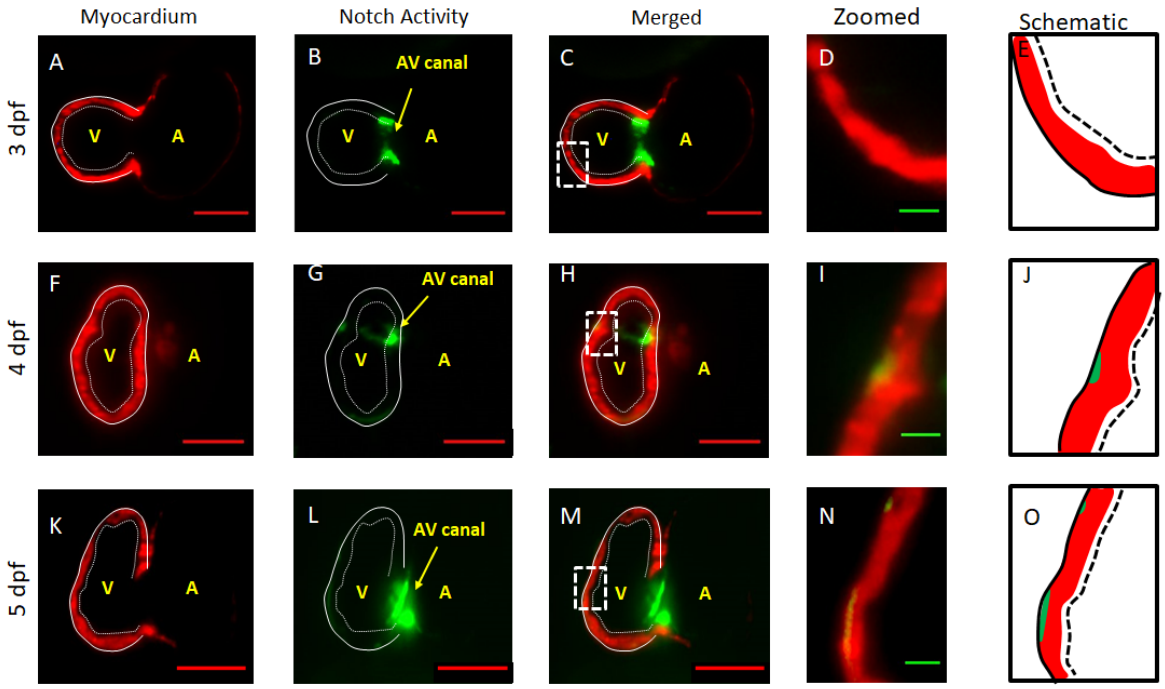


**Figure. 5.** Inhibition of Notch activity and trabeculation in response to γ-secretase inhibition. **(A-E)** At 3 dpf, DAPT treatment reduced Notch activity in the endocardium except for the AV canal region in the transgenic *Tg(Tp-1:GFP;cmlc:mcherry)* line. **(F-J)** At 4 dpf, Notch activity remained absent in the endocardium. A small area of Notch activity appeared in the epicardium (green arrow). **(K-O)** At 5 dpf, additional small areas of Notch activation appeared in the epicardium, while trabeculation remained absent. Red scale bar: 50 μm. Green scale bar: 10 μm. Dotted line (E, J, O): endocardium. Solid line (E, J, O): epicardium. (n=3). Reproduced in this dissertation with permission from Lee, Vedula, Baek *et al*.

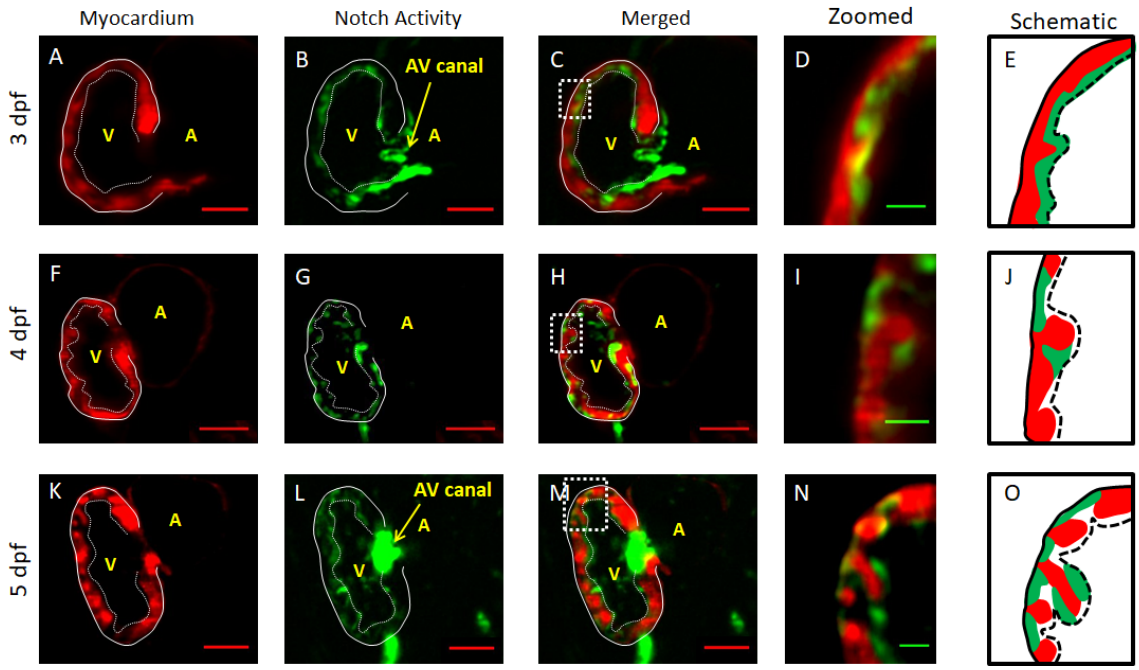


**Figure. 6**. NICD mRNA injection rescued Notch activation and trabeculation in the DAPT-treated embryos. **(A-E)** At 3 dpf, NICD injection rescued Notch activation in the endocardium of DAPT-treated transgenic Tg(Tp-1:GFP;cmlc:mcherry) embryos. **(F-J)** At 4 dpf, Notch activity appeared to be more prominent in the trabecular grooves than in the endocardium, reminiscent of the WT. **(K-O)** At 5 dpf, Notch activity was present in both endocardium and trabecular grooves, but not myocardium. Red scale bar: 50 μm. Green scale bar: 10 μm. Dotted line (E, J, O): endocardium. Solid line (E, J, O): epicardium. (n=5). Reproduced in this dissertation with permission from Lee, Vedula, Baek *et al*.

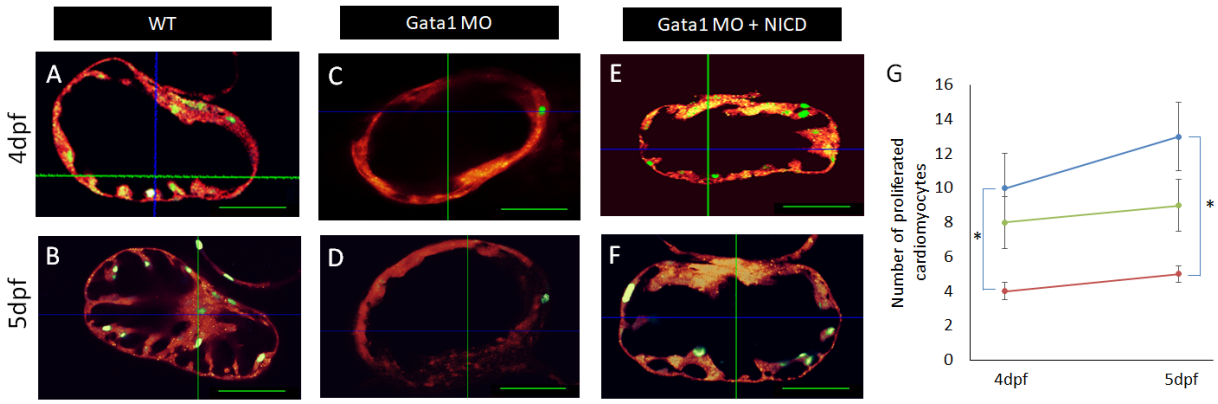


**Figure. 7.** FUCC system localized WSS-mediated proliferating cardiomyocytes in the trabecular ridges. **(A, B)** FUCCI system was used to visualize the myocardial proliferation via WT double transgenic zebrafish line between *Tg(cmlc2:mCherry)* and *Tg(cmlc2:Venus-hGeminin)*$^{pd58}$. Proliferating cardiomyocytes (green$^{+}$ nuclei) were present at the trabecular ridgese. **(C, D)** In response to *gata1a* MO, the number of proliferating cardiomyocytes was attenuated (n=4, t-test *$p < 0.05$). **(E, F)** Co-injection of *gata1a* MO with NICD mRNA partially restored cardiomyocyte proliferation (n=4, t-test *$p < 0.05$). (G) The graph statistically quantified the numbers of proliferating cardiomyocytes in response to *gata1a* Mo and to NICD mRNA rescue. Reproduced in this dissertation with permission from Lee, Vedula, Baek *et al*.

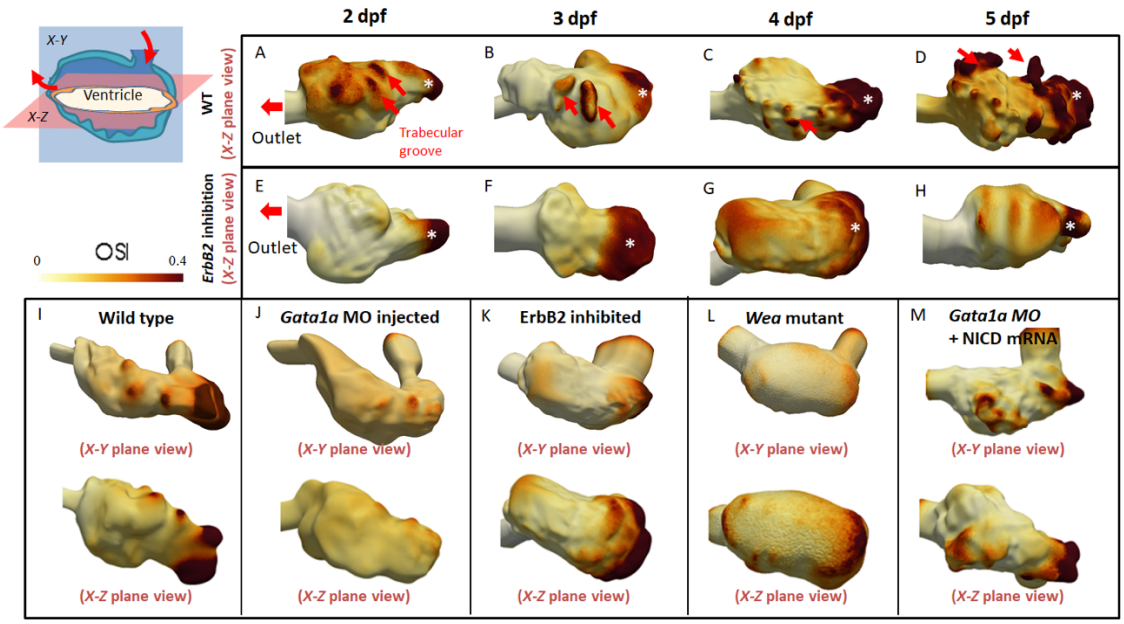


**Figure. 8.** Elevated OSI values developed in trabecular ridges and is depend ventricular surface roughness. OSI revealed distinct difference in the WT vs. ErbB2 inhibitor treatment and roughness of ventricular surface. **(A-B)** At 2 and 3 dpf, elevated OSI was interspersed between trabecular ridges and grooves in the WT. **(C-D)** At 4 and 5 dpf, high OSI associated with formation of the trabecular network. **(E-G)** However, ErbB2 inhibition to attenuate trabeculation abrogated the interspersed OSI at 2, 3, and 4 dpf. **(H)** Despite distinct OSI from the WT at 5 dpf, slight interspersion of OSI appeared in the ErbB2 inhibited group with consistent absence of trabecular network. **(I)** High OSI is generated in trabecular ridges at 4dpf. **(J)** OSI is significantly reduced after lowering of blood viscosity. **(K)** ErbB2 inhibited zebrafish showed attenuated trabecular wall which stymied oscillatory flow at ventricular wall. **(L)** Due to lack of atrial contraction, blood flow acting on the ventricle is low. This generated minimal amount of OSI. **(H)** Co-injection of NICD mRNA and gata1 MO, OSI is reminiscent of WF zebrafish due to restored trabeculation.

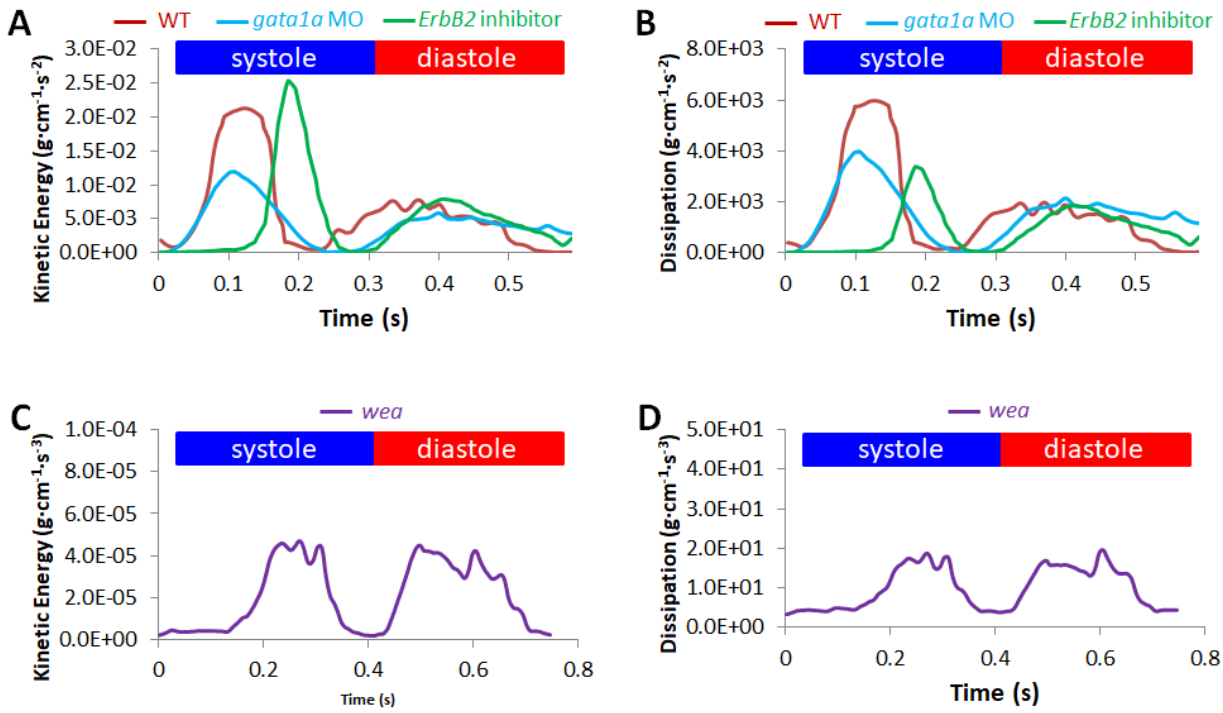


**Figure. 9.** Effects of trabeculation on the kinetic energy and energy dissipation in the ventricle at 4 dpf. **(A)** Gata1a MO injection reduced viscosity and WSS, resulting in a lower kinetic energy (KE) profile than in WT embryos during a cardiac cycle. However, ErbB2 inhibition model, which reduces trabeculation, received similar high KE. **(B)** Both *gata1a* MO injection and ErbB2 inhibition reduced energy dissipation in the ventricle, compared with WT. **(C)** *Wea* mutants, which lack the atrial contraction needed for initiation of trabeculation, had a profound reduction in KE. **(D)** *Wea* mutants also had a profound reduction in energy dissipation, associated with ventricular remodeling (Figure 2A).

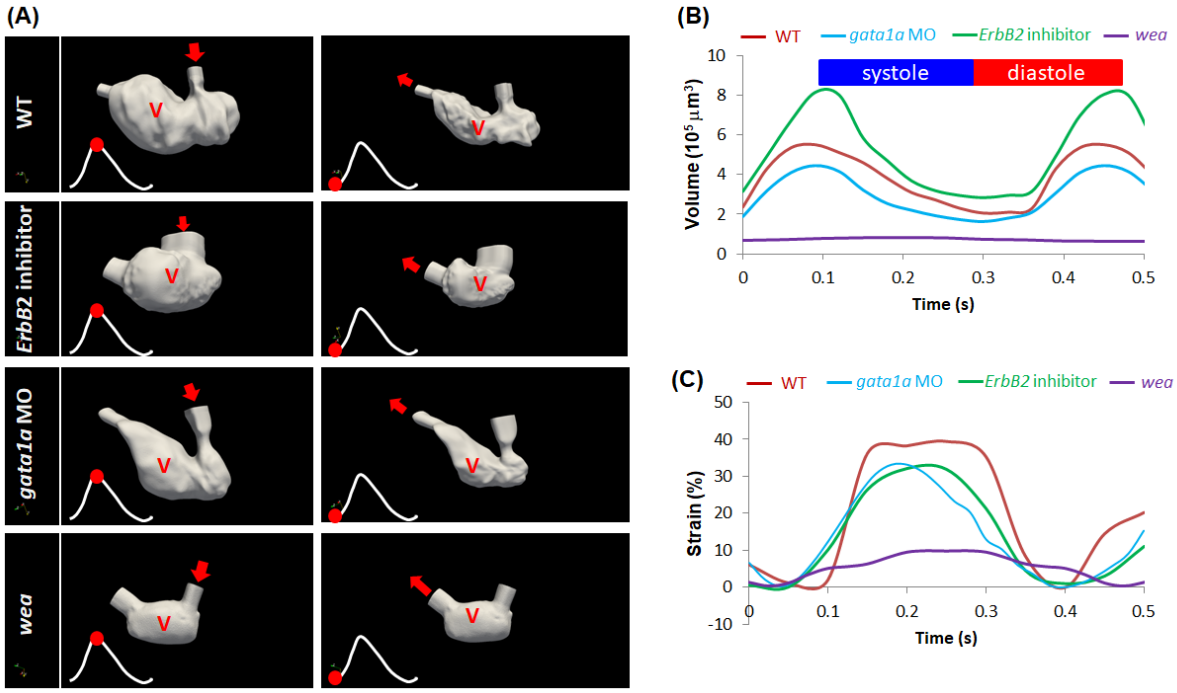


**Figure. 10.** Genetic manipulations of trabeculation influenced ventricular remodeling and strain rates. **(A)** Changes in 3-D fluid domain at end-diastole and -systole were recaptured by light-sheet imaging and were subsequently reconstructed. The 3-D ventricular contours reflect the trabeculated endocardium in the WT and the non-trabeculated endocardium in the genetic models. The red dots indicate the instantaneous moment at which ventricular volume was reconstructed during the cardiac cycle. **(B)** Time-dependent changes in ventricular volume were compared in response to genetic manipulations. ErbB2 inhibitor-mediated attenuation in trabeculation resulted in an increase in ventricular volume as compared to the WT. *Gata1a* MO-mediated reduction in shear stress reduced ventricular volume. *Wea* mutation resulted in a nearly zero ventricular volume. **(C)** Genetic manipulations to inhibit trabeculation also resulted in a reduction in ventricular strain rates ($p < 0.01$, n=3).

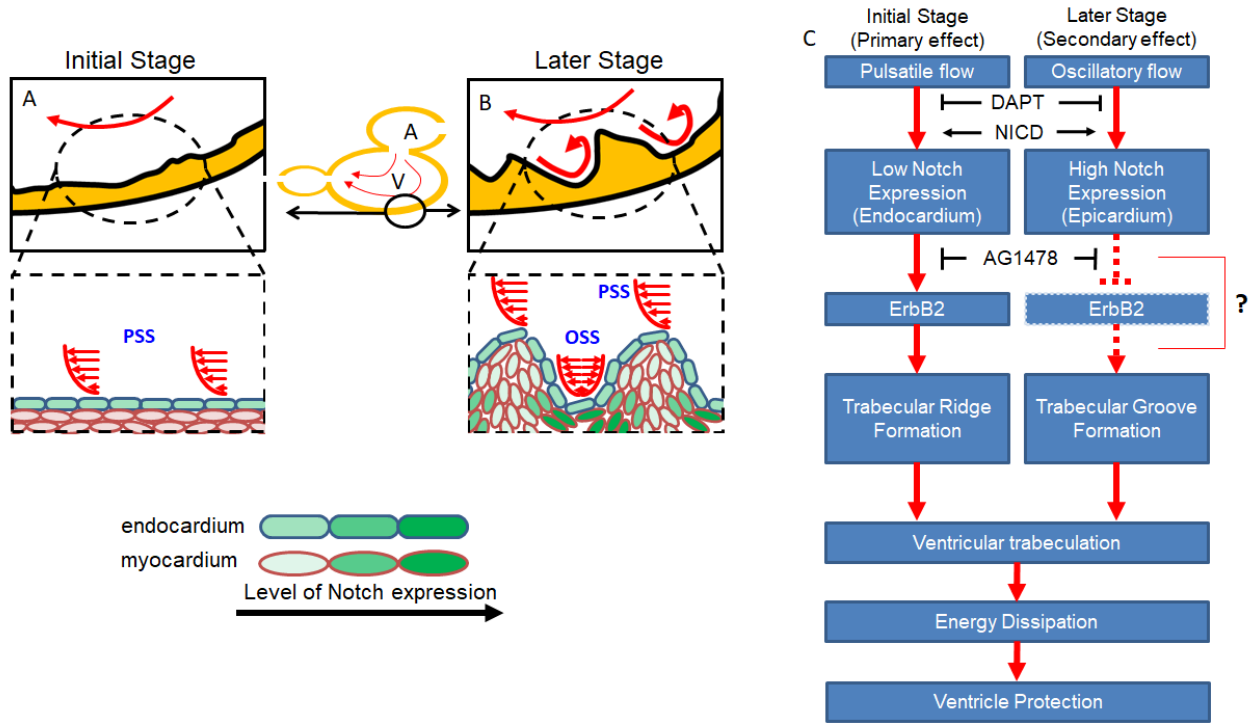


**Figure. 11.** Schematic of spatial and temporal determinants of shear stress and endocardial trabeculation. **(A)** WSS activates endocardial Notch signaling. **(B)** The development of trabecular ridges promotes flow recirculation yielding OSS, which, in turn, induces Notch activity in the trabecular grooves. **(C)** Coordination of PSS-induced endocardial Notch and OSS-mediated Notch in the grooves may organize ventricular trabeculation. While endocardial Notch activates myocardial Erbb2 expression to initiate trabecular ridge formation, Notch activity in the grooves may cause lateral inhibition of Erbb2 expression and resultant trabeculation [6]. DAPT treatment inhibits NICD release, whereas NICD expression rescues Notch signaling and trabeculation. Trabeculae may serve to dissipate kinetic energy thus preventing ventricular remodeling and dysfunction.

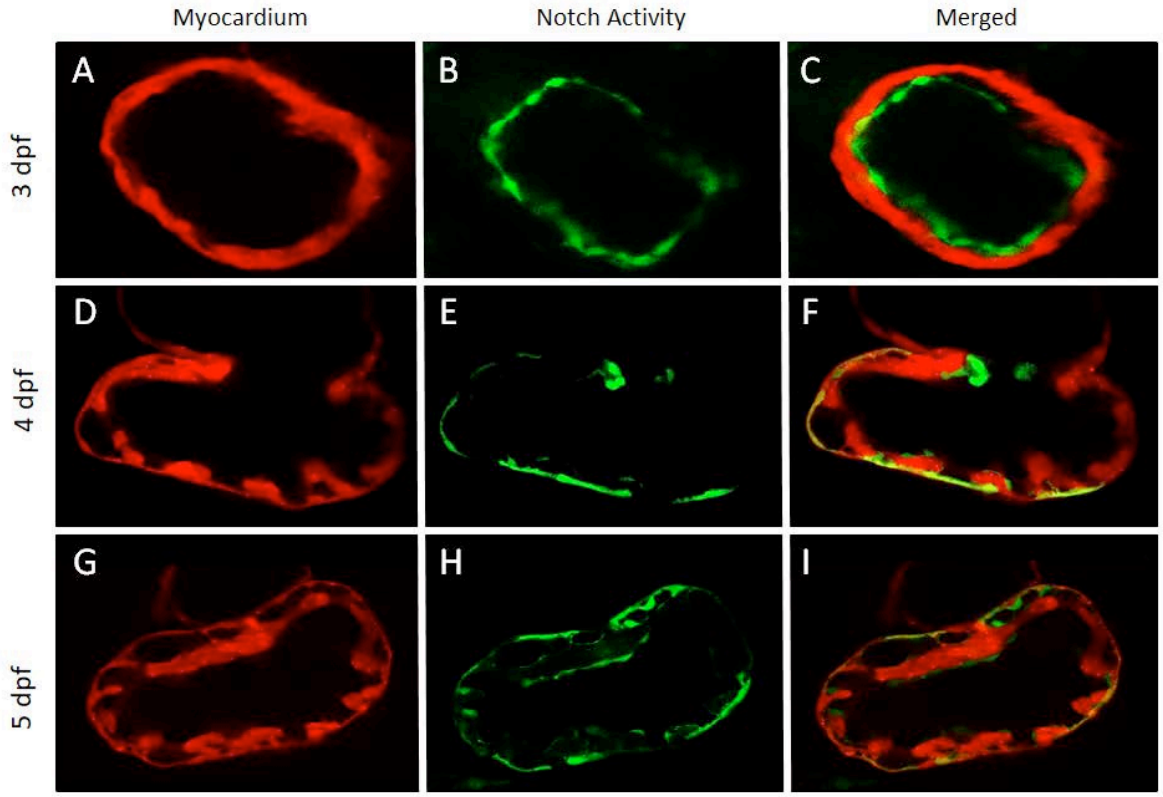


**Figure S1.** Sequential Notch in WT zebrafish from confocal microscopy. **(A-C)** At 3 dpf, Tp1 signal, Notch promoter, activity initially resided in the endocardial layer and AV canal. **(D-F)** At 4 dpf, Notch activity appeared to be more prominent in the epicardium than in the endocardium. Epicardial Tp1 signal and trabecular ridges were organizing into an interspersed pattern. **(G-H)** As trabeculae developed to form a network structure, Notch activity was prominent in both the epi- and endocardium. Notch activity was absent in the myocardium.

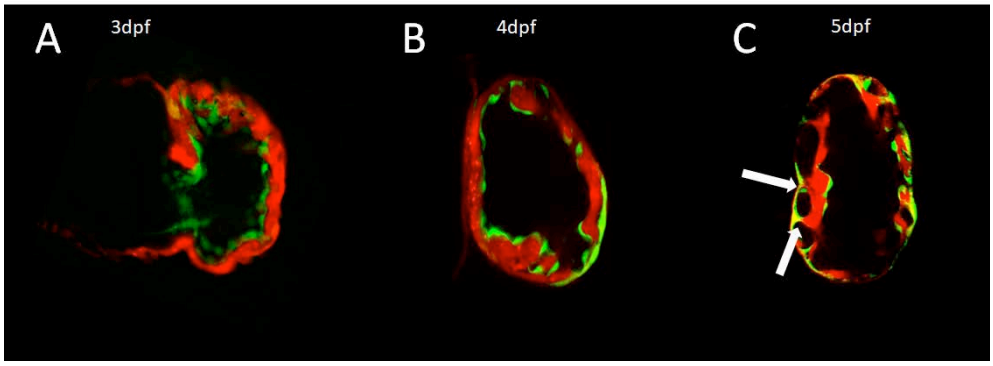


**Figure S2.** NICD mRNA injection to WT zebrafish *Tg(cmlc:mchery; tp1:gfp).* **(A)** At 3dpf, tp1 signal was initially expressed in endocardium as other groups. However, ventricular thickness was thicker than WT. **(B)** At 4 dpf, ventricle was over trabeculated and Notch activity was shown in both endocardium and myocardium. **(C)** Large amount of myocardium was separated from ventricular wall and form a trabecular network by interconnecting with thin bridges (arrow).

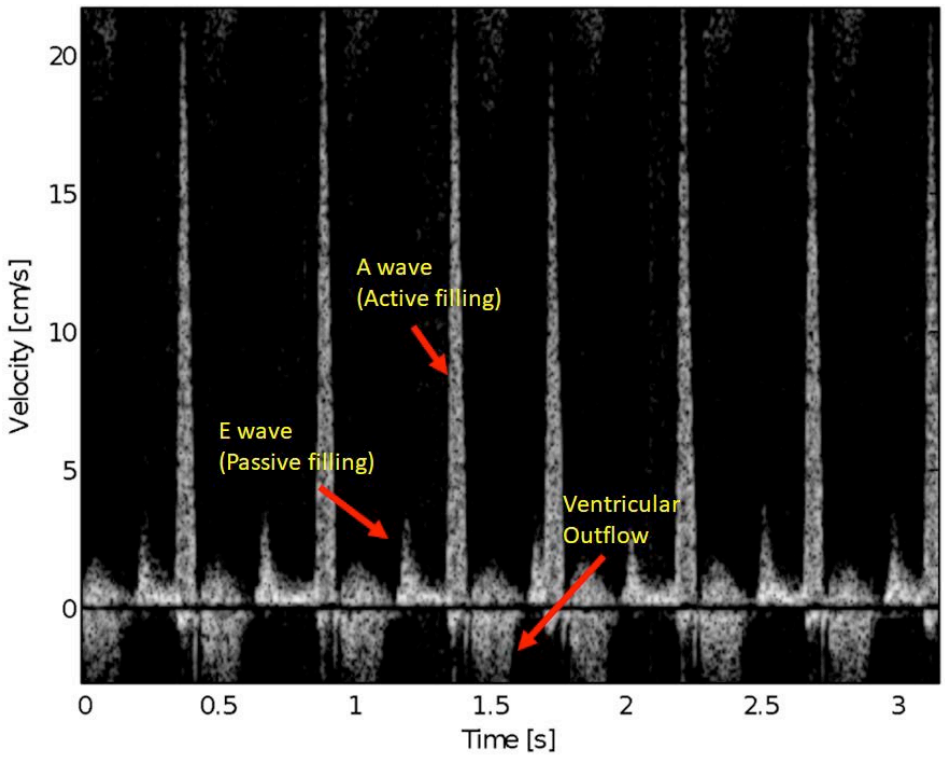


**Figure S3.** Pulse-wave (PW) Doppler image of adult wild type zebrafish. PW Doppler provides assessment of passive filling of the ventricle (early [E]-wave velocity) and active filling during atrial systole (atrial [A]-wave velocity). Unlike in human hearts, atrial contraction (A-wave) is stronger than passive filling by ventricular relaxation, therefore, E/A ratio is < 1 at baseline. For *wea* mutant, A-wave would be negligible due to lack to atrial contraction.

**[Supplemental Videos Available Online]**

**Video S1**. Registration of 4-D beating heart with segmented fluid domain.

**Video S2** 4-D WSS profile of WT zebrafish.

**Video S3**. 4-D streamline traces of WT zebrafish heart.

**Video S4**. Cardiomyocytes proliferation of WT zebrafish at 5 dpf

**Video S5**. Cardiomyocytes proliferation of WT zebrafish at 5 dpf

**Video S6**. Cardiomyocytes proliferation of rescue zebrafish with NICD mRNA injection at 5 dpf

## References


1. Hove JR, Koster RW, Forouhar AS, Acevedo-Bolton G, Fraser SE, Gharib M. Intracardiac fluid forces are an essential epigenetic factor for embryonic cardiogenesis. *Nature*. 2003;421:172-177

2. Wang X, Ha T. Defining single molecular forces required to activate integrin and notch signaling. *Science*. 2013;340:991-994

3. Gordon WR, Zimmerman B, He L, Miles LJ, Huang J, Tiyanont K, McArthur DG, Aster JC, Perrimon N, Loparo JJ, Blacklow SC. Mechanical allostery: Evidence for a force requirement in the proteolytic activation of notch. *Developmental cell*. 2015;33:729-736

4. Lee J, Moghadam ME, Kung E, Cao H, Beebe T, Miller Y, Roman BL, Lien CL, Chi NC, Marsden AL, Hsiai TK. Moving domain computational fluid dynamics to interface with an embryonic model of cardiac morphogenesis. *PloS one*. 2013;8:e72924

5. Peshkovsky C, Totong R, Yelon D. Dependence of cardiac trabeculation on neuregulin signaling and blood flow in zebrafish. *Developmental dynamics : an official publication of the American Association of Anatomists*. 2011;240:446-456

6. Han P, Bloomekatz J, Ren J, Zhang R, Grinstein JD, Zhao L, Burns CG, Burns CE, Anderson RM, Chi NC. Coordinating cardiomyocyte interactions to direct ventricular chamber morphogenesis. *Nature*. 2016;534:700-704

7. Lee J, Fei P, Packard RR, Kang H, Xu H, Baek KI, Jen N, Chen J, Yen H, Kuo CC, Chi NC, Ho CM, Li R, Hsiai TK. 4-dimensional light-sheet microscopy to elucidate shear stress modulation of cardiac trabeculation. *The Journal of clinical investigation*. 2016;126:1679-1690

8. Rasouli SJ, Stainier DYR. Regulation of cardiomyocyte behavior in zebrafish trabeculation by neuregulin 2a signaling. *Nature communications*. 2017;8:15281

9. Zhang W, Chen H, Qu X, Chang CP, Shou W. Molecular mechanism of ventricular trabeculation/compaction and the pathogenesis of the left ventricular noncompaction cardiomyopathy (lvnc). *American journal of medical genetics. Part C, Seminars in medical genetics*. 2013;163C:144-156

10. Finsterer J, Stollberger C, Towbin JA. Left ventricular noncompaction cardiomyopathy: Cardiac, neuromuscular, and genetic factors. *Nature reviews. Cardiology*. 2017;14:224-237

11. Pignatelli RH, McMahon CJ, Dreyer WJ, Denfield SW, Price J, Belmont JW, Craigen WJ, Wu J, El Said H, Bezold LI, Clunie S, Fernbach S, Bowles NE, Towbin JA. Clinical characterization of left ventricular noncompaction in children: A relatively common form of cardiomyopathy. *Circulation*. 2003;108:2672-2678

12. Brescia ST, Rossano JW, Pignatelli R, Jefferies JL, Price JF, Decker JA, Denfield SW, Dreyer WJ, Smith O, Towbin JA, Kim JJ. Mortality and sudden death in pediatric left ventricular noncompaction in a tertiary referral center. *Circulation*. 2013;127:2202-2208

13. Nugent AW, Daubeney PE, Chondros P, Carlin JB, Cheung M, Wilkinson LC, Davis AM, Kahler SG, Chow CW, Wilkinson JL, Weintraub RG, National Australian Childhood Cardiomyopathy S. The epidemiology of childhood cardiomyopathy in australia. *The New England journal of medicine*. 2003;348:1639-1646

14. Hoedemaekers YM, Caliskan K, Michels M, Frohn-Mulder I, van der Smagt JJ, Phefferkorn JE, Wessels MW, ten Cate FJ, Sijbrands EJ, Dooijes D, Majoor-Krakauer DF. The importance of genetic counseling, DNA diagnostics, and cardiologic family screening in left ventricular noncompaction cardiomyopathy. *Circulation. Cardiovascular genetics*. 2010;3:232-239

15. Samsa LA, Givens C, Tzima E, Stainier DY, Qian L, Liu J. Cardiac contraction activates endocardial notch signaling to modulate chamber maturation in zebrafish. *Development*. 2015;142:4080-4091

16. Liu J, Bressan M, Hassel D, Huisken J, Staudt D, Kikuchi K, Poss KD, Mikawa T, Stainier DY. A dual role for erbb2 signaling in cardiac trabeculation. *Development*. 2010;137:3867-3875

17. Grego-Bessa J, Luna-Zurita L, del Monte G, Bolos V, Melgar P, Arandilla A, Garratt AN, Zang H, Mukouyama YS, Chen H, Shou W, Ballestar E, Esteller M, Rojas A, Perez-Pomares JM, de la Pompa JL. Notch signaling is essential for ventricular chamber development. *Developmental cell*. 2007;12:415-429

18. Chen H, Shi S, Acosta L, Li W, Lu J, Bao S, Chen Z, Yang Z, Schneider MD, Chien KR, Conway SJ, Yoder MC, Haneline LS, Franco D, Shou W. Bmp10 is essential for maintaining cardiac growth during murine cardiogenesis. *Development*. 2004;131:2219-2231

19. High FA, Epstein JA. The multifaceted role of notch in cardiac development and disease. *Nature reviews. Genetics*. 2008;9:49-61

20. Masumura T, Yamamoto K, Shimizu N, Obi S, Ando J. Shear stress increases expression of the arterial endothelial marker ephrinb2 in murine es cells via the vegf-notch signaling pathways. *Arteriosclerosis, thrombosis, and vascular biology*. 2009;29:2125-2131

21. Vermot J, Forouhar AS, Liebling M, Wu D, Plummer D, Gharib M, Fraser SE. Reversing blood flows act through klf2a to ensure normal valvulogenesis in the developing heart. *PLoS biology*. 2009;7:e1000246

22. Vedula V, Lee J, Xu H, Kuo CJ, Hsiai TK, Marsden AL. A method to quantify mechanobiologic forces during zebrafish cardiac development using 4-d light sheet imaging and computational modeling. *PLoS computational biology*. 2017;13:e1005828

23. Hu N, Sedmera D, Yost HJ, Clark EB. Structure and function of the developing zebrafish heart. *The Anatomical record*. 2000;260:148-157

24. Liu E, Pan X, Liu R, Tan Y, Jin Z, Wei G, Liu Y, Hu N. [hyperconjugation, characteristic infrared absorption of methylsulfones and crystal structures of selected aromaticsulfones]. *Guang pu xue yu guang pu fen xi = Guang pu*. 2000;20:31-39

25. Esmaily-Moghadam M, Bazilevs Y, Marsden AL. A bi-partitioned iterative algorithm for solving linear systems arising from incompressible flow problems. *Computer Methods in Applied Mechanics and Engineering*. 2015;286:40-62

26. Galloway JL, Wingert RA, Thisse C, Thisse B, Zon LI. Loss of gata1 but not gata2 converts erythropoiesis to myelopoiesis in zebrafish embryos. *Developmental cell*. 2005;8:109-116

27. Lee J, Chou TC, Kang D, Kang H, Chen J, Baek KI, Wang W, Ding Y, Carlo DD, Tai YC, Hsiai TK. A rapid capillary-pressure driven micro-channel to demonstrate newtonian fluid behavior of zebrafish blood at high shear rates. *Scientific reports*. 2017;7:1980

28. D'Amato G, Luxan G, del Monte-Nieto G, Martinez-Poveda B, Torroja C, Walter W, Bochter MS, Benedito R, Cole S, Martinez F, Hadjantonakis AK, Uemura A, Jimenez-Borreguero LJ, de la Pompa JL. Sequential notch activation regulates ventricular chamber development. *Nature cell biology*. 2016;18:7-20

29. Choi WY, Gemberling M, Wang J, Holdway JE, Shen MC, Karlstrom RO, Poss KD. In vivo monitoring of cardiomyocyte proliferation to identify chemical modifiers of heart regeneration. *Development*. 2013;140:660-666

30. Gabriel S, Ding Y, Feng Y. Extending the oscillatory index to discern oscillatory flow modes. 2016

31. Kambe T. *Elementary fluid mechanics*. World Scientific; 2007.

32. Hall JE. *Guyton and hall textbook of medical physiology e-book*. Elsevier Health Sciences; 2015.

33. Liebling M, Forouhar AS, Gharib M, Fraser SE, Dickinson ME. Four-dimensional cardiac imaging in living embryos via postacquisition synchronization of nongated slice sequences. *Journal of biomedical optics*. 2005;10:054001

34. Fei P, Lee J, Packard RR, Sereti KI, Xu H, Ma J, Ding Y, Kang H, Chen H, Sung K, Kulkarni R, Ardehali R, Kuo CC, Xu X, Ho CM, Hsiai TK. Cardiac light-sheet fluorescent microscopy for multi-scale and rapid imaging of architecture and function. *Scientific reports*. 2016;6:22489

35. Mickoleit M, Schmid B, Weber M, Fahrbach FO, Hombach S, Reischauer S, Huisken J. High-resolution reconstruction of the beating zebrafish heart. *Nature methods*. 2014;11:919-922

36. Myronenko A, Song X. Intensity-based image registration by minimizing residual complexity. *IEEE Transactions on Medical Imaging*. 2010;29:1882-1891

37. Bray SJ. Notch signalling: A simple pathway becomes complex. *Nature reviews. Molecular cell biology*. 2006;7:678-689

38. Kadesch T. Notch signaling: The demise of elegant simplicity. *Current opinion in genetics & development*. 2004;14:506-512

39. Petrovic J, Formosa-Jordan P, Luna-Escalante JC, Abello G, Ibanes M, Neves J, Giraldez F. Ligand-dependent notch signaling strength orchestrates lateral induction and lateral inhibition in the developing inner ear. *Development*. 2014;141:2313-2324

40. Boareto M, Jolly MK, Lu M, Onuchic JN, Clementi C, Ben-Jacob E. Jagged-delta asymmetry in notch signaling can give rise to a sender/receiver hybrid phenotype. *Proceedings of the National Academy of Sciences of the United States of America*. 2015;112:E402-409

41. Gonzalez CA, Chanson H. Hydraulic design of stepped spillways and downstream energy dissipators for embankment dams. *Dam Engineering*. 2007;17:223-244

42. Meireles I, Cabrita J, Matos J. Non-aerated skimming flow properties on stepped chutes over embankment dams. *Proceedings of the International Junior Researcher and Engineer Workshop on Hydraulic Structures (IJREWHS'06)*. 2006:91-99

43. Neto AS, Amato M, Schultz M. Dissipated energy is a key mediator of vili: Rationale for using low driving pressures. *Annual update in intensive care and emergency medicine 2016*. Springer; 2016:311-321.

44. Parker SE, Mai CT, Canfield MA, Rickard R, Wang Y, Meyer RE, Anderson P, Mason CA, Collins JS, Kirby RS, Correa A, National Birth Defects Prevention N. Updated national birth prevalence estimates for selected birth defects in the united states, 2004-2006. *Birth defects research. Part A, Clinical and molecular teratology*. 2010;88:1008-1016

45. Lee J, Cao H, Kang BJ, Jen N, Yu F, Lee CA, Fei P, Park J, Bohlool S, Lash-Rosenberg L, Shung KK, Hsiai TK. Hemodynamics and ventricular function in a zebrafish model of injury and repair. *Zebrafish*. 2014;11:447-454

46. Sugii Y, Nishio S, Okamoto K, Niu L, Qian M, Wan K. Wall shear stress measurement method based on parallel flow model near vascular wall in echography. *Jpn. J. Appl. Phys*. 2017;56:07JF08

47. Lei Y-C, Tien W-H, Duncan J, Paul M, Ponchaut N, Mouton C, Dabiri D, Rösgen T, Hove J. A vision-based hybrid particle tracking velocimetry (ptv) technique using a modified cascade correlation peak-finding method. *Experiments in fluids*. 2012;53:1251-1268

48. Westerfield M. *The zebrafish book: A guide for the laboratory use of zebrafish (danio rerio)*. University of Oregon Press; 2000.

49. Liebling M, Forouhar AS, Wolleschensky R, Zimmermann B, Ankerhold R, Fraser SE, Gharib M, Dickinson ME. Rapid three-dimensional imaging and analysis of the beating embryonic heart reveals functional changes during development. *Dev Dyn*. 2006;235:2940-2948

50. Taylor JM, Girkin JM, Love GD. High-resolution 3d optical microscopy inside the beating zebrafish heart using prospective optical gating. *Biomedical optics express*. 2012;3:3043

51. Updegrove A, Wilson NM, Merkow J, Lan H, Marsden AL, Shadden SC. Simvascular: An open source pipeline for cardiovascular simulation. *Annals of biomedical engineering*. 2017;45:525-541

52. Myronenko A. Non-rigid image registration regularization, algorithms and applications. 2010

53. Arbia G, Corsini C, Esmaily Moghadam M, Marsden AL, Migliavacca F, Pennati G, Hsia TY, Vignon-Clementel IE, Modeling Of Congenital Hearts Alliance I. Numerical blood

flow simulation in surgical corrections: What do we need for an accurate analysis? *The Journal of surgical research*. 2014;186:44-55

54. Marsden AL, Esmaily-Moghadam M. Multiscale modeling of cardiovascular flows for clinical decision support. *Applied Mechanics Reviews*. 2015;67:030804

55. Marsden AL. Simulation based planning of surgical interventions in pediatric cardiology. *Physics of fluids*. 2013;25:101303

56. Hwang J, Ing MH, Salazar A, Lassegue B, Griendling K, Navab M, Sevanian A, Hsiai TK. Pulsatile versus oscillatory shear stress regulates nadph oxidase subunit expression: Implication for native ldl oxidation. *Circ Res*. 2003;93:1225-1232

# CHAPTER II

## ADVANCED MICROSCOPY TO ELUCIDATE CARDIOVASCULAR INJURY AND REGENERATION: 4D LIGHT-SHEET IMAGING

Baek KI*, Ding Y*, Chang CC*, Chang M, Packard RRS, Hsu JJ, Fei P, Hsiai TK.

* Equal contribution.

Review article, published in ***Progress in Biophysics and Molecular Biology***, 2018, 138; 105-115

## Introduction

Zebrafish (*Danio rerio*) share conserved cardiovascular developmental signaling pathways with mammals, providing a genetically tractable model in developmental research, drug screening, and heart failure studies [1-5]. Zebrafish embryos are optically transparent, allowing for real-time visualization of structural and functional phenotypes [2, 6]. Their small size and short developmental stages facilitate high-throughput genetic, epigenetic, and pharmaceutical analyses [7, 8]. Although mammalian models including mice exhibit the capacity of tissue regeneration during the early stage of development, zebrafish demonstrate structural recovery in response to anatomical amputation, chemotherapy, or redox active ultrafine particles (UFP, diameter < 0.2 μm) in air pollutants [2]. In this review, we introduce our novel imaging technique using our custom-built light-sheet fluorescence microscopy (LSFM) to elucidate zebrafish models of cardiovascular injury and regeneration. We highlight the pathological effects of ambient UFP exposure underlying impaired Notch transcriptional activation complex to promote vascular regeneration [9]. Furthermore, we introduce a novel flow-responsive mechano-metabolic pathway implicated in vascular regeneration [10].

## 1. Light-sheet imaging to study cardiovascular regeneration

Live imaging has transformed biomedical sciences by permitting visualization and analysis of dynamic cellular processes as they occur in their native contexts [11-13]. Conventional methods continue to be useful, but the pursuit of new biological insights often requires higher spatiotemporal resolution in ever-larger, intact samples and, crucially, a gentle touch, such that biological processes continue unhindered. Although confocal microscopy improves spatial resolution and image contrast, using the same path for both illumination and fluorescence detection leads to intensive photo-bleaching and

photo-toxicity with limited penetration depth (100-150 μm) [14, 15]. Multi-photon microscopy utilizes an infrared mode-locked laser as the illumination source and reaches up to 1 mm penetration depth [16, 17], but requires a high numerical aperture (NA > 0.7) and a short laser pulse with a long wavelength. On account of these limitations, LSFM splits the paths so that the illumination plane is perpendicular to the detection angle. Therefore, fluorescence is emitted from the selective focal plane, and only a few fluorescent molecules are excited in the micrometer thickness of the light-sheet.

In comparison to conventional microscopy, LSFM integrates several distinct advantages [18, 19]. (1) LSFM exposes the specimens to at least three orders of magnitude less light energy than confocal and multi-photon fluorescence microscopes over conventional excitation, thus greatly reducing photo-bleaching and photo-toxicity by two to five orders of magnitude [20-22]. In the absence of a pinhole, the loss of energy efficiency of the illumination beam is not more than 5% after transmission through the lenses and mirrors to scan a plane of sample. (2) LSFM allows for illuminating the desired sample area, significantly increasing signal efficiency and axial resolution. The thickness of the light-sheet generated by the illumination lens is the major determinant of the axial resolution whereas the axial resolution of other optical microscopes is predominately determined by the NA of the detection lens. (3) LSFM enables rapid imaging at 100 frames/sec (~400 megapixels/sec) after applying a sCMOS or CCD camera with a large dynamic range, far more than the 10 megapixels/sec of confocal or multi-photon microscopy. (4) LSFM also provides higher signal-to-noise ratio which is over 100:1, while that of confocal microscopy is 60:1 and multi-photon microscopy is only 10:1. LSFM for the present experimental data set was carried out on previously developed systems (**Fig. 1A**) [3, 23-28].

The detection path, including an objective lens (10x/0.25, Nikon), a tube lens (ITL 200, Thorlabs), and switchable optical filters (Semrock, NewYork, USA), was placed orthogonal to the illumination plane for collecting fluorescence signals (**Fig. 1B$_{1\text{-}2}$**). Digital images were recorded with a high frame rate by using two scientific CMOS cameras (ORCA-Flash4.0 V2, Hamamatsu, Japan) for dual-channel detection (**Fig. 1B$_3$**). A diode-pumped solid-state laser containing four wavelengths of 405 nm, 473 nm, 532 nm, and 589 nm (Laserglow Technologies, Toronto, Canada) was used as the illumination source (**Fig. 1B$_4$**). Three common light-sheet configurations were generated to illuminate the embryonic zebrafish heart (150–250 μm), adult zebrafish heart (500–1500 μm), and neonatal mouse heart (3000–5000 μm) (**Fig.1C$_1$**). The confocal region of the light-sheet was used as a uniform planar illumination and was finely stretched to cover the sample's transverse dimension (**Fig.1C$_2$**). The extent of axial projection was directly imaged at the waist of the light-sheet by the profiler, and the confocal range was further reconstructed by stacking the projections (**Fig. 1C$_2$**). The thickness of the light-sheet, defined as the axial full width at half maximum (FWHM) value of the beam waist, was measured at ~5 μm for the embryonic zebrafish heart (i), ~9 μm for the adult zebrafish heart (ii), and ~18 μm for the neonatal mouse heart (iii) (**Fig. 1C$_{1\text{-}2}$**). The lateral confocal regions with respect to these three axial extents were profiled (**Fig. 1C$_2$ i-iii**). The detection objectives were 10x/0.3 (Plan Fluor, Nikon, Japan) for the embryonic zebrafish heart, 4x/0.13 (Plan Fluor, Nikon, Japan) for the adult zebrafish heart, and 1x/0.25 (MVX10, Olympus, Japan) for the neonatal mouse heart to capture the full region-of-interest (ROI). Once the thickness of the light-sheet for excitation and the objective lens for detection were determined, the lateral and axial resolution for each configuration could be obtained by measuring the point spread function (PSF). The

fluorescent point source (polystyrene beads) was imaged by applying the aforementioned three light-sheet configurations and demonstrated the lateral and axial resolution by measuring the FWHMs from x-y, x-z, and y-z plane images (**Fig. 1C$_3$**).

LSFM has the capacity to localize the 4D cellular phenomena with multi-fluorescence channels to study cardiovascular development and regeneration. Unlike commercial systems, including the ASI iSPIM, Zeiss Z.1, Leica SP8 and LaVision Ultramicroscope. Our multi-scale LSFM strategy is capable of rapid imaging acquisition to elucidate mechanisms of vascular regeneration after injury in the zebrafish cardiovascular system. In comparison with the ASI iSPIM, Zeiss Z.1 and Leica SP8 [29-32], we applied dry objective lenses with long-working distances to provide a large field-of-view. We further implemented a cylindrical lens to reshape the Gaussian beam to achieve high spatiotemporal resolution without the need for laser scanning the contracting heart [4, 27]. In addition, our system minimizes photo-bleaching and photo-toxicity due to the planar illumination [4]. In contrast to the LaVision Ultramicrope optimized for mouse brain [33], our LSFM system enables live imaging of zebrafish embryos. Furthermore, our custom-built system adapts a retrospective synchronization algorithm to reconstruct contracting embryonic hearts in 4D [27]. We have also demonstrated a resolution-enhancement method for using the objective lenses with low NA objectives, allowing for multi-scale imaging with a large field-of-view [34]. For these reasons, our custom-built LSFM has the capacity to perform the image-guided study for cardiovascular regeneration.

However, the main limitation of LSFM reside in photon scattering or absorption in the setting of imaging acquisition of large specimens (such as the rodent heart) or interfacing with mismatching refractive indices (from inadequate tissue clearing). Other limitations

include the effect of out-of-focus light to reduce the signal-to-noise ratio. As a result of absorption, refraction, and scattering of coherent light within the tissue, these limitations generate stripe or shadow artifacts to attenuate the image. The lateral resolution of LSFM is lower than that of confocal imaging by the factor of $\sqrt{2}$ when the same objectives are used [35]. The advantages and disadvantages among the different optical modalities are summarized in **Table 1**.

### 1.1. Light-sheet imaging with automated segmentation method to analyze doxorubicin-induced cardiac injury and regeneration

In adult zebrafish, regenerating myocardium electrically couples with uninjured myocardium [36], providing a conserved cardiomyopathy model [37]. Precise assessment of cardiac ventricular architecture remains an imaging challenge due to the small size of the heart. The advent of the chemical clearing method enabled multi-scale imaging of hearts from zebrafish embryos (hundreds of μm in diameter) to adult fish (1-2 mm in diameter) [24, 26]. In the setting of a simplified tissue clearing method using benzyl alcohol-benzyl benzoate (BABB) to improve laser penetration and to achieve optical transparency, we visualized volumetric changes of cardiac morphology in adult zebrafish in response to doxorubicin-induced cardiac toxicity by combining light-sheet illumination with a customized automated segmentation method based on histogram analysis (**Fig. 2A**). Doxorubicin is an anthracycline agent that is commonly used in chemotherapy regimens for patients with a variety of cancers, and it is well known to cause cardiac injury, often limiting its use clinically [38]. The transgenic *Tg(cmlc2:GFP)* zebrafish line was used to visualize ventricular remodeling after doxorubicin chemotherapy. The detection objective is imaged through the liquid-air interface where it is introduced to a spherical

aberration-based PSF extension [39]. The section thickness (1-5 μm) of mechanical scanning was determined based on the Nyquist-Shannon sampling theorem, while image acquisition was done with an exposure time of between 10-50 ms. Thus, the spatial resolution of the LSFM in cross-section varied from 1 μm to 10 μm, while the waist $\omega_0$ ranged from 2 to 9 μm. Reconstructed image stacks underwent alpine interpolation and iterative 3D deconvolution to compensate under-sampling of the camera and to prevent blurred images. A 4-step automated image segmentation process was then applied to the input images for precise assessment of the structural reorganization of the adult zebrafish heart, as previously described [3]. Cardiac volumes assessed with automated segmentation were quantitatively compared following 3, 30, and 60 days of doxorubicin treatment (**Fig. 2B**). Our present data revealed 3 days of doxorubicin treatment led to global cardiac injury and resulted in the reduction of both endocardial and myocardial volumes, followed by ventricular remodeling at day 30, and complete regeneration and restoration of normal architecture at day 60. Furthermore, the automated segmentation method established a well-defined structure of the atrium, ventricle, and bulbus arteriosus, revealing ventricular trabeculae and ultrastructure (**Fig. 3A-B, D**). The computation of the angle between the atrio-ventricular (AV) valves and ventricular-bulbar (VB) valves permitted precise assessment, including the ventricular inflow (dotted yellow line) and outflow path (solid yellow line) (**Fig. 3C**). Our results accentuate the suitability of light-sheet imaging combined with automated segmentation as a high-throughput method to monitor 3D cardiac ultrastructural changes in adult zebrafish, with translational implications to drug discovery and modifiers of chemotherapy-induced cardiomyopathy.

### 1.2. LSFM to study mechano-transduction and vascular dynamics

With the use of the transgenic *Tg*(*flk1:GFP; Gata1:Ds-red*) zebrafish line which drives of the expressions of VEGFR2 as well as erythrocytes, we simultaneously detected circulating erythrocytes and demonstrated flow-mediated vascular regeneration. Our previous study established a zebrafish tail amputation model to seek mechanisms underlying vascular regeneration after injury [10]. The posterior tail segments of the embryos were amputated with a sterilized surgical scalpel under a stereomicroscope and immobilized with low melting agarose in a fluorinated ethylene propylene tube to achieve a uniform refractive index for fluorescence detection. Imaging cellular dynamics across large specimens requires high spatiotemporal resolution, uniform light-sheet thickness and low photo-bleaching/-toxicity. LSFM enables image acquisition of dynamic biophysical and biochemical activities such as blood flow or a beating heart at > 100 frames/sec. The precise alignment of dual-channel detection of LSFM further allows us to concurrently acquire the structure of the vasculature and circulating erythrocytes to perform 2D particle imaging velocimetry (PIV) in the dorsal aorta (DA) (**Fig. 4A-E**). The tail amputation model with LSFM offers a flexible platform to study hemodynamic regulation on endothelial vascular regeneration (**Fig. 4F-G**), providing an entry point to study mechano-transduction in a low Reynolds number system (Re: 100 ~ 1000). Besides, LSFM imaging has also been implemented in various developmental studies, such as 4D reconstruction of contracting zebrafish hearts [18, 27], time-lapse imaging of neural activity and cell lineages in *Drosophila* [40-44], *C. elegans* [32], zebrafish [19, 30, 45-49] and mice [50]. Unique characteristics of LSFM permit long-term imaging of cardiovascular regeneration and development. In comparison to the aforementioned studies, visualization of the periodic contractions of the embryonic heart requires either a 4D synchronization algorithm [18, 28,

[51] or a volumetric imaging method, while capturing dynamic blood flow in 4D is still underway.

## 2. Zebrafish tail amputation model to study vascular regeneration after injury

### 2.1. Exposure to ambient UFP reveals importance of Notch signaling for vascular regeneration

Ambient particulate matter ($PM_{2.5}$) in air pollutants is an emerging epigenetic factor in promoting endothelial dysfunction [52, 53]. Recent epidemiological studies have consistently supported that $PM_{2.5}$ exposure results in elevated risk of cancer, respiratory diseases, and cardiovascular defects during development [54-59]. UFP are a major sub-fraction of $PM_{2.5}$ and comprise a mixture of highly reactive organic chemicals [60] and transition metals [54, 61-63]. Exposure to UFP promotes Jun amino-terminal kinase (JNK) expression to produce a reactive oxygen species (ROS), thereby increasing vascular oxidative stress, and is also implicated in NF-κB-mediated inflammatory responses that induce atherosclerosis and vascular calcification [54, 62-67].

The Notch signaling pathway is an evolutionarily conserved intracellular signaling pathway intimately involved in cell-fate determination [68-72] and regulates initial sprout formation during angiogenesis [73-80]. Upon ligand binding, Notch receptors undergo proteolytic cleavages to release the Notch Intracellular Cytoplasmic Domain (NICD) under regulation of a disintegrin and metalloproteinases (ADAM) family. Following translocation to the nucleus, NICD forms a transcriptional activation complex to induce downstream Notch target genes, including Hairy and enhancer of split-1 (*Hes1*) and *gridlock* [68]. Ablation of Notch1 is associated with developmental retardation resulting in embryonic lethality, whereas dysregulated Notch1 activity in endothelial cells induces aberrant proliferation, resulting in a hyperplastic vascular network [81]. Missense mutation of the

Notch3 gene underlies the development of the degenerative vascular disease known as Cerebral Autosomal-Dominant Arteriopathy with Subcortical Infarcts and Leukoencephalopathy (CADASIL) [82].

To investigate whether UFP mitigate Notch-mediated vascular regeneration, we crossbred the Notch reporter transgenic fish *Tg(tp1:GFP)* with the *Tg(flk1:mCherry)* line to image Notch activity-mediated vascular regeneration. The Epstein-Barr Virus terminal protein 1 (tp1) reporter contains two Notch-responsive elements on the Rbp-Jκ binding sites for NICD, thereby reporting regional Notch1b activation [27]. The control group developed vascular regeneration and formed a loop between the DA and the dorsal longitudinal anastomotic vessel (DLAV) with prominent endothelial Notch activity (as visualized in yellow) on the site of injury at 3 days post amputation (dpa). On the other hand, UFP exposure resulted in significant reduction of vascular endothelial Notch activity followed by disrupted vascular network formation on the injured site. The ADAM10 inhibitor, GI254023X, which inhibits proteolytic activation of the Notch receptor, recapitulated Notch-mediated impaired vascular regeneration. To further investigate whether the reduction of Notch signaling is associated with vascular impairment after the injury, we constructed dominant-negative *Notch1b* (DN-*Notch1b*) mRNA that attenuated Notch signaling by 96%. Approximately 75% of Notch-knockdown embryos underwent aberrant vascular regeneration and network formation, exhibiting embryonic lethality at 5 dpa. *NICD* mRNA micro-injection as a means to up-regulate Notch signaling restored UFP-, ADAM10 inhibitor-, and DN-*Notch1b* mRNA- attenuated Notch activity and consequent vascular regeneration. By using our well-established zebrafish tail amputation model, we provide a molecular basis to assess the effects of UFP on endothelial function for vascular regeneration (**Fig. 5**).

Epidemiological studies consistently support a link between maternal exposure to air pollutants and increased risk of congenital cardiovascular diseases [58]. UFP in air pollutants are the products of incomplete combustion from urban environmental sources, including diesel trucks and gasoline vehicles, and are enriched by elemental and polycyclic aromatic hydrocarbons [19]. Their large surface-to-volume ratio increases potential absorption to the pulmonary and cardiovascular systems [83-85]. UFP exposure via inhalation facilitates plasma lipid metabolite production and increases high-density lipoprotein oxidant capacity to accelerate atherosclerosis in LDLR-null mice [65]. UFP exposure further regulates atherogenic lipid metabolites and promotes macrophage infiltration in the intestine [19], where the composition of the micro-biota is altered to elevate atherogenic lipid metabolite levels. The emerging role of redox-sensitive micro-RNAs (miRs) have been implicated in cellular proliferation [86, 87]. $PM_{2.5}$ have been reported to modulate the levels of a number of miRNAs, including miR-223 and miR-375 [88-90]. Therefore, UFP could regulate the level of miRs for Notch inhibition [91].

Nevertheless, the mechanism underlying endothelial proliferation and vascular regeneration remains elusive due to the demand of high spatial and temporal resolution of real-time 3-D imaging. Scanning methods such as confocal or multi-photon microscopy are able to provide sufficient lateral resolution to reveal the biophysical dynamics at the cellular level but are confined to sequential raster scanning over the specimen. For instance, confocal microscopy allows for capturing angiogenic sprouts at a particular time but is limited in time-lapse imaging due to rapid photo-bleaching [92-94]. However, selective-plane illumination and concurrent detection in a 2D plane enable to implement time-lapse visualization of regenerating endothelial vasculature with the minimal photo-bleaching and photo-toxicity. The signal-to-noise ratio and axial resolution of LSFM are also

improved due to planar illumination; otherwise, the focus of detection gradually degrades in the deep tissue. Therefore, the shorter exposure time, the deeper penetration depth, and the higher spatiotemporal resolution allow for time-lapse imaging of vascular regeneration and cellular dynamics in live zebrafish embryos, and LSFM provides the basis for revealing the mechanisms underlying cardiovascular regeneration and development.

### 2.2. Shear stress modulation of vascular dynamics and regeneration

Hemodynamic blood flow exerts shear stress, cyclic stretch, and hydrostatic pressure on the endothelium [95, 96]. While cyclic stretch plays an important role in maintaining endothelial function, it is well recognized that hemodynamic shear forces mechanically and metabolically modulate vascular endothelial function [97-99]. A complex flow profile develops at the arterial bifurcations, where flow separation and migrating stagnation points create disturbed flow (DF), mediating the focal and eccentric nature of atherosclerotic lesions [100-106]. A recent study examined the role of laminar shear stress in driving expression of vascular endothelial growth factor (VEGF) and endothelial nitric oxide synthase (eNOS)-mediated Protein Kinase C isoform epsilon (PKCε) to modulate endothelial cell (EC) proliferation and lumen formation [107, 108]. Unidirectional pulsatile (PSS) and oscillatory shear stress (OSS) differentially modulate the canonical Wnt/β-catenin pathway to modulate vascular development and regeneration [2, 109], while also being implicated in the differentiation of vascular progenitors during angiogenesis [110, 111]. Endothelial glycolysis is mechano-responsive [112], and ECs are highly glycolytic [113]. ECs further increase the level of glycolytic flux when switching from quiescence to a proliferative state, while the glycolytic enzyme, 6-phosphofructo-2-kinase/fructose-2,6-biphosphatase 3 (PFKFB3), localizes in lamellipodia [114]. As a critical regulator of

glycolysis, PFKFB3 further involves lamellipodia/filopodia extension during vessel formation [113, 114]. Laminar shear stress modulates the expression of Krüppel-like factor 2 (KLF2) to suppress PFKFB3-mediated endothelial glycolysis and vessel sprouting [115], whereas disturbed flow mitigates mitochondrial respiration and increases basal glycolysis and glycolytic capacity [116].

Our recent study with zebrafish supports the notion that PSS and OSS differentially modulate VEGFR-PKCε signaling to induce PFKFB3-mediated glycolytic metabolites for vascular repair [10]. Use of embryonic zebrafish allowed for genetic manipulation of blood viscosity to alter the level of endothelial wall shear stress [117] to modulate the PKCε-PFKFB3 pathway *in vivo* (**Fig. 6A**). *Gata1a* morpholino oligonucleotide (MO) micro-injection prevented erythrocyte production, thereby reducing the level of viscosity-mediated shear stress compared to control (**Fig. 6Ai-ii**). [5, 118]. On the other hand, *EPO* mRNA micro-injection resulted in elevated erythrocytosis as a means of augmenting viscosity-mediated wall shear stress (**Fig. 6Aiii**) [119]. In the transgenic *Tg(flk1:GFP)* zebrafish model of tail regeneration, control *p53* MO injection demonstrated vascular regeneration, as visualized by a closed loop between the DA and the DLAV at 3 dpa. In contrast, suppressing the level of PKCε with MO injection developed aberrant vascular regeneration. Furthermore, micro-injection of *Gata1a* MO delayed vascular regeneration from 3 dpa to 5 dpa. The micro-injection of cardiac troponin T2 (*Tnnt2*) MO to arrest myocardial contraction and subsequent blood flow further attenuated vascular regeneration at 3 dpa, while embryos failed to thrive at 5 dpa. On the other hand, erythropoietin (*EPO*) mRNA micro-injection promoted tail regeneration. As a corollary, *PKCε* mRNA restored vascular regeneration in *Gata1a* MO injected embryos at 3 and 5 dpa (**Fig. 6B**).

In reference to our metabolomic analysis via gas chromatography time-of-flight mass spectrometry (GC-TOF), we elucidated that shear stress regulates glycolytic metabolites, including glucose ($C_6H_{12}O_6$), fructose ($C_6H_{12}O_6$), and dihydroxyacetone ($C_3H_6O_3$, DHA) via PFKFB3. In the zebrafish tail amputation model, exposure to DHA increased the proportion of zebrafish embryos with complete regeneration in the control group, whereas it rescued vascular repair in the absence of PKCε (**Fig. 7**). Our findings support that flow-responsive PKCε modulates endothelial glycolytic metabolites that are implicated in vascular regeneration. The advent of high-throughput "omics" approaches, including epigenomics, transcriptomics, miRnomics, proteomics, and metabolomics [120], has provided new mechanotransduction strategies to discover biomarkers with therapeutic targets.

Current scanning methods are limited by their sequential point-scanning strategy in 2D planes, being insufficient to elucidate hemodynamic shear forces during cardiac morphogenesis. Unlike conventional bright-field microscopy, LSFM applies orthogonal illumination and detection, enabling investigators to selectively localize mechano-transduction to the endocardial endothelial lining within an ultra-thin plane of the sample. Due to the rapid multi-channel detection at the single cellular level, LSFM allows for the simultaneous imaging of the blood flow at the injured site and 3D structure of the vessels, elucidating hemodynamics with underlying the initiation of endocardial trabeculation during cardiac development [27]. In conclusion, LSFM allows for rapid tracking of fluorescently labeled targets in multiple channels, thereby providing a computational basis to quantify blood flow and hemodynamic shear forces.

## Conclusion and Outlook

Zebrafish have been utilized as an emerging developmental model due to a conserved physiology and anatomy with mammals. Its optical transparency at the embryonic stage facilitates direct observation of organogenesis including cardiovascular morphogenesis. While zebrafish comprise a well-established genetic system for studying cardiovascular development and disease, zebrafish demonstrate unique regenerative capacity in response to anatomical or chemotherapy-induced injury. Both high spatiotemporal resolution and deep tissue penetration are required to tracking cardiovascular dynamics, such as the regenerating ventricular ultrastructure. Therefore, LSFM is suitable to monitor spatiotemporal variations of the regenerating cardiovascular system with minimal photo-bleaching /-toxicity, and is also a promising approach to track single blood cells as well as estimating the parabolic velocity distribution of blood flow in the embryonic zebrafish model. In addition, parallel advances in deep learning and virtual reality may lead us to more precisely elucidating cardiovascular architecture and function in future studies. Developing a novel convolutional or recurrent neural network for automatic segmentation will benefit image post-processing procedures that are otherwise limited in accuracy and efficiency by manual segmentation in the setting of large data sets [121-123]. The study of interactive virtual reality establishes an efficient and robust framework for creating a user-directed microenvironment in which we are able to unravel developmental cardiac mechanics and physiology with high spatiotemporal resolution [28, 124-126]. In this review, we address our zebrafish model of injury with a mechanistic approach to understand cardiovascular regeneration. Furthermore, our findings with zebrafish combined with multi-scale light-sheet imaging demonstrate the advantages of light-sheet imaging,

highlighting its role as a novel imaging strategy that can illuminate the mechanisms of cardiovascular injury and repair and further advance the field.

**Acknowledgements**

This study was supported by the National Institutes of Health HL118650 (T.K.H.), HL083015 (T.K.H.), HL111437 (T.K.H.), HL129727 (T.K.H.), T32 training grant HL007895 (J.J.H.), and an AHA Scientist Development Grant 16SDG30910007 (R.R.S.P). Chapter II is a reprint of the article: Baek KI*, Ding YC*, Chang CC*, Chang M, Packard RRS, Hsu JJ, Fei P, Hsiai TK. Advanced microscopy to elucidate cardiovascular injury and regeneration: 4D light-sheet imaging. Prog Biophys Mol Biol. 138, 105-115, 2018, (https://doi.org10.1016/j.pbiomolbio.2018.05.003). Reprint was reproduced with permission from the publisher and all of the co-authors of the publication.

## FIGURES

**Fei *et al*, Sci. Rep., 2016**

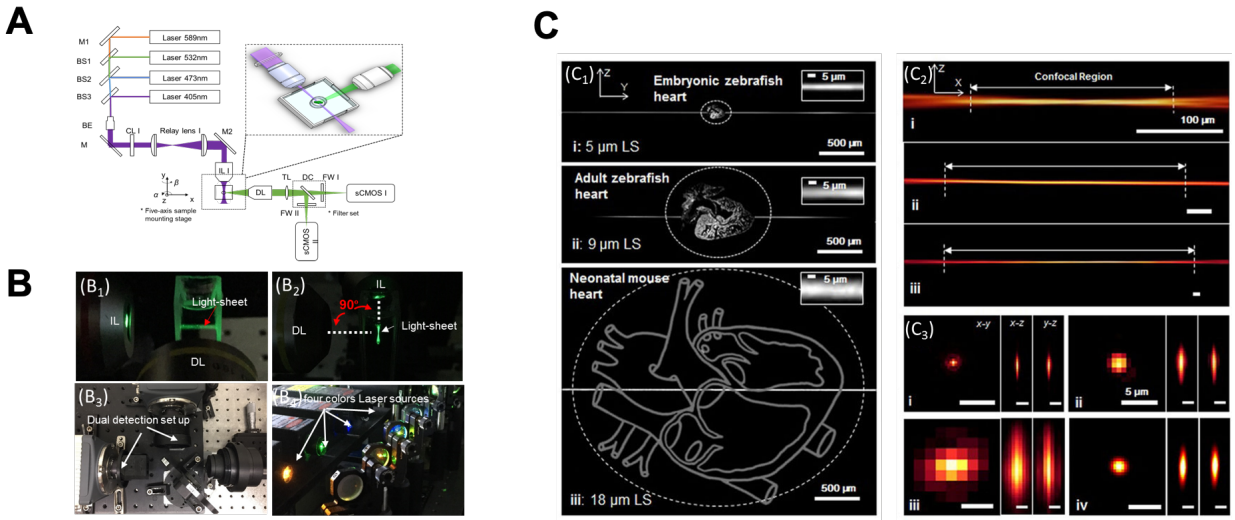


**Figure 1.** Schematic diagram and performance of the fluorescent light-sheet microscope (**A**) Four collimated laser sources were focused through a cylindrical lens and transmitted by illumination lens (IL) to generate a light-sheet sectioning the sample. The objective lens (DL) was positioned orthogonally to the illumination path for fluorescence detection. In addition, the dual-channel detection was achieved using a dichroic mirror and filter sets at the detection arm. The focus of detection needs to be exactly conjugated to the illuminated plane. **($B_1$)** The formation of the light-sheet from the illumination objectives and detected by detection objectives. **($B_2$)** Top view of the light-sheet demonstrated orthogonal relation between IL and DL. **($B_3$)** Four laser wavelengths offer flexibility for different fluorophores. M: mirror; DC: dichroic mirror; BE: beam expander; CL: cylindrical lens; SL: scan lens; TL: tube lens; FW: filter wheel; IL: illumination lens; DL: detection lens. **($B_4$)** The two orthogonal cameras allowed for the capability of simultaneous dual-channel detection. **($C_1$)** The axial confinement of the light-sheet was used for sectioning the (i) embryonic zebrafish, (ii) adult zebrafish, and (iii) neonatal mouse hearts. LS: light-sheet. **($C_2$)** The changes in confocal region corresponded to the area available for light-sheet sectioning. The double-headed arrow line indicates the confocal region, in which

the light-sheet is considered to be uniform. The scale bars are 100 μm in length for the sub-images in (i), (ii) and (iii). **($C_3$)** Imaging a 400 nm fluorescent bead (sub-resolution point source) was compared with the (i) 5 μm LS detected by the 20x/0.5 DL, (ii) 9 μm LS by 10x/0.3 DL, (iii) 18 μm LS by 4x/0.13 DL and (iv) 18 μm LS by 4x/0.13 DL, with resolution enhancement applied. Reproduced in this dissertation with permission from Baek, Ding, Chang *et al*.

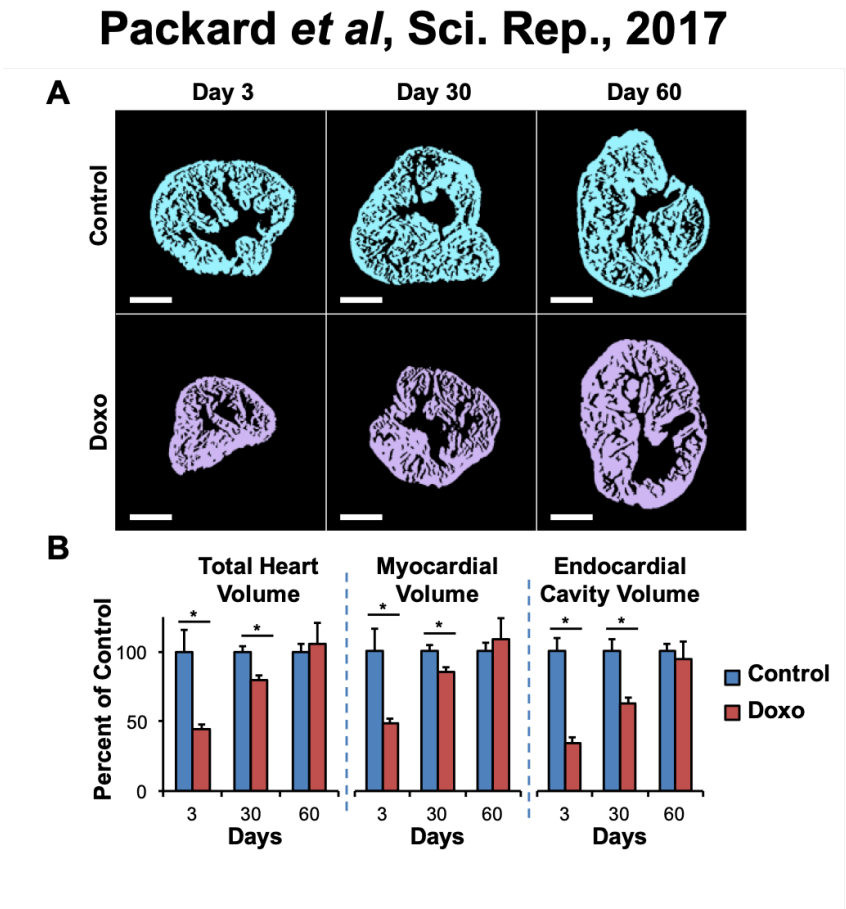


**Figure 2.** Light-sheet imaging to analyze doxorubicin-induced cardiac injury and regeneration Adult zebrafish hearts were isolated at days 3, 30, 60 following intraperitoneal treatment with doxorubicin or control vehicle. **(A)** Control zebrafish hearts exhibited a preserved architecture during the study period. Treatment of doxorubicin induced a dramatic cardiac remodeling leading to an acute reduction in size at day 3, followed by a gradual increase at day 30, and normalization at day 60. **(B)** Total heart, myocardial, and endocardial volumes were quantitatively compared to control values demonstrating the regeneration process following doxorubicin-induced injury (** $P < 0.01$ vs control). Doxo: doxorubicin. Scale bar: 200 μm. Reproduced in this dissertation with permission from Baek, Ding, Chang *et al*.

**Packard *et al*, Sci. Rep., 2017**

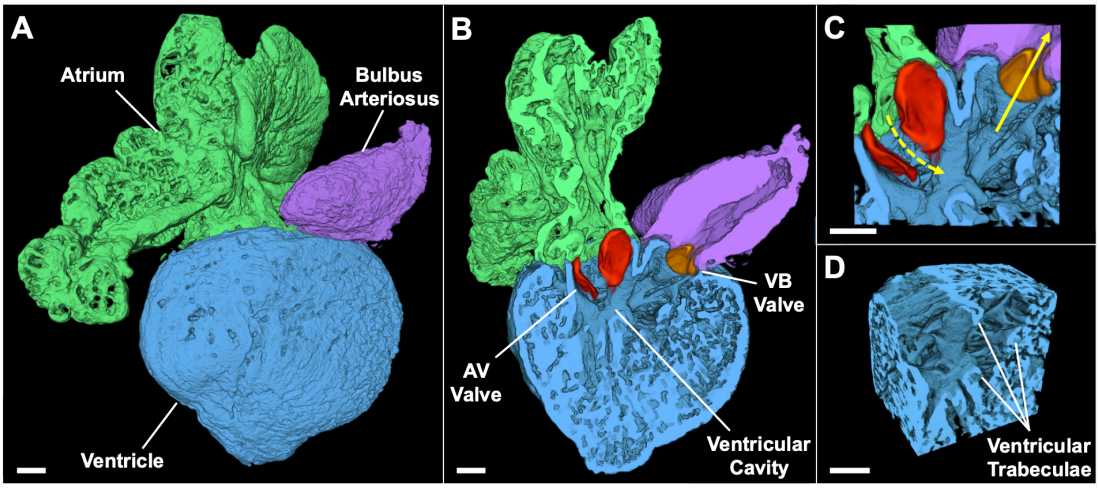


**Figure 3.** 3D rendering of the adult zebrafish heart **(A)** 3-D rendering combined with automated segmentation method provided anatomic structures of the intact atrium, ventricle, and bulbous arteriosus in adult zebrafish heart. **(B)** Precise assessment of zebrafish heart with automated segmentation established a cross-section through the atrium, ventricle, and bulbous arteriosus and demonstrated 2 leaflets of the AV valve (red) and of the VB valve (orange). **(C)** Ventricular inflow (dotted yellow line) and outflow path (solid yellow line) were estimated with computation of the angle between the atrioventricular (AV) valves and ventricular-bulbar (VB) valves. Scale bar: 100 μm. Reproduced in this dissertation with permission from Baek, Ding, Chang *et al*.

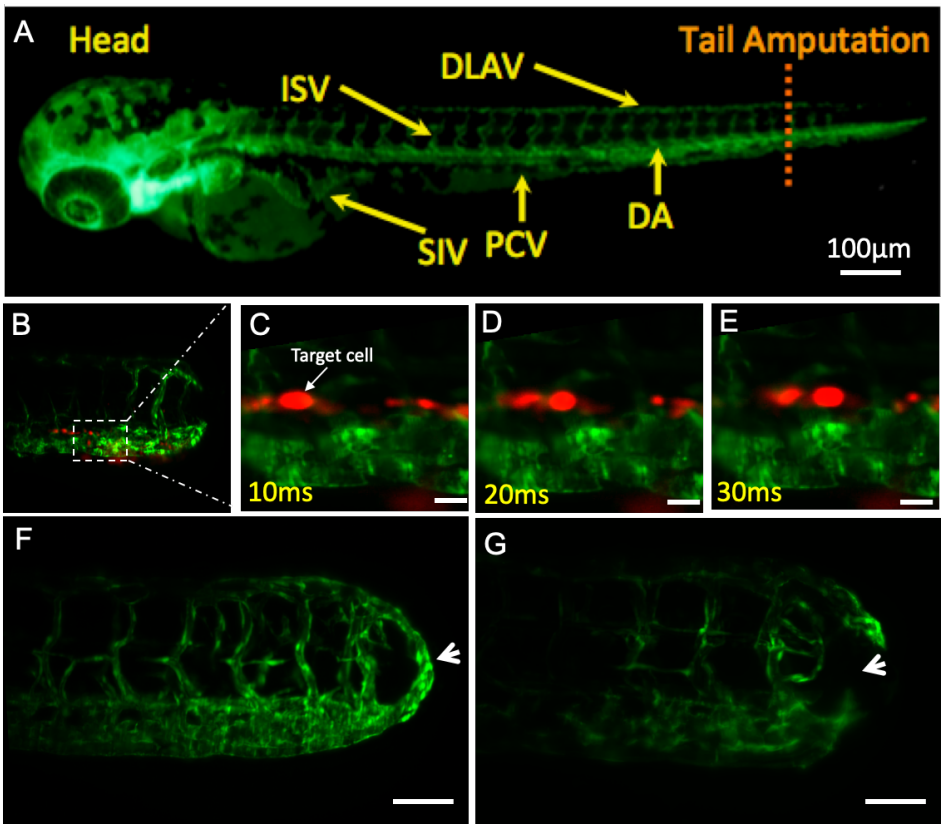


**Figure 4.** Light-sheet imaging of vascular regeneration and circulating erythrocytes in response to tail amputation **(A)** An inverted fluorescence image demonstrated the vasculature (green) and amputation region (dashed line) of a transgenic *Tg(flk1:GFP; Gata1:Ds-Red)* zebrafish embryo at 3 dpf. ISV: intersegmental vessel; DLAV: dorsal longitudinal anastomotic vessel; SIV: subintestinal vessel; PCV: posterior cardinal vein; DA: dorsal aorta. **(B)** LSFM imaging of the erythrocytes (red) adjacent to the site of amputation and regeneration. The dashed white box indicated locations of higher power images in the subsequent panels **(C-E)**. An individual erythrocyte (red) in relation to the vascular endothelial layer (green) was tracked under LSFM at 100 fps. The travel distance and net velocity of each erythrocyte could be measured from the corresponding location difference among images **(C)**, **(D)** and **(E).** The complete **(F)** and incomplete **(G)** vascular regeneration between DLAV and DA were revealed in separate zebrafish embryos at 3 days after tail amputation. Scale bars: 25 μm. Reproduced in this dissertation with permission from Baek, Ding, Chang *et al*.

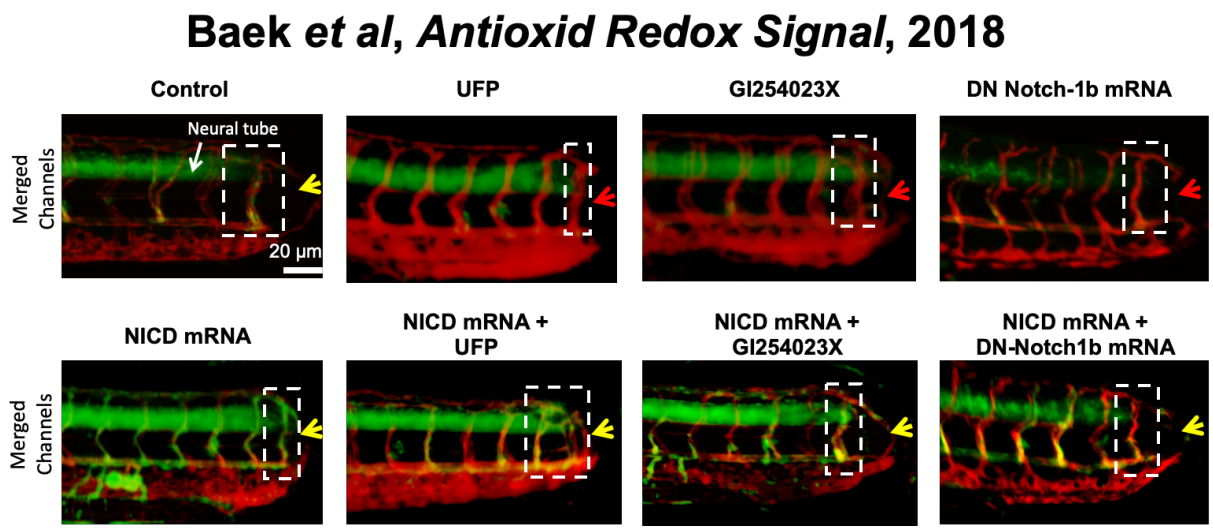


**Figure 5.** Ambient UFP exposure impaired Notch-mediated vascular regeneration. Transgenic *Tg(tp1:GFP; flk1:mCherry)* zebrafish embryos revealed Notch activity in the vasculature, as indicated by the overlapped yellow color, corroborating the role of endothelial Notch activity in the site of vascular repair. The control group developed vascular regeneration at 3 days post tail amputation (dpa). UFP or ADAM 10 inhibitor (GI254023X) treatment attenuated endothelial Notch activity in the site of injury and impaired vascular regeneration. Injection of dominant negative (DN)-*Notch1b* mRNA further attenuated Notch signaling-mediated vascular regeneration. As a corollary, *NICD* mRNA injection upregulated Notch activity and rescued UFP-, ADAM10 inhibitor- or DN-*Notch1b* mRNA-impaired vascular regeneration. Reproduced in this dissertation with permission from Baek, Ding, Chang *et al*.

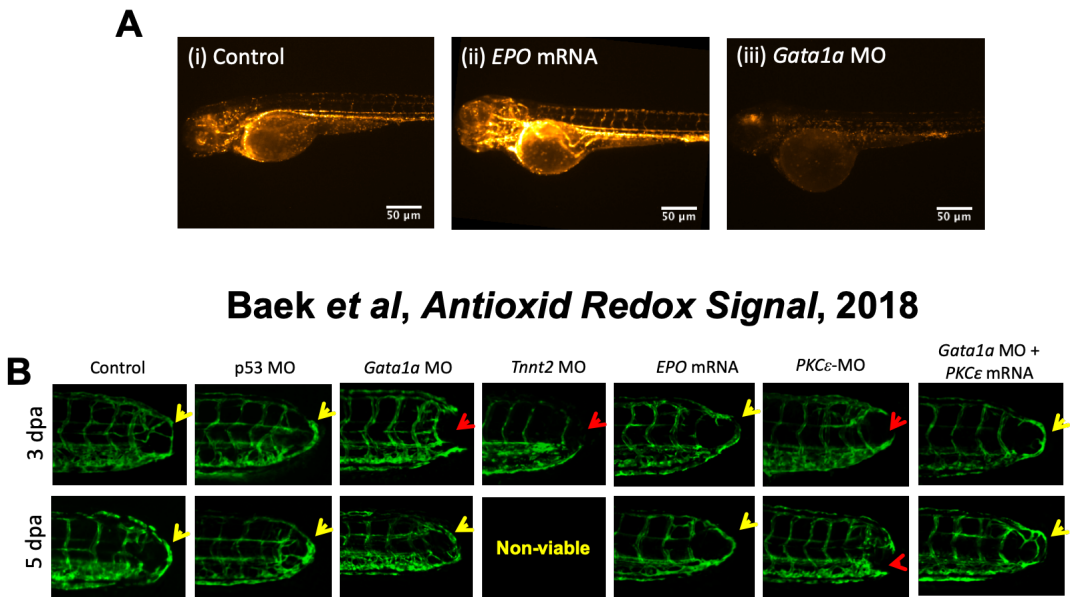


**Figure 6.** Shear stress is implicated in *PKCε*-dependent vascular repair. **(A)** Blood viscosity of the embryonic zebrafish was genetically manipulated to alter the level of endothelial wall shear stress. Compared to control embryos, micro-injection of *Gata1a* MO reduced the level of erythropoiesis and consequent wall shear stress, whereas erythropoietin (*EPO*) mRNA resulted in the opposite effect. **(B)** The control and *p53* MO-injected fish developed vascular repair at 3 dpa (yellow arrows). Reduction of viscosity-mediated shear stress with *Gata1a* MO delayed vascular repair from 3 dpa to 5 dpa. The presence of *Tnnt2* MO to arrest myocardial contractility led impaired vascular repair at 3 dpa, while embryos failed to thrive at 5 dpa (red arrow). On the other hand, increased level of erythropoiesis with *EPO* mRNA promoted vascular regeneration. Silencing *PKCε* with MO attenuated vascular repair at both 3 and 5 dpa, whereas upregulation of *PKCε* mRNA restored vascular impairment in *Gata1a* MO injected embryos. Reproduced in this dissertation with permission from Baek, Ding, Chang *et al*.

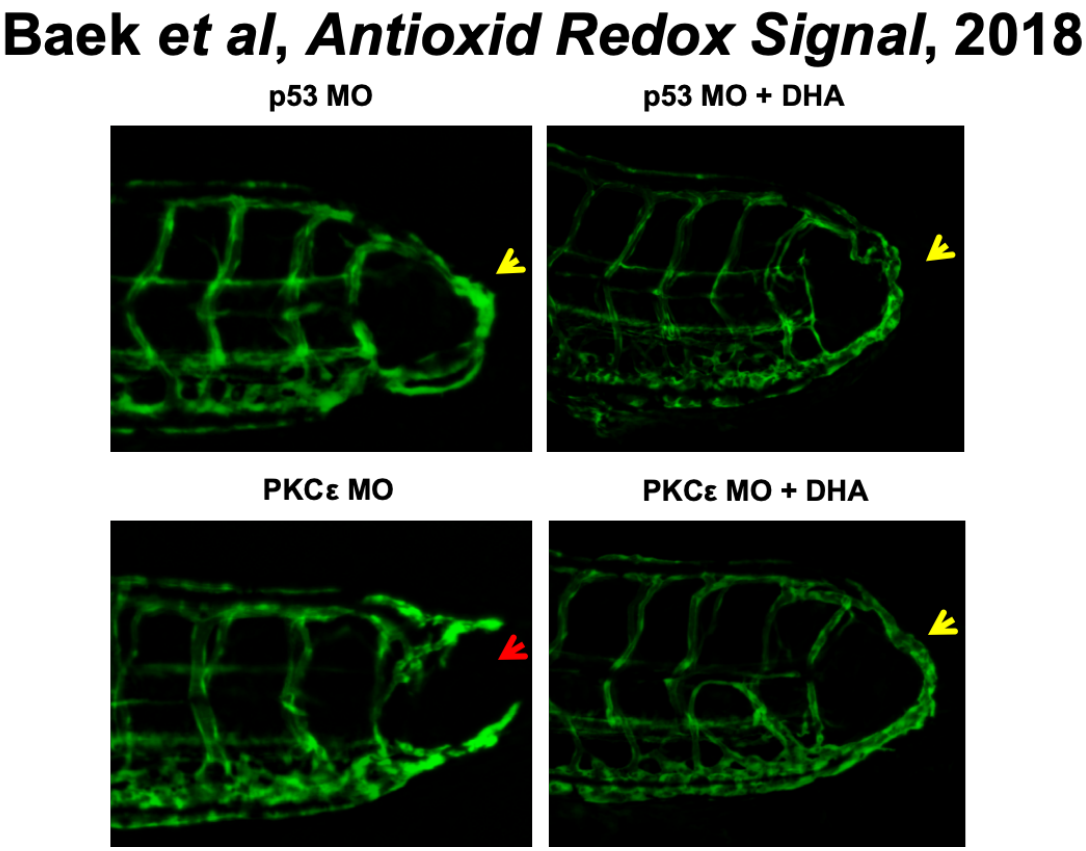


**Figure 7.** Glycolytic metabolite, dihydroxyacetone (DHA) promoted vascular regeneration. Transgenic *Tg(flk1:GFP)* embryos injected with control *P53* MO or *PKCε* MO were treated with or without DHA at 1mg/mL for 3 days after initial vascular injury. Micro-injection of *PKCε* MO resulted in impaired vascular regeneration (red arrow), whereas DHA treatment reversed the effect of *PKCε* MO and promoted vascular regeneration (yellow arrows). Reproduced in this dissertation with permission from Baek, Ding, Chang *et al*.

## Table 1: Comparative advantages and disadvantages among different imaging modalities

| Method | Lateral-Axial Resolution (nm) | Penetration (μm) | Image acquisition time | Advantage | Disadvantage |
|---|---|---|---|---|---|
| **LSFM** | 200-500 | >1000 | ms-s | Low phototoxicity | Big data |
| **CFM** | 200-400 | 150 | s-mins | Optical sectioning | Scanning |
| **WFM** | 250 | --- | ms-mins | Low cost, user-friendly design | Low contrast |
| **SD-CFM** | 200-400 | 150 | s-mins | Rapid Image acquisition | Fixed pinhole |
| **MPM** | 300-500 | 1000 | ms-mins | Penetration depth, intrinsic confocality | Requires high power pulsed laser |
| **STED** | 80-400 | 50 | s-mins | High resolution at confocal speed | Significant photobleaching |
| **PALM/STORM** | 50-100 | 0.1 | mins-hr | Extremely high resolution | Slow image acquisition |

LSFM: light-sheet fluorescence microscopy; CFM: confocal microscopy; WFM: wide-field microscopy; SD-CFM: spinning disk confocal microscopy; MPM: multi-photon microscopy; STED: stimulated emission depletion; PALM: photo-activated localization microscopy; STORM: stochastic optical reconstruction microscopy. Adapted from Ding Y et al., Curr. Cardiol. Rep., 2018.

## References


1. Tzahor E, Poss KD. Cardiac regeneration strategies: Staying young at heart. *Science*. 2017;356:1035-1039

2. Li R, Beebe T, Jen N, Yu F, Takabe W, Harrison M, Cao H, Lee J, Yang H, Han P, Wang K, Shimizu H, Chen J, Lien CL, Chi NC, Hsiai TK. Shear stress-activated wnt-angiopoietin-2 signaling recapitulates vascular repair in zebrafish embryos. *Arterioscler Thromb Vasc Biol*. 2014;34:2268-2275

3. Packard RRS, Baek KI, Beebe T, Jen N, Ding Y, Shi F, Fei P, Kang BJ, Chen P-H, Gau J. Automated segmentation of light-sheet fluorescent imaging to characterize experimental doxorubicin-induced cardiac injury and repair. *Sci. Rep.* 2017;7:8603

4. Power RM, Huisken J. A guide to light-sheet fluorescence microscopy for multiscale imaging. *Nature methods*. 2017;14:360

5. Vermot J, Forouhar AS, Liebling M, Wu D, Plummer D, Gharib M, Fraser SE. Reversing blood flows act through klf2a to ensure normal valvulogenesis in the developing heart. *PLoS biology*. 2009;7:e1000246

6. Opitz R, Maquet E, Huisken J, Antonica F, Trubiroha A, Pottier G, Janssens V, Costagliola S. Transgenic zebrafish illuminate the dynamics of thyroid morphogenesis and its relationship to cardiovascular development. *Developmental biology*. 2012;372:203-216

7. Sun P, Zhang Y, Yu F, Parks E, Lyman A, Wu Q, Ai L, Hu C-H, Zhou Q, Shung K. Micro-electrocardiograms to study post-ventricular amputation of zebrafish heart. *Ann. Biomed. Eng.* 2009;37:890-901

8. Herzog W, Müller K, Huisken J, Stainier DY. Genetic evidence for a noncanonical function of seryl-trna synthetase in vascular development. *Circulation research*. 2009;104:1260-1266

9. Baek KI, Packard RRS, Hsu JJ, Saffari A, Ma Z, Luu AP, Pietersen A, Yen H, Ren B, Ding Y. Ultrafine particle exposure reveals the importance of foxo1/notch activation complex for vascular regeneration. *Antioxidants & redox signaling*. 2018;28:1209-1223

10. Baek KI, Li R, Jen N, Choi H, Kaboodrangi A, Ping P, Liem D, Beebe T, Hsiai TK. Flow-responsive vascular endothelial growth factor receptor-protein kinase c isoform epsilon signaling mediates glycolytic metabolites for vascular repair. *Antioxid Redox Signal*. 2018;28:31-43

11. Amos B. Lessons from the history of light microscopy. *Nat Cell Biol*. 2000;2:E151-152

12. Yuste R. Fluorescence microscopy today. *Nat Methods*. 2005;2:902-904

13. Ntziachristos V, Ripoll J, Wang LV, Weissleder R. Looking and listening to light: The evolution of whole-body photonic imaging. *Nat. Biotechnol.* 2005;23:313-320

14. Huisken J, Swoger J, Del Bene F, Wittbrodt J, Stelzer EH. Optical sectioning deep inside live embryos by selective plane illumination microscopy. *Science*. 2004;305:1007-1009

15. Keller PJ, Stelzer EHK. Quantitative in vivo imaging of entire embryos with digital scanned laser light sheet fluorescence microscopy. *Curr Opin Neurobiol*. 2008;18:624-632

16. Kobat D, Horton NG, Xu C. In vivo two-photon microscopy to 1.6-mm depth in mouse cortex. *J. Biomed. Opt.* 2011;16:106014-106014-106014

17. Horton NG, Wang K, Kobat D, Clark CG, Wise FW, Schaffer CB, Xu C. In vivo three-photon microscopy of subcortical structures within an intact mouse brain. *Nat. Photon.* 2013;7:205-209

18. Mickoleit M, Schmid B, Weber M, Fahrbach FO, Hombach S, Reischauer S, Huisken J. High-resolution reconstruction of the beating zebrafish heart. *Nature methods*. 2014;11:919

19. Chhetri RK, Amat F, Wan Y, Höckendorf B, Lemon WC, Keller PJ. Whole-animal functional and developmental imaging with isotropic spatial resolution. *Nature methods*. 2015;12:1171

20. Huisken J, Stainier DY. Selective plane illumination microscopy techniques in developmental biology. *Development*. 2009;136:1963-1975

21. Santi PA. Light sheet fluorescence microscopy: A review. *J. Histochem. Cytochem.* 2011;59:129-138

22. De Vos WH, Beghuin D, Schwarz CJ, Jones DB, van Loon JJ, Bereiter-Hahn J, Stelzer EH. Invited review article: Advanced light microscopy for biological space research. *Rev. Sci. Instr.* 2014;85:101101

23. Sideris E, Griffin DR, Ding Y, Li S, Weaver WM, Di Carlo D, Hsiai T, Segura T. Particle hydrogels based on hyaluronic acid building blocks. *ACS Biomater. Sci. Engin.* 2016;2:2034-2041

24. Sung K, Ding Y, Ma J, Chen H, Huang V, Cheng M, Yang CF, Kim JT, Eguchi D, Carlo DD, Hsiai TK, Nakano A, Kulkarni RP. Simplified three-dimensional tissue clearing and incorporation of colorimetric phenotyping. *Sci. Rep.* 2016;6:30736

25. Ding Y, Lee J, Ma J, Sung K, Yokota T, Singh N, Dooraghi M, Abiri P, Wang Y, Kulkarni RP. Light-sheet fluorescence imaging to localize cardiac lineage and protein distribution. *Sci. Rep.* 2017;7:42209

26. Fei P, Lee J, Packard RRS, Sereti K-I, Xu H, Ma J, Ding Y, Kang H, Chen H, Sung K. Cardiac light-sheet fluorescent microscopy for multi-scale and rapid imaging of architecture and function. *Scientific reports*. 2016;6:22489

27. Lee J, Fei P, Packard RRS, Kang H, Xu H, Baek KI, Jen N, Chen J, Yen H, Kuo C-CJ. 4-dimensional light-sheet microscopy to elucidate shear stress modulation of cardiac trabeculation. *The Journal of clinical investigation*. 2016;126:1679-1690

28. Baek KI, Packard RR, Hsu JJ, Saffari A, Ma Z, Luu AP, Pietersen A, Yen H, Ren B, Ding Y, Sioutas C, Li R, Hsiai TK. Ultrafine particles exposure reveals the importance of foxo1/notch activation complex for vascular regeneration. *Antioxid Redox Signal*. 2017

29. Keller PJ, Schmidt AD, Wittbrodt J, Stelzer EH. Reconstruction of zebrafish early embryonic development by scanned light sheet microscopy. *science*. 2008;322:1065-1069

30. Wu Y, Wawrzusin P, Senseney J, Fischer RS, Christensen R, Santella A, York AG, Winter PW, Waterman CM, Bao Z. Spatially isotropic four-dimensional imaging with dual-view plane illumination microscopy. *Nature biotechnology*. 2013;31:1032

31. Kumar A, Wu Y, Christensen R, Chandris P, Gandler W, McCreedy E, Bokinsky A, Colón-Ramos DA, Bao Z, McAuliffe M. Dual-view plane illumination microscopy for rapid and spatially isotropic imaging. *nature protocols*. 2014;9:2555

32. Wu Y, Ghitani A, Christensen R, Santella A, Du Z, Rondeau G, Bao Z, Colon-Ramos D, Shroff H. Inverted selective plane illumination microscopy (ispim) enables

coupled cell identity lineaging and neurodevelopmental imaging in caenorhabditis elegans. *Proc Natl Acad Sci U S A*. 2011;108:17708-17713

33. Dodt H-U, Leischner U, Schierloh A, Jährling N, Mauch CP, Deininger K, Deussing JM, Eder M, Zieglgänsberger W, Becker K. Ultramicroscopy: Three-dimensional visualization of neuronal networks in the whole mouse brain. *Nature methods*. 2007;4:331

34. Fei P, Nie J, Lee J, Ding Y, Li S, Yu Z, Zhang H, Hagiwara M, Yu T, Segura T. Sub-voxel light-sheet microscopy for high-resolution, high-throughput volumetric imaging of large biomedical specimens. *bioRxiv*. 2018:255695

35. Cannell M, McMorland A, Soeller C, Pawley J. Handbook of biological confocal microscopy. 2006

36. Lee J, Cao H, Kang BJ, Jen N, Yu F, Lee C-A, Fei P, Park J, Bohlool S, Lash-Rosenberg L. Hemodynamics and ventricular function in a zebrafish model of injury and repair. *Zebrafish*. 2014;11:447-454

37. Ding Y, Sun X, Huang W, Hoage T, Redfield M, Kushwaha S, Sivasubbu S, Lin X, Ekker S, Xu X. Haploinsufficiency of target of rapamycin attenuates cardiomyopathies in adult zebrafishnovelty and significance. *Circ. Res.* 2011;109:658-669

38. Volkova M, Russell R, 3rd. Anthracycline cardiotoxicity: Prevalence, pathogenesis and treatment. *Curr Cardiol Rev*. 2011;7:214-220

39. Tomer R, Lovett-Barron M, Kauvar I, Andalman A, Burns VM, Sankaran S, Grosenick L, Broxton M, Yang S, Deisseroth K. Sped light sheet microscopy: Fast mapping of biological system structure and function. *Cell*. 2015;163:1796-1806

40. Keller PJ, Schmidt AD, Santella A, Khairy K, Bao Z, Wittbrodt J, Stelzer EH. Fast, high-contrast imaging of animal development with scanned light sheet-based structured-illumination microscopy. *Nat Methods*. 2010;7:637-642

41. Truong TV, Supatto W, Koos DS, Choi JM, Fraser SE. Deep and fast live imaging with two-photon scanned light-sheet microscopy. *Nat Methods*. 2011;8:757-760

42. Ahrens MB, Orger MB, Robson DN, Li JM, Keller PJ. Whole-brain functional imaging at cellular resolution using light-sheet microscopy. *Nat Methods*. 2013;10:413-420

43. Tomer R, Khairy K, Amat F, Keller PJ. Quantitative high-speed imaging of entire developing embryos with simultaneous multiview light-sheet microscopy. *Nat Methods*. 2012;9:755-763

44. Vladimirov N, Mu Y, Kawashima T, Bennett DV, Yang CT, Looger LL, Keller PJ, Freeman J, Ahrens MB. Light-sheet functional imaging in fictively behaving zebrafish. *Nat Methods*. 2014;11:883-884

45. Bassi A, Schmid B, Huisken J. Optical tomography complements light sheet microscopy for in toto imaging of zebrafish development. *Development*. 2015;142:1016-1020

46. Schmid B, Shah G, Scherf N, Weber M, Thierbach K, Campos CP, Roeder I, Aanstad P, Huisken J. High-speed panoramic light-sheet microscopy reveals global endodermal cell dynamics. *Nat Commun*. 2013;4:2207

47. Weber M, Scherf N, Meyer AM, Panakova D, Kohl P, Huisken J. Cell-accurate optical mapping across the entire developing heart. *Elife*. 2017;6

48. Forouhar AS, Liebling M, Hickerson A, Nasiraei-Moghaddam A, Tsai H-J, Hove JR, Fraser SE, Dickinson ME, Gharib M. The embryonic vertebrate heart tube is a dynamic suction pump. *Science*. 2006;312:751-753

49. Lenard A, Daetwyler S, Betz C, Ellertsdottir E, Belting H-G, Huisken J, Affolter M. Endothelial cell self-fusion during vascular pruning. *PLoS biology*. 2015;13:e1002126

50. Bouchard MB, Voleti V, Mendes CS, Lacefield C, Grueber WB, Mann RS, Bruno RM, Hillman EM. Swept confocally-aligned planar excitation (scape) microscopy for high-speed volumetric imaging of behaving organisms. *Nature photonics*. 2015;9:113

51. Liebling M, Forouhar AS, Gharib M, Fraser SE, Dickinson ME. Four-dimensional cardiac imaging in living embryos via postacquisition synchronization of nongated slice sequences. *J Biomed Opt*. 2005;10:054001

52. Karimi Galougahi K, Ashley EA, Ali ZA. Redox regulation of vascular remodeling. *Cell Mol Life Sci*. 2016;73:349-363

53. Minicucci MF, Azevedo PS, Paiva SA, Zornoff LA. Cardiovascular remodeling induced by passive smoking. *Inflamm Allergy Drug Targets*. 2009;8:334-339

54. Brook RD, Rajagopalan S, Pope CA, 3rd, Brook JR, Bhatnagar A, Diez-Roux AV, Holguin F, Hong Y, Luepker RV, Mittleman MA, Peters A, Siscovick D, Smith SC, Jr., Whitsel L, Kaufman JD, American Heart Association Council on E, Prevention CotKiCD, Council on Nutrition PA, Metabolism. Particulate matter air pollution and cardiovascular disease: An update to the scientific statement from the american heart association. *Circulation*. 2010;121:2331-2378

55. Brunekreef B, Holgate ST. Air pollution and health. *Lancet*. 2002;360:1233-1242

56. Gorham ED, Garland CF, Garland FC. Acid haze air pollution and breast and colon cancer mortality in 20 canadian cities. *Can J Public Health*. 1989;80:96-100

57. Ritz B, Yu F, Fruin S, Chapa G, Shaw GM, Harris JA. Ambient air pollution and risk of birth defects in southern california. *American journal of epidemiology*. 2002;155:17-25

58. Dadvand P, Rankin J, Rushton S, Pless-Mulloli T. Ambient air pollution and congenital heart disease: A register-based study. *Environmental research*. 2011;111:435-441

59. Hwang BF, Lee YL, Jaakkola JJ. Air pollution and the risk of cardiac defects: A population-based case-control study. *Medicine*. 2015;94:e1883

60. Sardar SB, Fine PM, Mayo PR, Sioutas C. Size-fractionated measurements of ambient ultrafine particle chemical composition in los angeles using the nanomoudi. *Environ Sci Technol*. 2005;39:932-944

61. Lough GC, Schauer JJ, Park JS, Shafer MM, Deminter JT, Weinstein JP. Emissions of metals associated with motor vehicle roadways. *Environ Sci Technol*. 2005;39:826-836

62. Nel A, Xia T, Madler L, Li N. Toxic potential of materials at the nanolevel. *Science*. 2006;311:622-627

63. Zhang Y, Schauer JJ, Shafer MM, Hannigan MP, Dutton SJ. Source apportionment of in vitro reactive oxygen species bioassay activity from atmospheric particulate matter. *Environ Sci Technol*. 2008;42:7502-7509

64. Li R, Ning Z, Cui J, Khalsa B, Ai L, Takabe W, Beebe T, Majumdar R, Sioutas C, Hsiai T. Ultrafine particles from diesel engines induce vascular oxidative stress via jnk activation. *Free Radic Biol Med*. 2009;46:775-782

65. Li R, Navab M, Pakbin P, Ning Z, Navab K, Hough G, Morgan TE, Finch CE, Araujo JA, Fogelman AM, Sioutas C, Hsiai T. Ambient ultrafine particles alter lipid metabolism and hdl anti-oxidant capacity in ldlr-null mice. *J Lipid Res*. 2013;54:1608-1615

66. Araujo JA, Barajas B, Kleinman M, Wang X, Bennett BJ, Gong KW, Navab M, Harkema J, Sioutas C, Lusis AJ, Nel AE. Ambient particulate pollutants in the ultrafine

range promote early atherosclerosis and systemic oxidative stress. *Circ Res*. 2008;102:589-596

67. Pope CA, 3rd, Burnett RT, Thurston GD, Thun MJ, Calle EE, Krewski D, Godleski JJ. Cardiovascular mortality and long-term exposure to particulate air pollution: Epidemiological evidence of general pathophysiological pathways of disease. *Circulation*. 2004;109:71-77

68. Bray SJ. Notch signalling in context. *Nature reviews. Molecular cell biology*. 2016;17:722-735

69. MacKenzie F, Duriez P, Wong F, Noseda M, Karsan A. Notch4 inhibits endothelial apoptosis via rbp-jkappa-dependent and -independent pathways. *The Journal of biological chemistry*. 2004;279:11657-11663

70. Quillard T, Coupel S, Coulon F, Fitau J, Chatelais M, Cuturi MC, Chiffoleau E, Charreau B. Impaired notch4 activity elicits endothelial cell activation and apoptosis: Implication for transplant arteriosclerosis. *Arterioscler Thromb Vasc Biol*. 2008;28:2258-2265

71. Rostama B, Peterson SM, Vary CP, Liaw L. Notch signal integration in the vasculature during remodeling. *Vascular pharmacology*. 2014;63:97-104

72. Walshe TE, Connell P, Cryan L, Ferguson G, Gardiner T, Morrow D, Redmond EM, O'Brien C, Cahill PA. Microvascular retinal endothelial and pericyte cell apoptosis in vitro: Role of hedgehog and notch signaling. *Investigative ophthalmology & visual science*. 2011;52:4472-4483

73. Krebs LT, Xue Y, Norton CR, Shutter JR, Maguire M, Sundberg JP, Gallahan D, Closson V, Kitajewski J, Callahan R, Smith GH, Stark KL, Gridley T. Notch signaling is

essential for vascular morphogenesis in mice. *Genes & development*. 2000;14:1343-1352

74. Baonza A, Garcia-Bellido A. Notch signaling directly controls cell proliferation in the drosophila wing disc. *Proc Natl Acad Sci U S A*. 2000;97:2609-2614

75. Jensen J, Heller RS, Funder-Nielsen T, Pedersen EE, Lindsell C, Weinmaster G, Madsen OD, Serup P. Independent development of pancreatic alpha- and beta-cells from neurogenin3-expressing precursors: A role for the notch pathway in repression of premature differentiation. *Diabetes*. 2000;49:163-176

76. Fre S, Huyghe M, Mourikis P, Robine S, Louvard D, Artavanis-Tsakonas S. Notch signals control the fate of immature progenitor cells in the intestine. *Nature*. 2005;435:964-968

77. Stanger BZ, Datar R, Murtaugh LC, Melton DA. Direct regulation of intestinal fate by notch. *Proc Natl Acad Sci U S A*. 2005;102:12443-12448

78. Pellegrinet L, Rodilla V, Liu Z, Chen S, Koch U, Espinosa L, Kaestner KH, Kopan R, Lewis J, Radtke F. Dll1- and dll4-mediated notch signaling are required for homeostasis of intestinal stem cells. *Gastroenterology*. 2011;140:1230-1240 e1231-1237

79. Hellstrom M, Phng LK, Hofmann JJ, Wallgard E, Coultas L, Lindblom P, Alva J, Nilsson AK, Karlsson L, Gaiano N, Yoon K, Rossant J, Iruela-Arispe ML, Kalen M, Gerhardt H, Betsholtz C. Dll4 signalling through notch1 regulates formation of tip cells during angiogenesis. *Nature*. 2007;445:776-780

80. Lobov IB, Renard RA, Papadopoulos N, Gale NW, Thurston G, Yancopoulos GD, Wiegand SJ. Delta-like ligand 4 (dll4) is induced by vegf as a negative regulator of angiogenic sprouting. *Proc Natl Acad Sci U S A*. 2007;104:3219-3224

81. Artavanis-Tsakonas S, Rand MD, Lake RJ. Notch signaling: Cell fate control and signal integration in development. *Science*. 1999;284:770-776

82. Joutel A, Corpechot C, Ducros A, Vahedi K, Chabriat H, Mouton P, Alamowitch S, Domenga V, Cecillion M, Marechal E, Maciazek J, Vayssiere C, Cruaud C, Cabanis EA, Ruchoux MM, Weissenbach J, Bach JF, Bousser MG, Tournier-Lasserve E. Notch3 mutations in cadasil, a hereditary adult-onset condition causing stroke and dementia. *Nature*. 1996;383:707-710

83. Schulz H, Harder V, Ibald-Mulli A, Khandoga A, Koenig W, Krombach F, Radykewicz R, Stampfl A, Thorand B, Peters A. Cardiovascular effects of fine and ultrafine particles. *J Aerosol Med*. 2005;18:1-22

84. Frampton MW. Systemic and cardiovascular effects of airway injury and inflammation: Ultrafine particle exposure in humans. *Environ Health Persp*. 2001;109:529-532

85. Nemmar A, Hoet PHM, Vanquickenborne B, Dinsdale D, Thomeer M, Hoylaerts MF, Vanbilloen H, Mortelmans L, Nemery B. Passage of inhaled particles into the blood circulation in humans. *Circulation*. 2002;105:411-414

86. Yu B, Zhou S, Wang Y, Qian T, Ding G, Ding F, Gu X. Mir-221 and mir-222 promote schwann cell proliferation and migration by targeting lass2 after sciatic nerve injury. *Journal of cell science*. 2012;125:2675-2683

87. Wu L, Li H, Jia CY, Cheng W, Yu M, Peng M, Zhu Y, Zhao Q, Dong YW, Shao K, Wu A, Wu XZ. Microrna-223 regulates foxo1 expression and cell proliferation. *FEBS letters*. 2012;586:1038-1043

88. Bleck B, Grunig G, Chiu A, Liu M, Gordon T, Kazeros A, Reibman J. Microrna-375 regulation of thymic stromal lymphopoietin by diesel exhaust particles and ambient particulate matter in human bronchial epithelial cells. *J Immunol*. 2013;190:3757-3763

89. Rodosthenous RS, Coull BA, Lu Q, Vokonas PS, Schwartz JD, Baccarelli AA. Ambient particulate matter and microrna in extracellular vesicles: A pilot study of older individuals. *Part Fibre Toxicol*. 2016;13:13

90. Yang L, Hou XY, Wei Y, Thai P, Chai F. Biomarkers of the health outcomes associated with ambient particulate matter exposure. *Sci Total Environ*. 2017;579:1446-1459

91. Li R, Yang J, Saffari A, Jacobs J, Baek KI, Hough G, Larauche MH, Ma J, Jen N, Moussaoui N, Zhou B, Kang H, Reddy S, Henning SM, Campen MJ, Pisegna J, Li Z, Fogelman AM, Sioutas C, Navab M, Hsiai TK. Ambient ultrafine particle ingestion alters gut microbiota in association with increased atherogenic lipid metabolites. *Sci Rep*. 2017;7:42906

92. Gerhardt H, Golding M, Fruttiger M, Ruhrberg C, Lundkvist A, Abramsson A, Jeltsch M, Mitchell C, Alitalo K, Shima D. Vegf guides angiogenic sprouting utilizing endothelial tip cell filopodia. *The Journal of cell biology*. 2003;161:1163-1177

93. Nguyen D-HT, Stapleton SC, Yang MT, Cha SS, Choi CK, Galie PA, Chen CS. Biomimetic model to reconstitute angiogenic sprouting morphogenesis in vitro. *Proceedings of the National Academy of Sciences*. 2013;110:6712-6717

94. Hogan BM, Bos FL, Bussmann J, Witte M, Chi NC, Duckers HJ, Schulte-Merker S. Ccbe1 is required for embryonic lymphangiogenesis and venous sprouting. *Nature genetics*. 2009;41:396

95. Li YS, Haga JH, Chien S. Molecular basis of the effects of shear stress on vascular endothelial cells. *J Biomech*. 2005;38:1949-1971

96. Ando J, Yamamoto K. Effects of shear stress and stretch on endothelial function. *Antioxid Redox Signal*. 2011;15:1389-1403

97. Li R, Jen N, Wu L, Lee J, Fang K, Quigley K, Lee K, Wang S, Zhou B, Vergnes L, Chen YR, Li Z, Reue K, Ann DK, Hsiai TK. Disturbed flow induces autophagy, but impairs autophagic flux to perturb mitochondrial homeostasis. *Antioxid Redox Signal*. 2015;23:1207-1219

98. Lee J, Packard RR, Hsiai TK. Blood flow modulation of vascular dynamics. *Curr Opin Lipidol*. 2015;26:376-383

99. Cheng C, Tempel D, van Haperen R, de Boer HC, Segers D, Huisman M, van Zonneveld AJ, Leenen PJ, van der Steen A, Serruys PW, de Crom R, Krams R. Shear stress-induced changes in atherosclerotic plaque composition are modulated by chemokines. *J Clin Invest*. 2007;117:616-626

100. Chiu JJ, Wang DL, Chien S, Skalak J, Usami S. Effects of disturbed flow on endothelial cells. *Journal of biomechanical engineering*. 1998;120:2-8

101. Dewey Jr CF, Bussolari SR, Gimbrone Jr MA, Davies PF. The dynamic response of vascular endothelial cells to fluid shear stress. *Journal of biomechanical engineering*. 1981;103:177-185

102. Ding Z, Liu S, Wang X, Khaidakov M, Dai Y, Mehta JL. Oxidant stress in mitochondrial DNA damage, autophagy and inflammation in atherosclerosis. *Scientific reports*. 2013;3:1077

103. Frangos JA, Huang TY, Clark CB. Steady shear and step changes in shear stimulate endothelium via independent mechanisms--superposition of transient and sustained nitric oxide production. *Biochem Biophys Res Commun*. 1996;224:660-665

104. Hwang J, Michael H, Salazar A, Lassegue B, Griendling K, Navab M, Sevanian A, Hsiai TK. Pulsatile versus oscillatory shear stress regulates nadph oxidase subunit expression: Implication for native ldl oxidation. *Circulation research*. 2003;93:1225-1232

105. Hwang J, Saha A, Boo YC, Sorescu GP, McNally JS, Holland SM, Dikalov S, Giddens DP, Griendling KK, Harrison DG, Jo H. Oscillatory shear stress stimulates endothelial production of o2- from p47phox-dependent nad(p)h oxidases, leading to monocyte adhesion. *J Biol Chem*. 2003;278:47291-47298

106. Surapisitchat J, Hoefen RJ, Pi X, Yoshizumi M, Yan C, Berk BC. Fluid shear stress inhibits tnf-alpha activation of jnk but not erk1/2 or p38 in human umbilical vein endothelial cells: Inhibitory crosstalk among mapk family members. *Proceedings of the National Academy of Sciences of the United States of America*. 2001;98:6476-6481

107. Koh W, Sachidanandam K, Stratman AN, Sacharidou A, Mayo AM, Murphy EA, Cheresh DA, Davis GE. Formation of endothelial lumens requires a coordinated pkcepsilon-, src-, pak- and raf-kinase-dependent signaling cascade downstream of cdc42 activation. *Journal of cell science*. 2009;122:1812-1822

108. Rask-Madsen C, King GL. Differential regulation of vegf signaling by pkc-alpha and pkc-epsilon in endothelial cells. *Arterioscler Thromb Vasc Biol*. 2008;28:919-924

109. Dejana E. The role of wnt signaling in physiological and pathological angiogenesis. *Circ Res*. 2010;107:943-952

110. Boselli F, Freund JB, Vermot J. Blood flow mechanics in cardiovascular development. *Cell Mol Life Sci*. 2015;72:2545-2559

111. Roman BL, Pekkan K. Mechanotransduction in embryonic vascular development. *Biomechanics and modeling in mechanobiology*. 2012;11:1149-1168

112. Suarez J, Rubio R. Regulation of glycolytic flux by coronary flow in guinea pig heart. Role of vascular endothelial cell glycocalyx. *The American journal of physiology*. 1991;261:H1994-2000

113. De Bock K, Georgiadou M, Carmeliet P. Role of endothelial cell metabolism in vessel sprouting. *Cell Metab*. 2013;18:634-647

114. De Bock K, Georgiadou M, Schoors S, Kuchnio A, Wong BW, Cantelmo AR, Quaegebeur A, Ghesquiere B, Cauwenberghs S, Eelen G, Phng LK, Betz I, Tembuyser B, Brepoels K, Welti J, Geudens I, Segura I, Cruys B, Bifari F, Decimo I, Blanco R, Wyns S, Vangindertael J, Rocha S, Collins RT, Munck S, Daelemans D, Imamura H, Devlieger R, Rider M, Van Veldhoven PP, Schuit F, Bartrons R, Hofkens J, Fraisl P, Telang S, Deberardinis RJ, Schoonjans L, Vinckier S, Chesney J, Gerhardt H, Dewerchin M, Carmeliet P. Role of pfkfb3-driven glycolysis in vessel sprouting. *Cell*. 2013;154:651-663

115. Doddaballapur A, Michalik KM, Manavski Y, Lucas T, Houtkooper RH, You X, Chen W, Zeiher AM, Potente M, Dimmeler S, Boon RA. Laminar shear stress inhibits endothelial cell metabolism via klf2-mediated repression of pfkfb3. *Arterioscler Thromb Vasc Biol*. 2015;35:137-145

116. Wu D, Huang RT, Hamanaka RB, Krause M, Oh MJ, Kuo CH, Nigdelioglu R, Meliton AY, Witt L, Dai G, Civelek M, Prabhakar NR, Fang Y, Mutlu GM. Hif-1alpha is required for disturbed flow-induced metabolic reprogramming in human and porcine vascular endothelium. *Elife*. 2017;6

117. Galloway JL, Wingert RA, Thisse C, Thisse B, Zon LI. Loss of gata1 but not gata2 converts erythropoiesis to myelopoiesis in zebrafish embryos. *Dev Cell*. 2005;8:109-116

118. Kulkeaw K, Sugiyama D. Zebrafish erythropoiesis and the utility of fish as models of anemia. *Stem cell research & therapy*. 2012;3:55

119. Chu C-Y, Cheng C-H, Chen G-D, Chen Y-C, Hung C-C, Huang K-Y, Huang C-J. The zebrafish erythropoietin: Functional identification and biochemical characterization. *FEBS letters*. 2007;581:4265-4271

120. Simmons RD, Kumar S, Jo H. The role of endothelial mechanosensitive genes in atherosclerosis and omics approaches. *Arch Biochem Biophys*. 2016;591:111-131

121. Lawrence S, Giles CL, Tsoi AC, Back AD. Face recognition: A convolutional neural-network approach. *IEEE Trans Neural Netw*. 1997;8:98-113

122. Shelhamer E, Long J, Darrell T. Fully convolutional networks for semantic segmentation. *IEEE Trans Pattern Anal Mach Intell*. 2017;39:640-651

123. Zheng S, Jayasumana S, Romera-Paredes B, Vineet V, Su Z, Du D, Huang C, Torr PH. Conditional random fields as recurrent neural networks. *Proceedings of the IEEE International Conference on Computer Vision*. 2015:1529-1537

124. Peng H, Ruan Z, Long F, Simpson JH, Myers EW. V3d enables real-time 3d visualization and quantitative analysis of large-scale biological image data sets. *Nat Biotechnol*. 2010;28:348-353

125. Eliceiri KW, Berthold MR, Goldberg IG, Ibanez L, Manjunath BS, Martone ME, Murphy RF, Peng H, Plant AL, Roysam B, Stuurman N, Swedlow JR, Tomancak P, Carpenter AE. Biological imaging software tools. *Nat Methods*. 2012;9:697-710

126. Peng H, Tang J, Xiao H, Bria A, Zhou J, Butler V, Zhou Z, Gonzalez-Bellido PT, Oh SW, Chen J, Mitra A, Tsien RW, Zeng H, Ascoli GA, Iannello G, Hawrylycz M, Myers E, Long F. Virtual finger boosts three-dimensional imaging and microsurgery as well as terabyte volume image visualization and analysis. *Nat Commun*. 2014;5:4342

# CHAPTER III

# ULTRAFINE PARTICLE EXPOSURE REVEALS THE IMPORTANCE OF FORK HEAD BOX SUBFAMILY O1 / NOTCH ACTIVATION COMPLEX FOR VASCULAR REGENERATION

Baek KI, Packard RRS, Hsu JJ, Saffari A, Ma Z, Luu AP, Pietersen A, Yen H, Ren B, Ding Y, Sioutas C, LiR, Hsiai TK

Original article, published in ***Antioxidants and redox signaling***, 2018, May 1; 28(13):1209-1223

## Introduction

Vascular regeneration involves complex signaling pathways, and exposure to ambient particulate matter ($PM_{2.5}$, d < 2.5 μm) is an emerging epigenetic factor to impair vascular regeneration [1, 2]. While $PM_{2.5}$ in air pollution significantly contributes to cancer, cardiovascular, and respiratory diseases [3-6], recent epidemiological studies indicated an increased risk of cardiovascular defects during development [7, 8]. Ultrafine particles (UFP, diameter < 0.2 μm) are the highly redox-active subtraction of $PM_{2.5}$ rich in reactive organic chemicals [9] and transition metals [3, 10-12]. UFP exposure activates JNK to produce reactive oxygen species (ROS), and induces NF-κB-mediated inflammatory responses to initiate atherosclerosis and vascular calcification[11-17]. However, the mechanism whereby exposure to ambient UFP impairs vascular regeneration remains unexplored.

The Notch signaling pathway is an evolutionarily conserved intercellular signaling pathway critical in cell-fate specification and embryonic development[18-23]. Upon ligand binding, the Notch receptor undergoes proteolytic cleavages to release Notch Intracellular Cytoplasmic Domain (NICD). Following translocation to the nuclei, NICD forms a transcriptional activation complex consisting of recombination signal-binding protein for immunoglobulin J region (Rbp-Jκ), suppressor of hairless, Lag-1(CSL), and mastermind-like (MAML) to induce Notch target genes [24].

The Forkhead box O subfamily (FOXO) protein is a transcription factor that regulates hormonal control, cellular metabolism, and differentiation [25]. Analogous to Notch signaling in cell fate and vascular maturation, FOXO1 (*FKHR*), the dominant isoform of the Forkhead box O subfamily, is essential for vascular growth. Conditional deletion of FOXO1 results in abnormal sprout formation and vascular migration, resulting in a hyperplastic vascular network, whereas constitutively active FOXO1 suppresses vascular

expansion, resulting in a sparse vascular network [26]. Endothelial FOXO1 physically interacts with canonical Notch signaling by binding to CSL, enhancing co-repressor clearance to promote Notch signaling [27]. FOXO1 ablation recapitulates the Notch1 knockout phenotype, whereas the FOXO1 interaction with NICD promotes Notch1 activation in vascular, muscular, and neuronal differentiation [27].

In this context, we assessed whether exposure to ambient UFP inhibits Notch signaling via FOXO1/Notch activation complex to impair vascular regeneration. Following tail amputation in embryonic zebrafish, vascular regeneration occurred, whereas UFP exposure attenuated Notch activity and impaired regeneration. UFP further down-regulated FOXO1 expression, resulting in reduced FOXO1 and NICD co-localization. While rescue with *NICD* mRNA partially restored Notch activity, rescue with *FOXO1* mRNA reversed UFP-mediated reduction in Notch activity, leading to restored vascular network and blood flow to the amputated site. Thus, the redox active UFP down-regulate FOXO1-mediated Notch signaling, revealing the essential role of FOXO1/Notch activation complex in vascular regeneration.

## Materials & Methods

### Ultrafine particle collection

UFP were collected at the University of Southern California (USC) campus near downtown Los Angeles, California. UFP are characterized by a mixture of particulate pollutants, including ambient PM from heavy duty diesel trucks, light duty gasoline vehicles, and PM generated by photochemical oxidation of primary organic vapors [62]. UFP were collected with High Volume Particle Sampler, operating at 400 liters per minute [63], on Zefluor PTFE membrane filters (3 μm, Pall Life Sciences, NY). Collected PM

samples were extracted from the filter substrates by soaking and vortexing in ultrapure Milli-Q water followed by sonication and neutralization. Metal and organic content of the UFP samples were quantified using inductively coupled plasma mass spectrometry (ICP-MS) and Siever 900 Organic Carbon Analyzer respectively as reported [64, 65]. Mass fraction of the total organic carbon (TOC) and major metals (in units of ng/μg UFP) are summarized in **Fig. S1**.

**Vascular endothelial cell culture and exposure to UFP**

Human aortic endothelial cells (HAEC) were cultured in endothelial growth medium (Cell Applications, San Diego, CA) supplemented with 5% Fetal Bovine Serum (FBS), 1% penicillin/streptomycin (Life Technologies, NY) and 0.1% fungicide. HAEC were propagated for experiments between passages 4 and 7, and were treated with UFP, ADAM10 inhibitor, GI254023X, or proteasome inhibitor, MG-132 (Sigma-Aldrich, MO) at indicated concentrations diluted in M199 media (Life Technologies, NY).

**Preparation of NICD, FOXO1, and dominant negative *Notch1b* (DN-*Notch1b*) mRNA**

Rat NICD and mouse FOXO1 cDNA were amplified from donor plasmids and cloned into the plasmid pCS2+ at the BamHI/EcoRI sites (for NICD) and BamHI/XbaI sites (for FOXO1), respectively. Zebrafish DN-*Notch1b* cDNA was amplified from zebrafish cDNA with primers excluding the intracellular domain and cloned into pCS2+ at EcoRI/XhoI sites. Clones with insert of interest were selected by PCR screening and validated with sequencing. mRNAs were prepared using the mMessage SP6 kit (Invitrogen, CA) following the manufacturer's instruction. The *in vitro* transcribed mRNAs were purified by using a total RNA isolation kit (Bio-Rad, CA) for *in vivo* rescue experiments.

**Notch reporter activity assay**

HEK-293 cells were grown to sub-confluence in 24-well plates. The cells were transfected with the Notch reporter plasmid pJH26 with or without control or dominant-negative *Notch1b* (DN-*Notch1b*) plasmid overnight using Lipofectamine 2000 (Thermo Fisher Scientific, MA). The cells were treated overnight with UFP at different concentrations in M199 containing 0.1 % FBS**.** The cells were lysed in Passive Lysis Buffer (Promega, WI), and luciferase activities were quantified with a Luminometer using Bright-Glow substrate (Promega, WI).

**Quantitative real-time PCR analysis**

Notch signaling related gene mRNA expression patterns, including Notch ligands *DLL4, JAG1* and *JAG2,* Notch receptor *Notch1b*, downstream target *Hey2,* and *FOXO1*, were assessed by quantitative real-time PCR (qRT-PCR). RNA was isolated using the Bio-Rad total RNA kit (Bio-Rad, CA), and synthesized into cDNA using iScript cDNA synthesis kit (Bio-Rad, CA). Synthesized cDNAs were diluted in the molecular biology reagent water (Sigma-Aldrich, MO) for PCR amplification with qPCR master mix (Applied Biological Materials Inc., Canada). The individual mRNA expression patterns were normalized to actin expression. Sequence of primers and MOs are listed in **Table 1**.

**Western blot analysis and immunoprecipitation**

HAEC treated with or without UFP were lysed with standard RIPA buffer supplemented with phosphatase inhibitor as previously described [66]. Cytosolic and nuclear lysates were prepared as previously described [67]. Protein concentrations of each sample were determined by DCP assay. Western blotting was done as previously described [66] with anti-FOXO1 (H-128, Santa Cruz Biotechnology Inc., TX), anti-MAML1 (EMD Millipore Inc., CA) and anti-NICD (V1744, Cell Signaling Technology Inc., MA). Equal loading was verified with anti-β-tubulin (AA2, Santa Cruz Biotechnology Inc., TX). Blot densitometry

was performed with the FluorChem FC2 imaging software for chemiluminescence. Immunoprecipitation of FOXO1 and NICD was performed with Pierce Crosslink magnetic IP/CI-IP kit (Thermo Fisher Scientific, MA) following the manufacturer's instruction. Elution of imunoprecipitation was neutralized with neutralize buffer (Thermo Fisher Scientific, MA) for Western blot analysis.

**Assessment of vascular regeneration with the transgenic *Tg*(*fli1:GFP*) zebrafish tail amputation model**

The transgenic *Tg(fli1:GFP)* zebrafish line, in which vascular endothelial cells were labeled with GFP under the promoter of *Fli1* (also known as *ERGB*), was used to image the vascular regeneration. *Tg(fli1:GFP)* fish embryos were injected with or without NICD mRNA, P53 control MO (GeneTools LLC, OR), FOXO1 MO (GeneTools LLC, OR), FOXO1 mRNA (2-4 picograms), or dominant negative (*DN)-Notch1b* mRNA, and were cultured in standard E3 medium supplemented with 0.05% methylene blue at 28.5 °C for 3 days. At 3 days post fertilization (dpf), approximately 100 μm of the posterior tail segments was amputated using a clean razor blade under a phase contrast microscope (Zeiss, Germany). Embryos were then returned to fresh E3 medium, or E3 medium with UFP or ADAM 10 inhibitor. At 3 days post tail amputation (dpa), embryonic zebrafish were randomly picked and immobilized in neutralized 0.02% tricaine solution (Sigma-Aldrich, MO), and were mounted in 1-2% low melting agarose (Sigma-Aldrich, MO) on a glass coverslip to image regeneration of blood vessels with confocal microscopy (Zeiss, Germany).

**Notch activity in double transgenic *Tg(tp1:GFP; flk1:mCherry)* embryos**

The *Tg(tp1:GFP)* Notch reporter line was crossbred with the *Tg(flk1:mCherry)* line to localize endothelial Notch signaling. NICD mRNA, FOXO1 MO, and FOXO1 mRNA were

micro-injected to modulate Notch signaling and to elucidate FOXO1/Notch cooperation. At 6 dpf (3 dpa), embryos were randomly selected to image Notch activation in the central nervous system and in the amputated tail. Embryos from the remaining group were sorted and treated with and without UFP and ADAM10 inhibitor. After 3 days of treatment, Notch signaling localized in the vasculature was scanned at 3-5μm intervals in the Z direction using dual channel confocal microscopy (Zeiss, Germany). Images of Notch activity and the vascular endothelial layer were acquired and superimposed to visualize endothelial Notch activation. Images from each channel are displayed as **Fig. S8**. Stacked images from both channels were projected onto a single plane using ImageJ to visualize 3-D Notch activation.

**Immunofluorescence staining**

Following UFP exposure, HAECs were fixed with 4% PFA and stained with antibody against NICD and FOXO1 diluted in 2% BSA (Sigma Aldrich, MO). Images were acquired by using dual channel confocal microscopy (Zeiss, Germany) and superimposed by using ImageJ.

**Visualization of FOXO1/NICD co-localization.**

To accentuate co-localizations of NICD and FOXO1, we customized a MATLAB (Mathworks, MA) algorithm. Multi-level image thresholds were applied for segmenting the single slice in each channel. Threshold levels for each channel were manually chosen to generate binary masks of the slice. Pixels defined with binary masks were merged together and visualized as overlapping regions, while the remaining regions were regarded as background.

**FOXO1 knockdown**

Scrambled (Qiagen, CA) and FOXO1 siRNA (Thermo Fisher Scientific) were transfected to HAEC with Lipofectamine 2000 (Invitrogen, CA) as previously described [13]. To confirm FOXO1 knockdown, cells were applied to immunofluorescence staining and imaged under fluorescent microscopy (Zeiss, Germany) at 48 hours post transfection.

**Endothelial cell migration and tube formation assays**

For migration assays, human aortic endothelial cell (HAEC) monolayers at confluence were scratched with 200 μL pipette tips. After the scratch, cells were treated with or without UFP at 25 μg/mL in M199 media (Life Technologies, NY). Cell migration was imaged under phase contrast microscopy (Olympus IX 70) at 4, 8, 12, and 24 hrs. For the quantification of cell migration, distances between each inner border of cells was assessed using ImageJ. For tube formation assays, confluent HAEC were pre-treated with or without UFP at 25 μg/mL and re-suspended in DMEM (Invitrogen, CA) supplemented with 25 ng/mL VEGF and 5% FBS. Cells were then added to 96-well plates coated with growth factor-reduced Matrigel (BD Biosciences, CA) and were incubated with or without UFP. Tube formation was imaged under phase contrast microscopy at 4, 8, 12, and 24 hrs.

**Quantification of the regenerated intersegmental vessels**

To quantify changes in vascular repair, we used Amira 3D imaging software. The whole vasculature on the posterior tail segment was masked (purple). The area of regenerated vessels was derived manually by designating segmental vessels (pink) connecting the DA and the DLAV (**Fig. S4**).

**Imaging blood flow on the tail post regeneration**

Double transgenic *Tg(fli1:GFP; gata1:DS-RED)* zebrafish underwent tail amputation at 3 dpf, and were maintained with or without UFP at 25 μg/mL for 3 days. At 3 dpa, fish were

immobilized and placed in 1-2% low melting agarose to image the circulation of erythrocytes through the regenerated vessel. Images of the blood flow and endothelial layer were taken separately with QIcam at 20-30 frames per second (fps). Images were superimposed by using Corel imaging software.

**Wholemount zebrafish immunofluorescence staining**

Wild type zebrafish embryos were injected with P53 MO and FOXO1 MO (GeneTools LLC, OR) respectively, and were maintained in standard E3 medium at 28.5 °C for 3 days. At 3 dpf, embryos were fixed in 4% PFA solution overnight and were subjected to pure acetone for dehydration. Embryos were then rehydrated with 0.2% PBST and were blocked with 2% BSA (Sigma Aldrich, MO). Zebrafish embryos underwent 24 hours of incubation with FOXO1 targeted antibody (C-9, Santa Cruz Biotechnology Inc., TX) to assess reduction of FOXO1. Fluorescent images were acquired using a confocal microscope (Zeiss, Germany) by mounting embryos in 1-2% low melting agarose.

**Statistical analysis**

Data were expressed as mean ± standard deviation and compared among separate experiments. Unpaired two-tail *t* test and 2 proportion z-test were used for statistical comparisons between 2 experimental conditions. $P$ values $< 0.05$ were considered significant. Comparisons of multiple values were made by one-way analysis of variance (ANOVA) and statistical significance for pairwise comparison was determined by using the Tukey test.

## Results

**UFP exposure impaired vascular regeneration**

To assess the effects of UFP on vascular regeneration, we used the transgenic *Tg(fli1:GFP)* zebrafish embryos to visualize the vascular endothelium in response to tail

amputation at 3 days post fertilization (dpf) (**Figs. 1A-B**). Embryos in the control group developed a complete loop formation connecting the dorsal aorta (DA) with the dorsal longitudinal anastomotic vessel (DLAV) at 3 days post amputation (dpa) (**Fig. 1C**), accompanied with restored blood flow to the amputated site (**Supplemental Video 1A**), whereas UFP-exposed embryos developed a disrupted vascular network with aberrant blood flow (**Fig. 1D**) (**Supplemental Video 1B**). Impaired vascular regeneration was seen in 77% of the UFP-exposed embryos as compared to 20% of the wild type (WT) embryos (* $P < 0.05$, n = 20 for WT, n=28 for UFP) (**Fig. 1E**). As a corollary to the zebrafish model of vascular endothelial injury and regeneration, UFP inhibited both endothelial cell migration and tube formation (**Fig. S2**). Thus, UFP exposure impaired vascular repair.

**UFP exposure down-regulated Notch-related genes**

To assess Notch signaling in response to UFP exposure, we used the pJH26 Notch reporter. UFP significantly reduced Notch activity in human aortic endothelial cells (HAEC) in a dose-dependent manner (* $P < 0.05$ vs. control, n = 3) (**Fig. 2A**), accompanied with down-regulation of Notch signaling-related genes, including Notch ligand *Dll4* and Notch target *Hes1*, in a dose- and time-dependent manner (* $P < 0.05$ vs. control, n = 3) (**Figs. 2B-C**). In the zebrafish embryos, UFP exposure also down-regulated Notch signaling-related genes, including Notch ligands (*JAG1* and *JAG2*), the Notch receptor (*Notch1b*), and Notch targets (*Hey2* and *Hes1*) (* $P < 0.05$ vs. control, n = 3) (**Fig. 2D**). The UFP-mediated attenuation in Notch signaling was corroborated by ADAM10 inhibitor (GI254023X) that inhibits Notch receptor activation (**Fig. 2D**). Thus, UFP inhibited Notch activity and down-regulated Notch-related mRNA expression in both HAEC and zebrafish embryos.

**UFP-attenuated Notch signaling impaired vascular regeneration**

We further performed gain- and loss-of-function analyses to validate Notch signaling-mediated vascular regeneration in the transgenic *Tg(fli1:GFP)* embryos. Similar to the effects of UFP, ADAM10 inhibitor, GI254023X, impaired vascular regeneration after tail amputation (* $P < 0.05$, n = 20) (**Fig. 3A-B**). However, rescue with *NICD* mRNA attenuated the proportion of embryos with ADAM10 inhibitor- and UFP-impaired vascular regeneration from 65% to 31% and 80% to 31%, respectively (* $P < 0.05$, n = 20) (**Figs. 3C**). To further assess whether the reduction in Notch signaling impairs vascular regeneration, we constructed a dominant-negative *Notch 1b* (DN-*Notch1b*) mRNA that inhibits 96% of Notch signaling (**Fig. S3**). 75% of embryos injected with DN-*Notch1b* mRNA developed abnormal vascular regeneration and exhibited embryonic lethality (* $P < 0.05$, n = 20), which was reduced to 50% by *NICD* mRNA rescue (**Fig. 3C**). In agreement with DN-*Notch1b* mRNA, UFP exposure during embryogenesis retarded development and promoted embryonic lethality (**Fig. S5**). Hence, UFP-attenuated Notch signaling is implicated in impaired vascular regeneration.

**Reduced endothelial Notch activity impaired vascular regeneration**

We further crossbred the Notch reporter transgenic fish *Tg(tp1:GFP)* with *Tg(flk1:mCherry)* line to demonstrate Notch activity-mediated vascular regeneration. The *tp1* (Epstein Barr Virus terminal protein 1) in the Notch reporter line contains two Rbp-Jκ binding sites for NICD, thereby reporting regional Notch1b activation [28]. Vascular endothelial Notch activity (as visualized in yellow) was reduced following either UFP exposure, ADAM10 inhibitor treatment, or injection of DN-*Notch1b* mRNA, accompanied with incomplete vascular loop closure (* $P < 0.05$ vs. control, n = 29 for control, n = 28 for UFP, n = 29 for ADAM10, n = 15 for DN-*Notch1b*), whereas *NICD* mRNA injection rescued endothelial Notch activity and restored vascular regeneration (**Fig. 4A**).

Endothelial Notch activity was further quantified by a customized MATLAB algorithm to color-code the accentuation of co-localized Notch activity in the vasculature **(Fig. 4B**). These findings further support that UFP exposure inhibits endothelial Notch activity to impair vascular network formation.

**UFP exposure attenuated FOXO1-mediated Notch activation complex**

To elucidate the mechanism underlying UFP-mediated reduction in Notch activity, we analyzed the protein levels of NICD and Notch co-activators to form the activation complex. The total, active, and nuclear NICD protein levels remained unchanged in HAEC following 6 hours of UFP exposure (**Fig. 5A**). Consistently, intact level of NICD protein was observed in response to various UFP exposure time (2, 3, 4, 5, and 6 hours) (* $P < 0.05$ vs. control, n = 3) (**Fig. S6**). In contrast, FOXO1 expression, but not Mastermind-like1 (MAML1) expression, was significantly reduced after 6 hours post initial UFP exposure (* $P < 0.05$ vs. control, n = 3) (**Fig. 5B**). *FOXO1* mRNA expression was also reduced in a dose- and time-dependent manner by UFP treatment (* $P < 0.05$ vs. control, n = 3) (**Fig. 5C**). Treatment of the proteasome inhibitor, MG-132, in the presence of UFP restored UFP attenuated- FOXO1 protein expression, suggesting that UFP also stimulate the degradation of FOXO1 via proteasome (**Fig. 5D**) (* $P < 0.05$ vs. control, n = 3). To determine whether suppressing FOXO1 expression affects the formation of the Notch activation complex, we performed immunoprecipitation and immunofluorescence against NICD and FOXO1, respectively. Immunoprecipitation with different UFP exposure time (2, 3, 4, 5, and 6 hours) revealed that UFP suppressed FOXO1 expression 4-5 hours post initial exposure, while significantly attenuated FOXO1-mediated NICD pull down 5 and 6 hours after exposure (**Fig. 5E**). Immunofluorescence further uncovered a reduction in NICD and FOXO1 co-localization (* $P < 0.05$, n = 3) (**Fig. 5F**). Silencing FOXO1 with

siRNA recapitulated the UFP-mediated reduction in Notch activation complex formation (* $P < 0.05$, n = 3) (**Fig. 5E**), and down-regulated Notch signaling gene expressions. These data corroborate FOXO1-mediated Notch signaling (**Fig. S7**), and UFP suppression of FOXO1 expression, leading to a reduction in FOXO1/Notch activation complex.

**FOXO1 is an essential co-activator for the Notch activation complex for vascular repair**

To assess the importance of FOXO1/Notch activation complex for vascular regeneration, we performed gain- and loss-of-function analyses on FOXO1. Wholemount zebrafish immunofluorescence staining with anti-FOXO1 validated the reduction of FOXO1 expression following FOXO1 MO micro-injection (**Fig S6A**). Embryos injected with P53 control MO developed normal vascular repair at 3 dpa (* $P < 0.05$, n = 20), whereas FOXO1 MO impaired vascular regeneration analogous to UFP-mediated effect (**Fig. 6A**). *FOXO1* mRNA rescue restored regeneration despite the presence of UFP (* $P < 0.05$, n = 25), whereas co-injection of FOXO1 MO with *NICD* mRNA failed to restore vascular regeneration (* $P < 0.05$, n = 17) (**Figs. 6A-C**). FOXO1 MO attenuated Notch activity in the *Tg(tp1:GFP, flk1:mCherry)* embryos (**Figs. 7, S7B**), co-injection of FOXO1 MO and *NICD* mRNA partially restored Notch activity (* $P < 0.05$, n = 15) (**Figs. 7A-B**). Taken together, FOXO1 is an essential co-activator of the Notch activation complex, and UFP inhibits FOXO1-mediated Notch signaling to impair vascular regeneration following tail amputation (**Fig. 8)**.

## Discussion

The novel contribution of our study lies in the elucidation of UFP-mediated disruption in FOXO1/Notch complex to impair vascular network formation. DN-*Notch 1b* mRNA

injection or ADAM10 inhibitor treatment supports Notch signaling as the mechanism underlying UFP-impaired vascular regeneration. We further uncovered that UFP attenuated FOXO1 expression and FOXO1/NICD co-localization. While *NICD* mRNA rescue partially restored Notch activity, *FOXO1* mRNA rescue completely restored UFP-attenuated Notch activity and blood flow to the injured site. Hence, FOXO1 is as an essential co-activator for the Notch activation complex for Notch signaling-mediated vascular regeneration.

The Notch signaling pathway regulates stem cell differentiation and proliferation [24, 29-32]. Ablation of Notch1 induces developmental retardation, followed by collapsed arterial/venous specification and vascular malformation [18]. Dysregulated Notch activity results in abnormal endothelial proliferation, leading to a hyperplastic vascular network prone to developing cancer [33]. Missense mutation in the Notch3 gene is the underlying cause of the degenerative vascular disease known as Cerebral Autosomal-Dominant Arteriopathy with Subcortical Infarcts and Leukoencephalopathy (CADASIL) [34]. In addition, Notch signaling is implicated in the initiation of sprouting angiogenesis [35, 36]. Following UFP exposure, zebrafish embryos developed impaired vascular repair and aberrant appearance in intersomatic space (**Figs. 1 & 3**), accompanied with reduced Notch activity and down-regulation of Notch target genes (**Fig. 2**). We further corroborated UFP-mediated reduction in Notch activity using the transgenic *Tg(tp1:GFP)* Notch activity reporter line (**Figs. 3 & 7**). In addition, ADAM10 inhibitor or DN-*Notch1b* mRNA strengthened the role of Notch signaling in restoring vascular network formation. As a corollary, UFP attenuated vascular endothelial cell migration and tube formation (**Fig. S2**). Thus, UFP attenuates Notch signaling to impair vascular regeneration.

NICD, MAML1, and FOXO1 bind to the CSL domain to form a Notch activation complex. While UFP inhibited Notch activity, NICD and MAML protein levels remained unchanged. For this reason, we uncovered down-regulation of FOXO1 mRNA and protein expression following UFP exposure (**Fig. 5**). FOXO1 and Notch cooperation has been reported in myogenic differentiation and neural stem cell differentiation [27, 37]. Our data suggest that UFP exposure suppressed FOXO1-mediated Notch activation complex formation; thus, attenuating Notch signaling for vascular regeneration.

Exposure to ambient $PM_{2.5}$ promotes cardiovascular, pulmonary, and gastrointestinal disorders [38]. Epidemiological studies associated maternal exposure to air pollutants with increased occurrence of congenital heart diseases [7]. Maternal exposure to ozone ($O_3$) at the second-month gestation increases the risk of aortic and pulmonary valve anomalies [6]. UFP are the redox-active sub-fraction of $PM_{2.5}$, harboring elemental carbon and polycyclic aromatic hydrocarbons (PAH) as products of incomplete combustion from urban environmental sources, including the exhaust from diesel trucks and gasoline vehicles [39]. Their large surface-to-volume ratio favors their potential adsorption to or absorption in the pulmonary and cardiovascular systems [40-42]. Long-term epidemiological studies on UFP exposure demonstrate adverse respiratory function [43,44], exercise-induced cardiac ischemia [45] and arrhythmias [46]. At the molecular level, UFP induces JNK-mediated superoxide ($O_2^{\cdot -}$) production and NF-κB-mediated monocyte recruitment to prime atherosclerosis [13, 47]. UFP exposure via inhalation increases plasma lipid metabolites and reduces HDL anti-oxidant capacity to accelerate atherosclerosis in LDLR-null mice [14]. UFP inhalation further promotes atherogenic lipid metabolites and macrophage infiltrates in the intestine [39], where microbiota composition was altered to produce atherogenic lipid metabolites [48]. In our zebrafish model of vascular injury and

repair, we provide the first molecular insights into UFP-suppressed FOXO1 as a co-activator for the Notch activation complex.

The emerging role of redox-sensitive micro-RNAs (miRNAs), including miR-223 and -375, have been implicated in disrupting FOXO1 signaling [49] and cellular proliferation [50, 51]. Furthermore, miR-154 and -379 have been reported to regulate inflammatory responses [52, 53]. While miR-3188 targets the mTOR pathway to suppress p-PI3K/p-AKT/c-JUN signaling [54], miR-132 activates the PI3K/AKT pathway to decrease FOXO1 expression [55]. $PM_{2.5}$ has been reported to modulate the levels of a number of miRNAs including miR-223 and miR-375 [56-58]. Thus, UFP could down-regulate FOXO1 by modulating miRNAs. Additionally, we have previously reported that UFP activates JNK, and JNK activation promotes protein ubiquitination and degradation via proteasome activity [13, 59]. In this study, we observed UFP down-regulated FOXO1 protein levels via proteasome degradation (**Fig. 5D**) which could be mediated by the JNK pathway (**Fig. S9**). However, the precise mechanism whereby UFP exposure suppresses FOXO1 expression warrants further investigation [60].

Overall, we demonstrate FOXO1 as an important co-activator with NICD for assembling the Notch activation complex for vascular development and regeneration [61]. UFP-mediated reduction in FOXO1/NICD complex formation was corroborated by immunoprecipitation of FOXO1-mediated NICD pull down, immunofluorescence of FOXO1 expression, and FOXO1/NICD co-localization. Thus, exposure to redox active UFP disrupts Notch activity to impair vascular network formation.

**Acknowledgements**

We are grateful to Dr. Weinmaster for providing the NICD plasmid and the JH26 Notch reporter plasmid, and we thank Drs. David Traver at UCSD and Nathan Lawson at the University of Massachusetts Medical School (Worcester, Massachusetts, USA) for generously providing the *Tg(tp1:GFP)* line. This study was supported by National Institutes of Health R01HL083015 (TKH), R01HL111437 (TKH), R01HL129727 (TKH), R01HL118650 (TKH), American Heart Association 16SDG30910007 (RRSP), and funded by EPA under STAR program (CS) and the South Coast Air Quality Management District Award (CS). Chapter III is a reprint of the article: Baek KI, Packard RRS, Hsu JJ, Saffari A, Ma Z, Luu AP, Pietersen A, Yen H, Ren B, Ding Y, Sioutas C, LiR, Hsiai TK. Ultrafine particle exposure reveals importance of FOXO1/Notch activation complex for vascular regeneration. Antioxid Redox Signal. 28(13), 2018, (https://doi.org/10.1089/ars.2017.7166). Reprint was reproduced with permission from the publisher and all of the co-authors of the publication.

## FIGURES

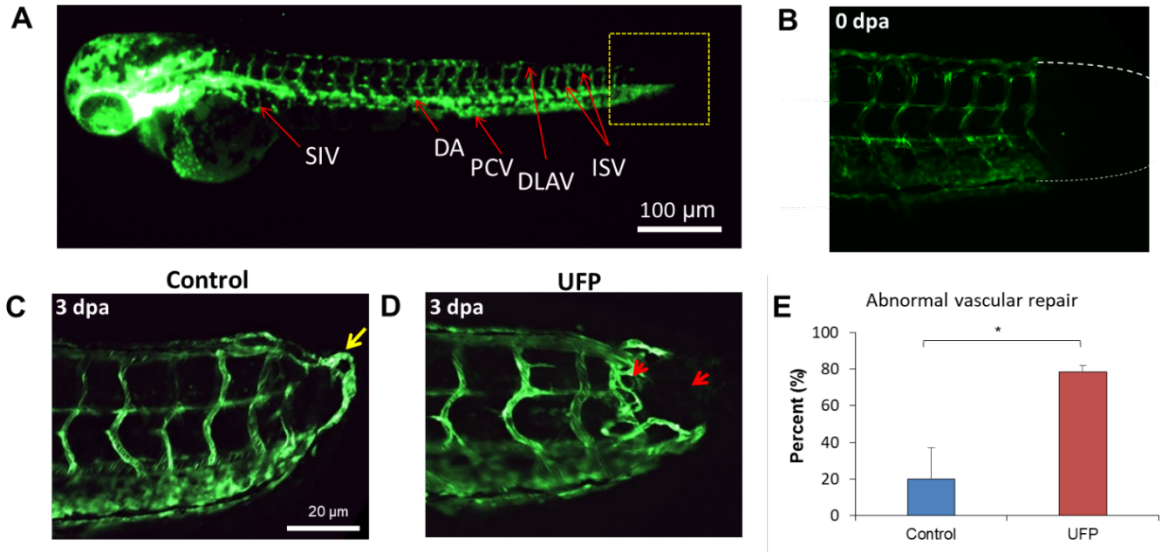


**Figure 1.** UFP impaired vascular repair. **(A)** Vasculature of transgenic *Tg(fli1:GFP)* zebrafish at 3 days post fertilization (dpf). The yellow dashed box denotes the site of tail amputation. **(B)** Zebrafish underwent tail amputation at 3 dpf. Dashed line indicates the site of amputation. **(C)** WT fish developed vascular regeneration with a complete loop connecting the Dorsal Aorta (DA) with the Dorsal Longitudinal Anastomotic Vessel (DLAV) at 3 days post amputation (dpa) (yellow arrow). **(D)** Fish exposed to UFP at 25 µg/mL developed impaired vascular repair and a disrupted vascular network (red arrows) at 3 dpa. **(E)** Percentage of fish with abnormal vascular repair. UFP exposure led to significant impairment in vascular repair (* $P < 0.05$, n=20 for WT, n=28 for UFP). Reproduced in this dissertation with permission from Baek *et al*.

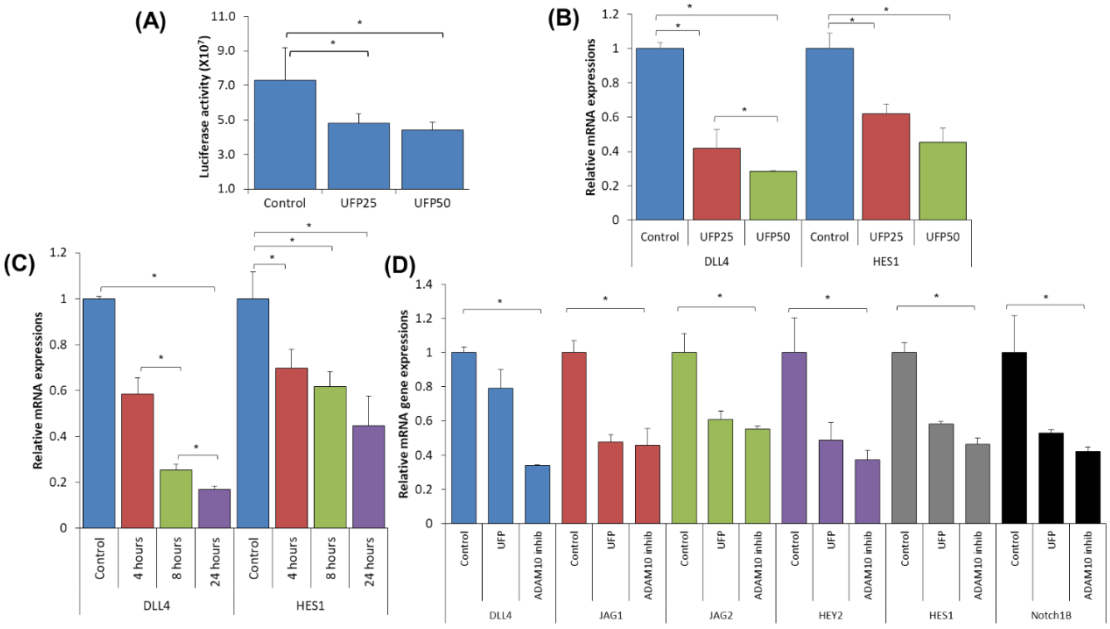


**Figure 2.** UFP inhibited Notch signaling. **(A)** Human aortic endothelial cells (HAEC) transfected with Notch reporter plasmid pJH26 were treated with UFP at 25 µg/mL (UFP25) or 50 µg/mL (UFP50) for 12 hours, resulting in a dose-dependent reduction in Luciferase activity (* $P < 0.05$ vs. control, n=3). **(B)** Dose response of UFP on the mRNA expression of Notch ligand Dll4 and Notch target HES1 in HAEC. **(C)** Time course of UFP on the mRNA expression of Dll4 and HES1. UFP inhibited the expression of Dll4 and HES1 in a dose-, and time course- dependent manner. **(D)** Notch signaling-related mRNA expression in zebrafish larvae, including Notch ligands, *DLL4* (*blue*), *JAG1* (*red*) and *JAG2* (*green*), Notch receptor, *Notch1b* (*black*), and Notch target gene *Hey2* (*purple*), were significantly down-regulated in response to UFP (25 µg/mL) or ADAM10 inhibitor (GI254023X at 5µM) at 3 days post amputation(* $P < 0.05$ vs. control, n=3). Reproduced in this dissertation with permission from Baek *et al*.

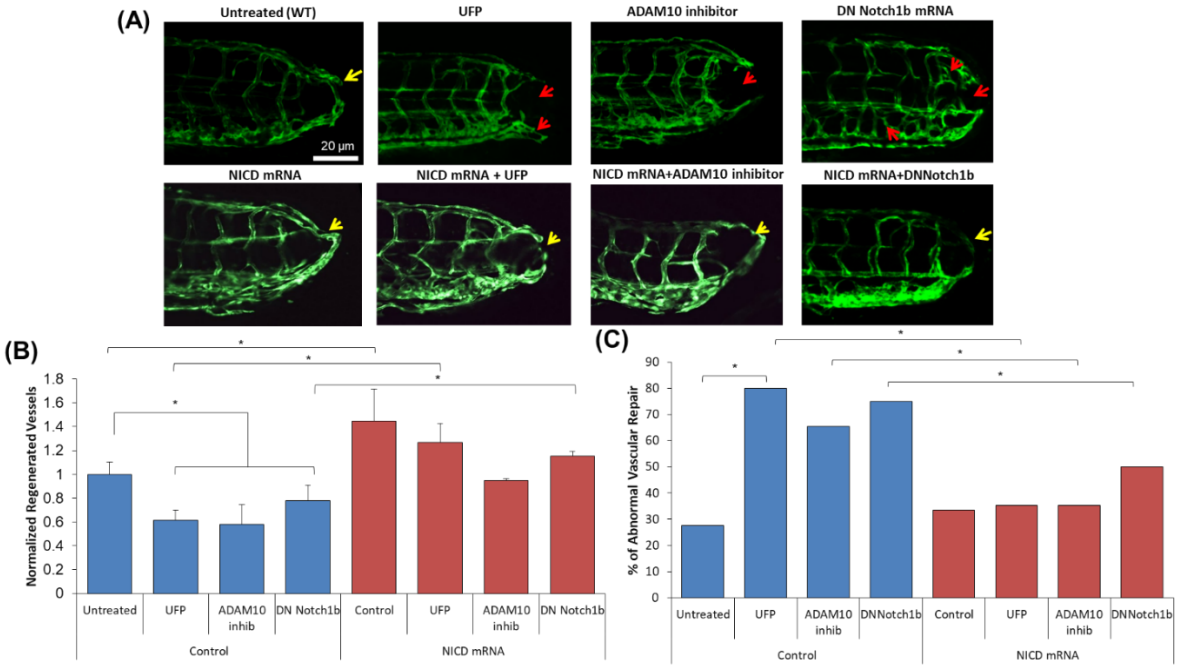


**Figure 3.** UFP impaired vascular repair via Notch signaling. (A) Control (WT) *Tg(fli1:GFP)* zebrafish embryos developed vascular regeneration at 3 days post tail amputation (dpa). UFP or ADAM 10 inhibitor treatment impaired vascular regeneration. Injection with Dominant negative (DN) *DN-Notch1b* mRNA mitigated intersegmental vessel (ISV) network and impaired tail regeneration, similar to the UFP mediated effect (* $P < 0.05$, n = 20). NICD mRNA injection rescued UFP-impaired vascular regeneration by UFP, ADAM10 inhibitor, or injection of DN-Notch1b mRNA. (B) Quantification of the area of regenerated vessels as described in methods. (* $P < 0.05$ vs. control, n=5). (C) Proportion of fish with abnormal vascular regeneration. Reproduced in this dissertation with permission from Baek *et al*.

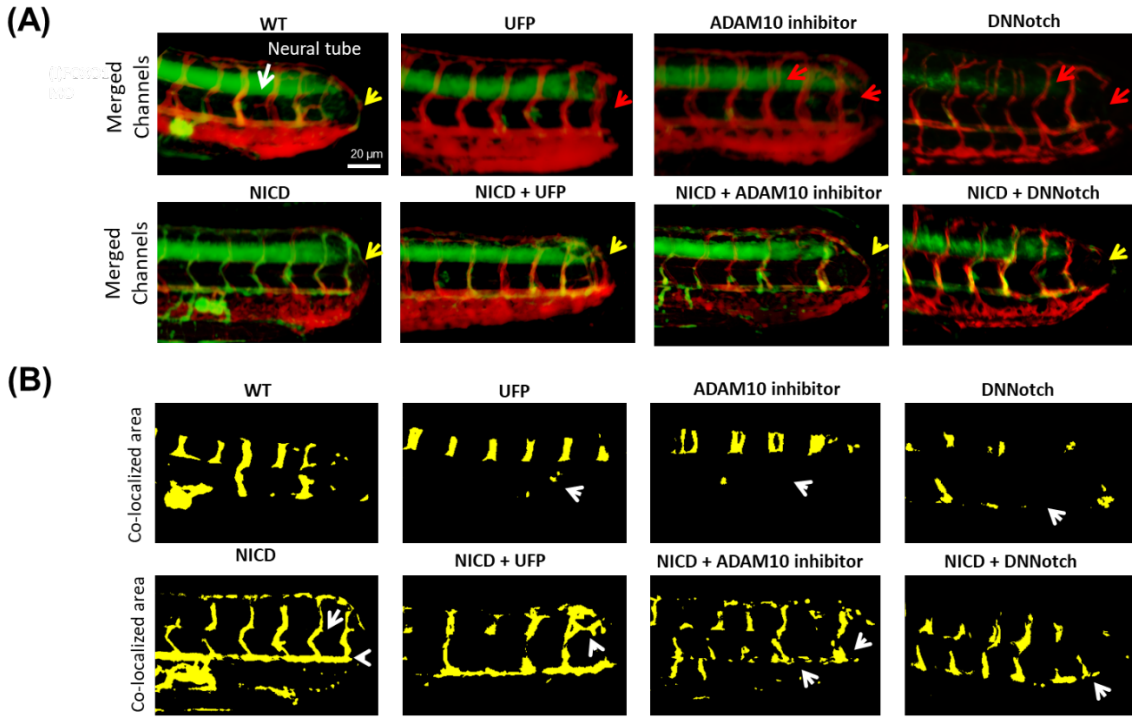


**Figure 4:** UFP inhibited Notch activity at the site of vascular injury. **(A)** Transgenic *Tg(tp1:GFP; flk1:mCherry)* embryos revealed Notch activity in vasculature, indicated by the overlapped yellow color, corroborating the role of endothelial notch activity in site of vascular repair. **(B)** Endothelial Notch activity was accentuated by customized MATLAB algorithm. In the presence of UFP, endothelial Notch activity was nearly absent, while NICD mRNA rescued Notch inhibition by UFP, ADAM10 inhibitor, or DN-Notch1b mRNA in vasculature. Reproduced in this dissertation with permission from Baek *et al*.

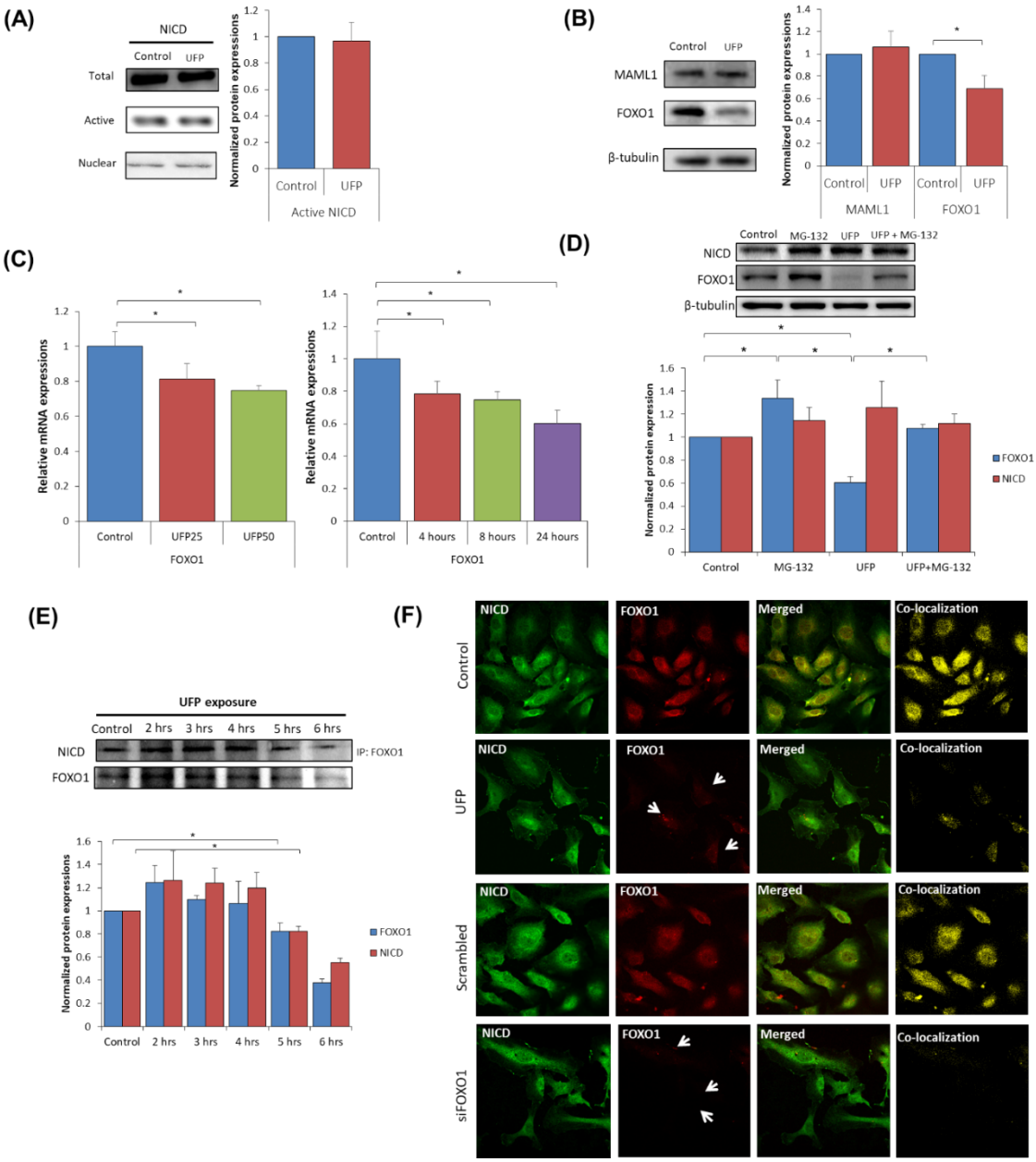


**Figure 5**. UFP exposure attenuated FOXO1-mediated Notch activation complex. **(A)** Total, active and nuclear NICD protein expression remained unchanged following UFP exposure at 25 μg/mL for 6 hours in HAEC. **(B)** Protein expressions of the NICD co-activator Master-mind like 1(MAML1) was unchanged, whereas FOXO1 was significantly reduced following UFP exposure (* $P < 0.05$ vs. control, n=3). **(C)** UFP down-regulated FOXO1 mRNA expression in a dose- and time-dependent manner ($P < 0.05$ vs. control, n=3). **(D)** HAEC were cultured in the presence or

absence of UFP with or without 10 μM of proteasome inhibitor MG-132 for 6 hours. FOXO1 and NICD protein expression were elevated by 1.34-fold and 1.14-fold respectively when treated with MG-132 alone. UFP induced a decrease in FOXO1 protein expression, while MG-132 restored UFP attenuated-FOXO1 expression (* $P < 0.05$ vs. control, normalized to β-tubulin expression, n=3). **(E)** Immunoprecipitation with different UFP exposure times (2, 3, 4, 5, and 6 hours) revealed significant reduction of FOXO1 and NICD pull down against anti-FOXO1 antibody at 5 and 6 hours post UFP exposure, while the initial reduction started between 4-5 hours of exposure (* $P < 0.05$ vs. control, n=3). **(F)** Immunofluorescence staining of NICD and FOXO1 in HAEC treated with or without UFP. UFP significantly reduced FOXO1 levels, whereas NICD levels remained unchanged. Co-localization with MATLAB code revealed that UFP reduced FOXO1-mediated Notch activation complex formation. Reproduced in this dissertation with permission from Baek *et al*.

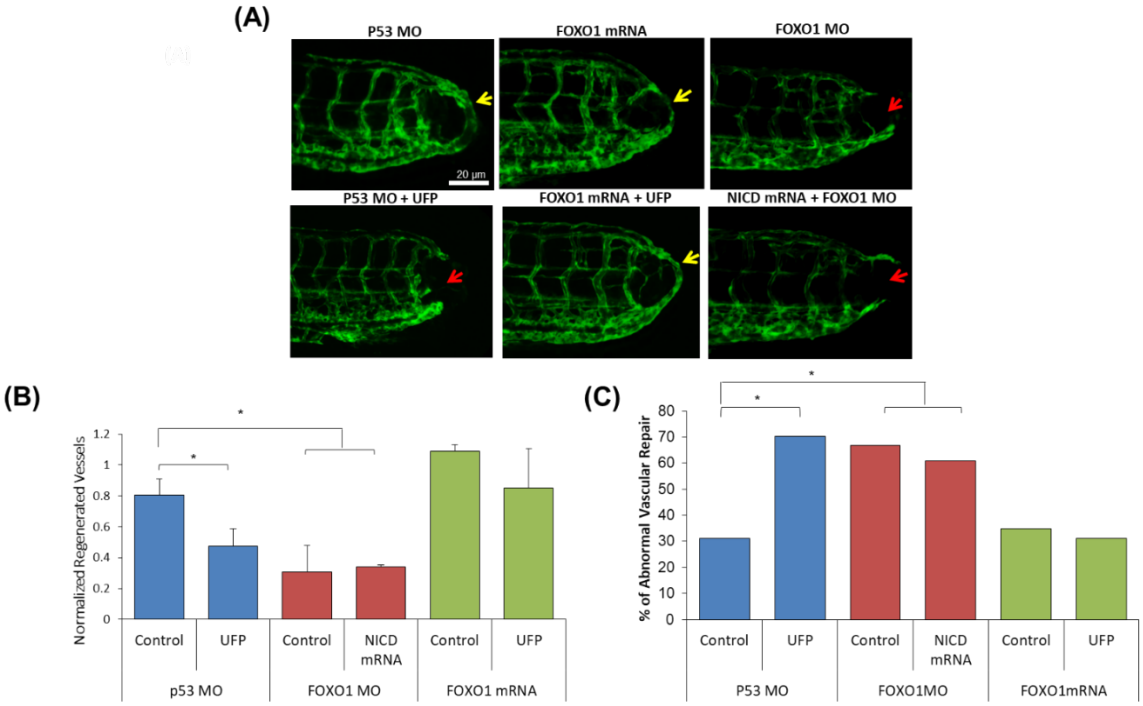


**Figure 6.** UFP impairs vascular regeneration via FOXO1. **(A)** Transgenic *Tg (fli1:GFP)* zebrafish injected with P53 control MO developed complete vascular regeneration between the DA and DLAV, but impaired vascular regeneration in response to UFP treatment or FOXO1 MO injection. FOXO1 mRNA restored vascular regeneration in the presence of UFP. NICD mRNA failed to restore regeneration following FOXO1 MO injection. **(B)** The area of regenerated vessels were quantified as described in methods (* $P < 0.05$ vs control, n=5). **(C)** Proportion of fishes with abnormal vascular regeneration was quantified (* $P < 0.05$ vs. control, n=5). Reproduced in this dissertation with permission from Baek *et al*.

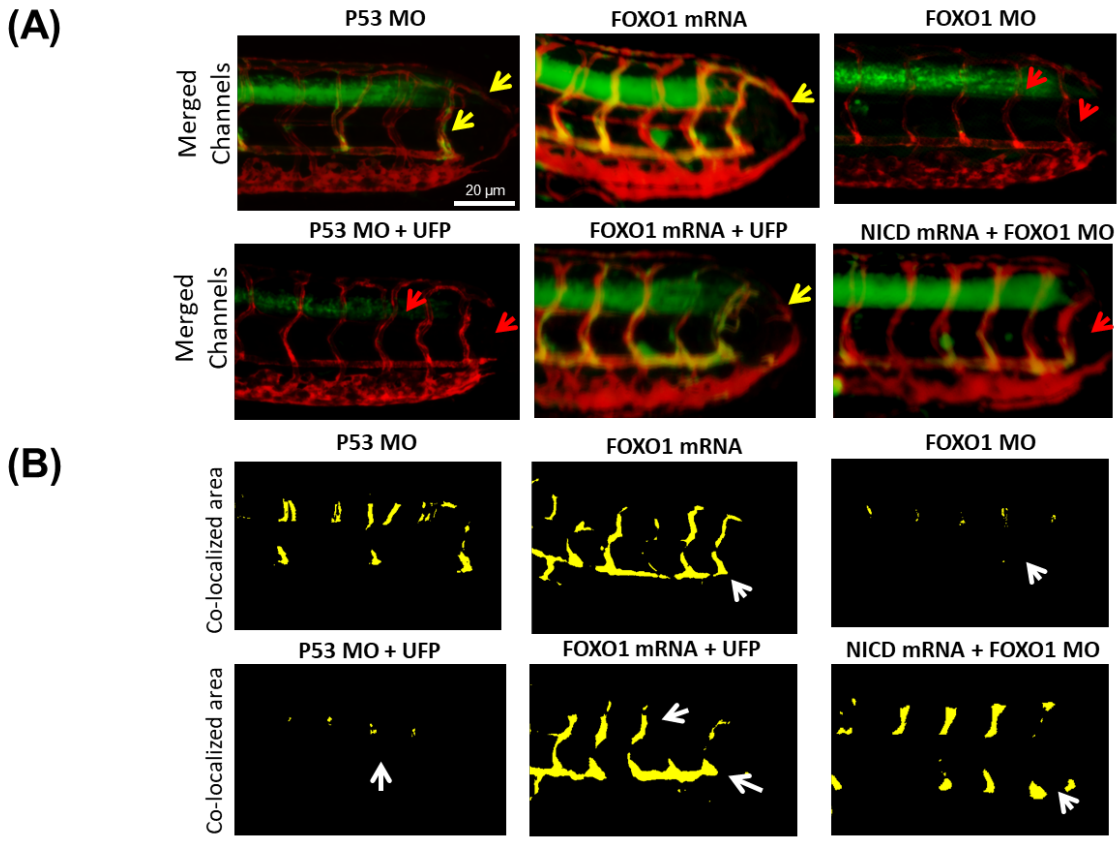


**Figure 7.** FOXO1 modulated endothelial Notch activity at the site of vascular injury. **(A)** In the transgenic *Tg(tp1:GFP; flk1:mCherry)* embryos, FOXO1 MO attenuated Notch activity and impair vascular regeneration. Rescue with FOXO1 mRNA promoted endothelial Notch activity and rescued UFP impaired vascular regeneration (* $P < 0.05$ vs. control, n=26). Co-injection of NICD mRNA with FOXO1 MO partially restored Notch activity but failed to restore vascular regeneration. **(B)** Endothelial Notch activity was accentuated by the customized MATLAB code. Endothelial Notch activity were attenuated (white arrows) in response to UFP exposure or to FOXO1 MO, while rescue with FOXO1 mRNA promoted endothelial Notch activity. Reproduced in this dissertation with permission from Baek *et al*.

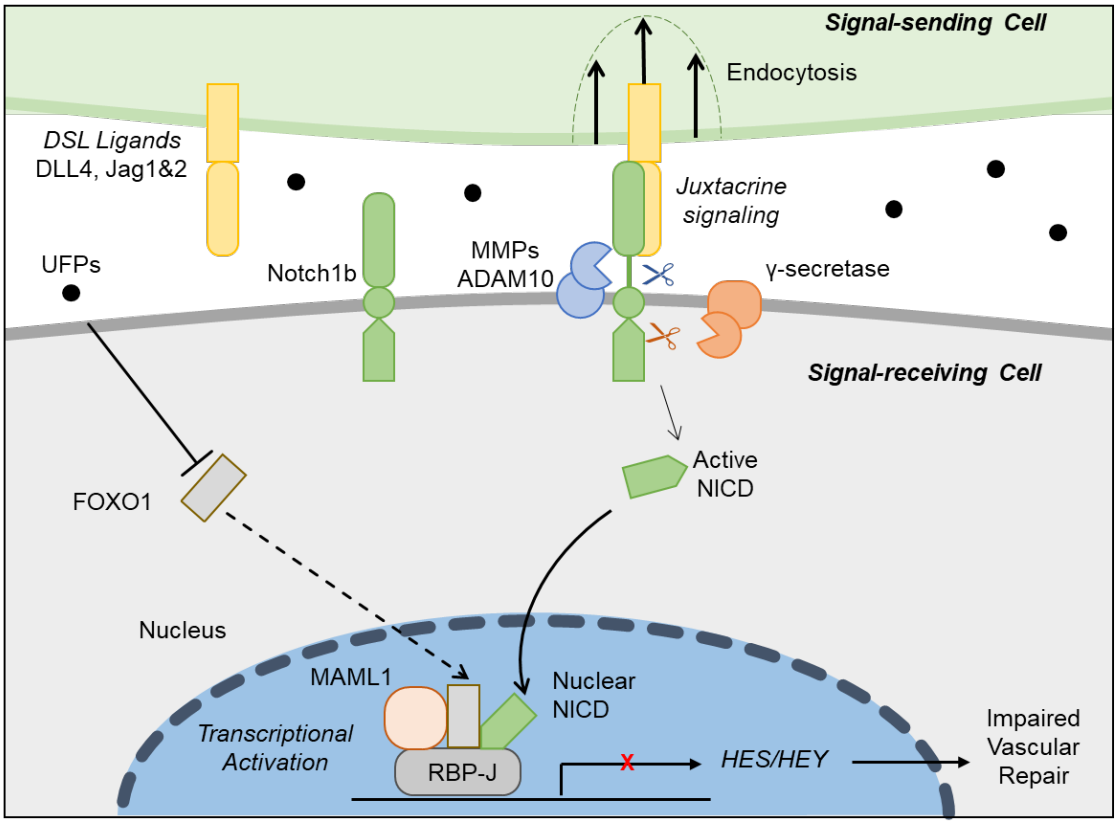


**Figure 8.** A schematic diagram. A depiction of the disruption of FOXO1/Notch cooperation highlights impaired vascular network formation. Reproduced in this dissertation with permission from Baek *et al*.

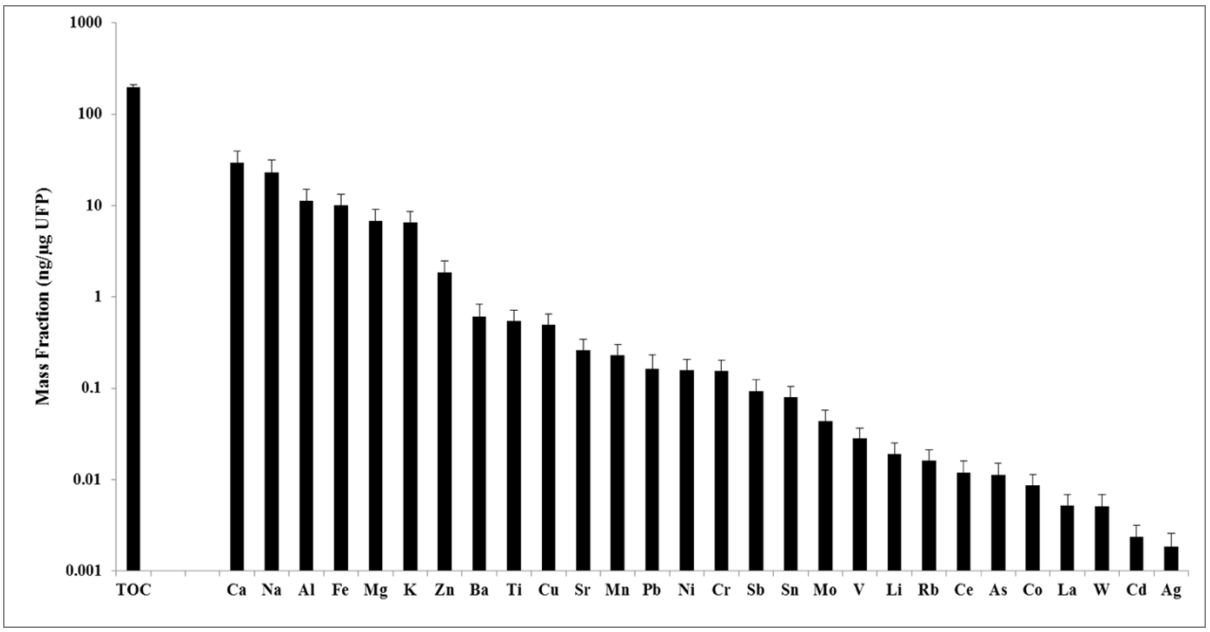


**Figure S1**. Chemical composition of UFP. Mass fraction of total organic carbon (TOC) as well as major metals in UFP were measured as described in the online supplemental methods. Error bars represent standard deviations. Reproduced in this dissertation with permission from Baek *et al*.

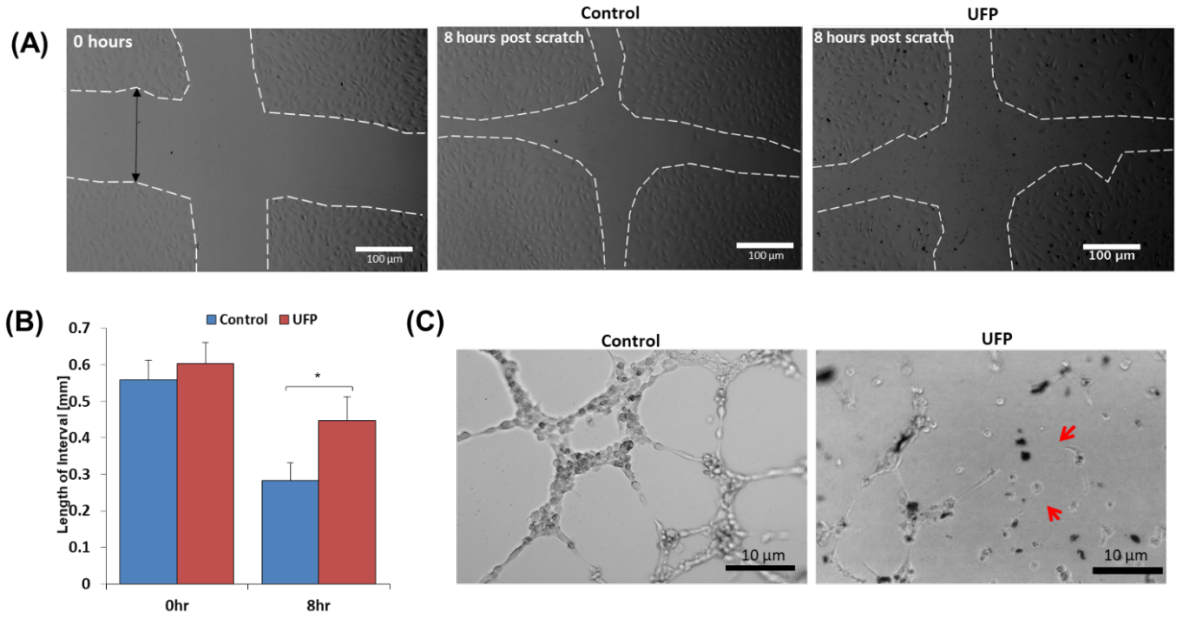


**Figure S2.** UFP inhibits cell migration and tube formation. **(A)** HAEC were pre-treated with and without UFP at 25 µg/mL and tube formation was assessed in Matrigel. UFP inhibited HAEC migration at 8 hours. **(B)** Quantification of cell migration was measured by average residual distances (black arrow) between inner borders of the scratched area not covered by cells. **(C)** HAEC were pre-treated and incubated with or without UFP at 25 µg/mL and tube formation was assessed. HAEC exposed to UFP at 25 µg/mL led to attenuated tube formation at 8 hours post treatment (red arrows) compared to the tube formation of untreated HAEC. Reproduced in this dissertation with permission from Baek *et al*.

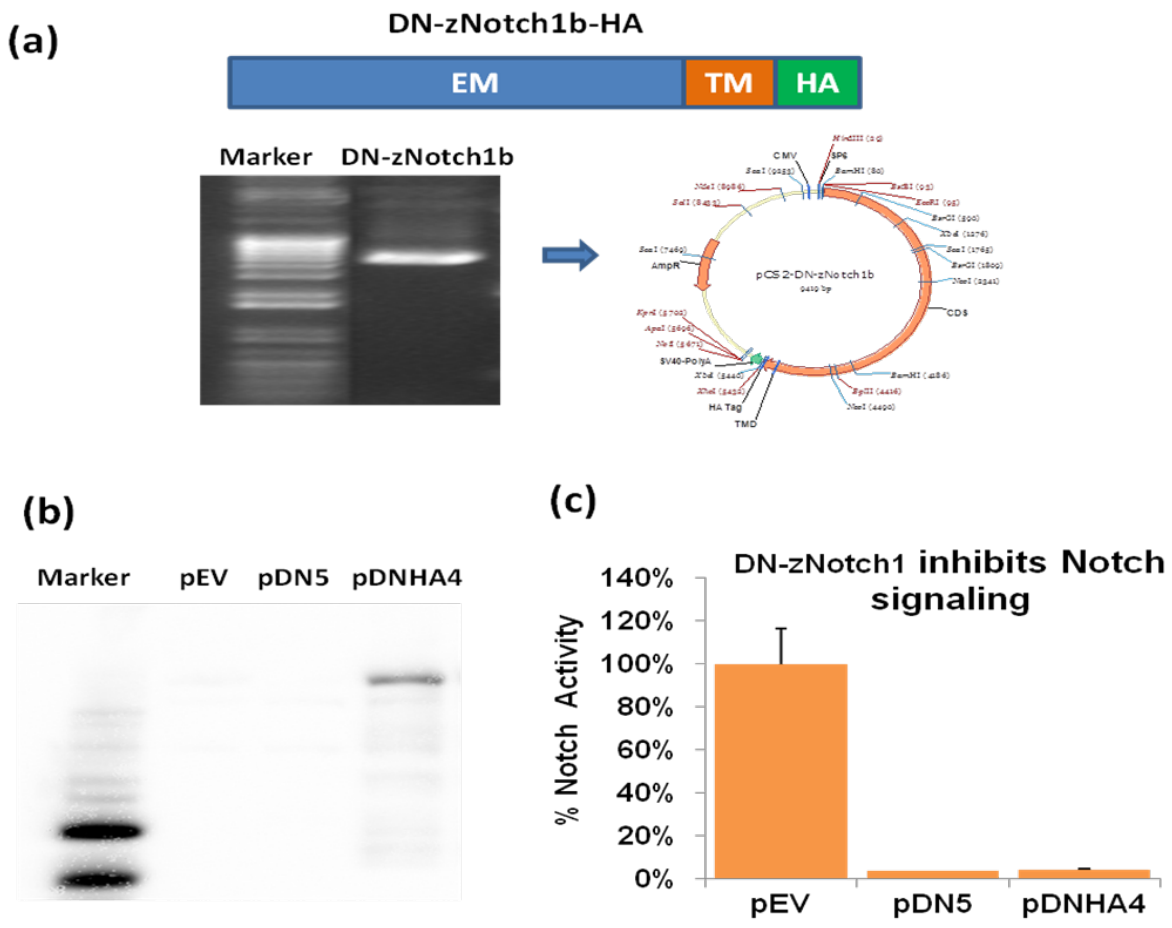


**Figure S3.** Construction of dominant-negative Notch1b (DN-Notch1b) zebrafish **(A)** Zebrafish Notch1b cDNA with the intracellular domain truncated (DN-zNotch1b) and a HA-tag was amplified from isolated zebrafish mRNA into the pCS2 plasmid. **(B)** HEK293 cells were transfected with pCS2 empty plasmid (pEV), pCS2-DN-Notch1b (pDN5) or pCS2-DN-Notch1b-HA(pDNHA4). Western blot with anti-HA tag antibody showed the expression of DN-zNotch1b with HA tag. **(C)** HEK293 cells were transfected with a Notch signaling reporter (pJH26) plus pEV, pDN5, or pDNHA4. Luciferase activity demonstrated that the DN-zNotch1b with or without HA tag inhibited Notch signaling. Reproduced in this dissertation with permission from Baek *et al*.

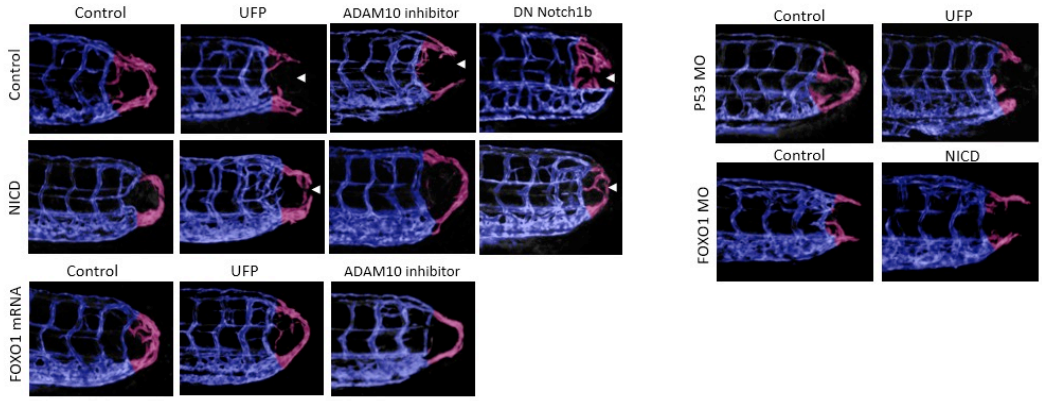


**Figure S4.** Quantification of the regenerated vessel. The area highlighted as pink indicates regenerated vessel, which was quantified using Amira 3D software. Reproduced in this dissertation with permission from Baek *et al*.

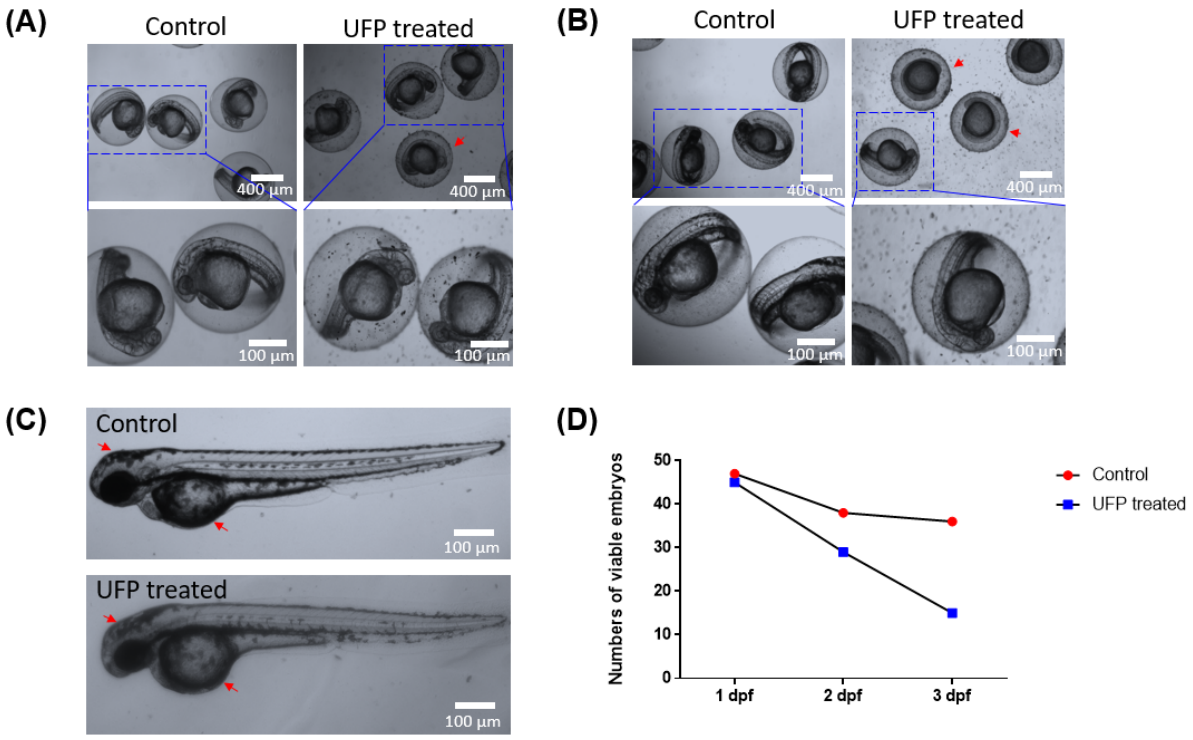


**Figure S5.** UFP Exposure retarded embryogenesis and promoted embryonic lethality. *Tg(Fli1-GFP)* zebrafish embryos at 1-2 cell stage were treated with or without UFP at 25 µg/ml for 3 days. **(A)** At 1 dpf, ~97% of embryos remained intact in both control and UFP treated groups. **(B)** At 2 dpf, 20% in the control group, and 34% UFP treated-embryos developed embryonic lethality, along with retarded development (red arrows). **(C)** Following 3 days of UFP exposure, 94% of viable embryos in the control group underwent complete embryogenesis. Only 51% remained viable following UFP exposure (n=47 for the control group, n=45 for UFP treated group), and these UFP-exposed embryos developed immature tectum and yolk sac formation. Reproduced in this dissertation with permission from Baek *et al*.

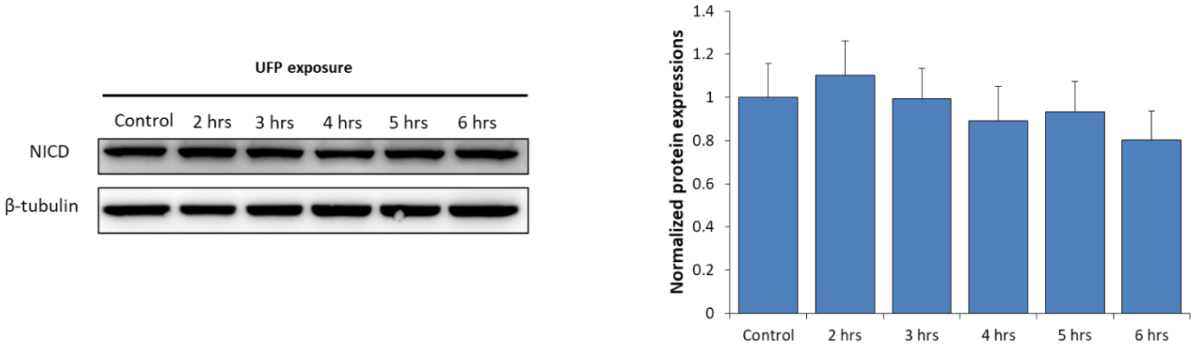


**Figure S6**. NICD protein level in HAEC remained unchanged in response to UFP exposure. Time course of NICD protein expression after UFP exposure for different time. NICD protein expression in HAEC remained unchanged in response to UFP exposure (relative levels were normalized to b-tubulin expression, n = 3). NICD, notch intracellular cytoplasmic domain. Reproduced in this dissertation with permission from Baek *et al*.

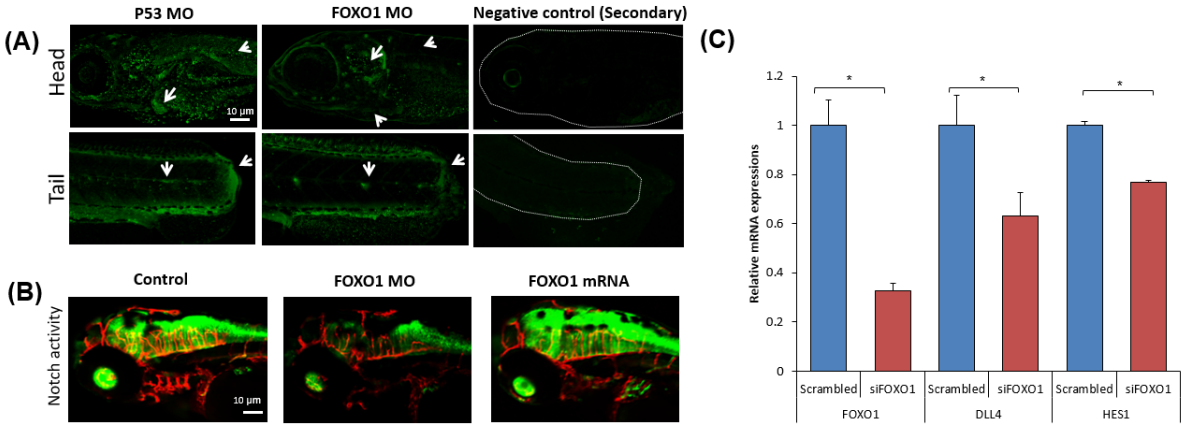


**Figure S7.** FOXO1 knockdown inhibited Notch signaling. **(A)** Micro-injection of FOXO1 MO suppressed FOXO1 expression in viable wild type ABWT zebrafish (white arrows) at 3 dpf as visualized by wholemount immunofluorescence staining. **(B)** Notch activity in central nervous system (CNS) was visualized in transgenic *Tg(tp1:GFP; flk1:mCherry)* zebrafish. Micro-injection of FOXO1 MO mitigated, whereas FOXO1 mRNA promoted, Notch activity in the neuronal network at 6 dpf. **(C)** Silencing FOXO1 expression with siRNA attenuated the expression of Notch signaling related genes *Dll4* and *Hes1* in HAEC. Reproduced in this dissertation with permission from Baek *et al*.

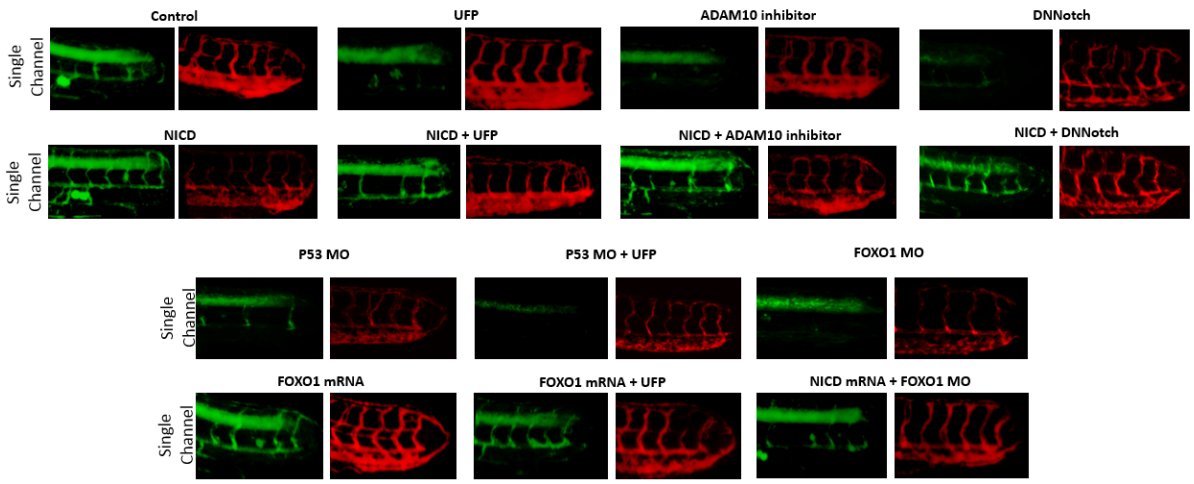


**Figure S8.** Imaging of endothelial Notch activity with *Tg(tp1:GFP; flk1:mCherry)* zebrafish. Images of Notch activity (green) and vasculature (red) in zebrafish with indicated treatments. Reproduced in this dissertation with permission from Baek *et al*.

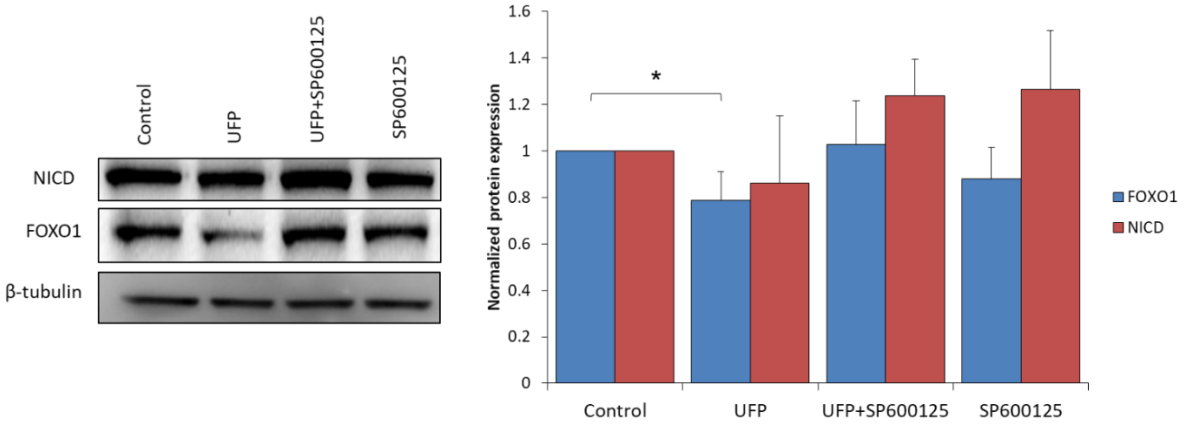


**Figure S9.** Inhibition of JNK signaling rescues UFP-inhibited FOXO1 expression. JNK inhibitor, SP600125, restored UFP-attenuated FOXO1 protein expression (*$p < 0.05$ vs. control, n = 3). Reproduced in this dissertation with permission from Baek *et al*.

**[Supplemental Videos Available Online]**

**Video S1**. UFP impairs vascular regeneration. **(A)** Control zebrafish exhibited functional vascular recovery at 3 dpa, allowing erythrocytes to flow through the vasculature (yellow arrow, n = 5). **(B)** UFP exposure impaired vascular regeneration accompanied by abnormal circulation at the DLAV, and between the DA and PCV (red arrows, n = 5). DA, dorsal aorta; DLAV, dorsal longitudinal anastomotic vessel; dpa, days post-amputation; UFP, ultrafine particles; PCV, posterior cardinal vein.

**Table 1. Sequencing Information of qRT-PCR primers and Morpholino**

| | | |
|---|---|---|
| Human Hey1 | Forward | GTTCGGCTCTAGGTTCCATGT |
| | Backward | CGTCGGCGCTTCTCAATTATTC |
| Human Dll4 | Forward | CGACAGGTGCAGGTGTAGC |
| | Backward | TACTTGTGATGAGGGCTGGG |
| Human FOXO1 | Forward | GCGACCTGTCCTACGCCGACCTCA |
| | Backward | CCTTGAAGTAGGGCACGCTCTTGACC |
| Zebrafish Jag1 | Forward | CCGCGTATGTTTGAAGGAGTATCAGTCG |
| | Backward | CAGCACGATCCGGGTTTTGTCG |
| Zebrafish Jag2 | Forward | AGCCCTAGCAAAACGAGCGACG |
| | Backward | GCGTGAATGTGCCGTTCGATCAA |
| Zebrafish Dll4 | Forward | CAAAGTGGGAAGCAGACAGAGCTAAGG |
| | Backward | CGGTCATCCCTGGGTGTGCATT |
| Zebrafish Notch1b | Forward | CAGAGAGTGGAGGCACAGTGCAATCC |
| | Backward | GCCGTCCCATTCACACTCTGCATT |
| Zebrafish Hey2 | Forward | AAGATGTGGCTCACCTACAAC |
| | Backward | TGGCACCAGACGACGCAACTC |
| Zebrafish FOXO1 | Forward | TTGTTCTTTTTGCAGGATCCACCATGGCCG AGGCGCCCCAGGTG |
| | Backward | TCACTATAGTTCTAGATTAGCCTGACACCC AGCTGTGTGTTGTAG |
| Zebrafish NICD | Forward | GCAGGATCCACCATGGGTTGTGGGGTGCT GCTGTCCCGCAAG |
| | Backward | CTTGAATTCTTACTTAAATGCCTCTGGAAT GTGGGTG |
| Zebrafish DN-Notch1b | Forward | GATCCCATCGATTCGAATTCACCATGCATC TTTTCTTCGTGAAACTAATTGTTG |
| | Backward | CTATAGTTCTAGAGGCTCGAGCTAAGCGTA ATCTGGAACATCGTATGGGTATTCTCCGAC CGGCTCTCTCCTC |
| Zebrafish P53 MO | GCGCCATTGCTTTGCAAGAATTG | |
| Zebrafish FOXO1 MO | CTTTGAGGGCCATTACCTTCCAGCC | |

## References


1. Karimi Galougahi K, Ashley EA, Ali ZA. Redox regulation of vascular remodeling. *Cell Mol Life Sci*. 2016;73:349-363

2. Minicucci MF, Azevedo PS, Paiva SA, Zornoff LA. Cardiovascular remodeling induced by passive smoking. *Inflamm Allergy Drug Targets*. 2009;8:334-339

3. Brook RD, Rajagopalan S, Pope CA, 3rd, Brook JR, Bhatnagar A, Diez-Roux AV, Holguin F, Hong Y, Luepker RV, Mittleman MA, Peters A, Siscovick D, Smith SC, Jr., Whitsel L, Kaufman JD, American Heart Association Council on E, Prevention CotKiCD, Council on Nutrition PA, Metabolism. Particulate matter air pollution and cardiovascular disease: An update to the scientific statement from the american heart association. *Circulation*. 2010;121:2331-2378

4. Brunekreef B, Holgate ST. Air pollution and health. *Lancet*. 2002;360:1233-1242

5. Gorham ED, Garland CF, Garland FC. Acid haze air pollution and breast and colon cancer mortality in 20 canadian cities. *Can J Public Health*. 1989;80:96-100

6. Ritz B, Yu F, Fruin S, Chapa G, Shaw GM, Harris JA. Ambient air pollution and risk of birth defects in southern california. *American journal of epidemiology*. 2002;155:17-25

7. Dadvand P, Rankin J, Rushton S, Pless-Mulloli T. Ambient air pollution and congenital heart disease: A register-based study. *Environmental research*. 2011;111:435-441

8. Hwang BF, Lee YL, Jaakkola JJ. Air pollution and the risk of cardiac defects: A population-based case-control study. *Medicine*. 2015;94:e1883

9. Sardar SB, Fine PM, Mayo PR, Sioutas C. Size-fractionated measurements of ambient ultrafine particle chemical composition in los angeles using the nanomoudi. *Environ Sci Technol*. 2005;39:932-944

10. Lough GC, Schauer JJ, Park JS, Shafer MM, Deminter JT, Weinstein JP. Emissions of metals associated with motor vehicle roadways. *Environ Sci Technol*. 2005;39:826-836

11. Nel A, Xia T, Madler L, Li N. Toxic potential of materials at the nanolevel. *Science*. 2006;311:622-627

12. Zhang Y, Schauer JJ, Shafer MM, Hannigan MP, Dutton SJ. Source apportionment of in vitro reactive oxygen species bioassay activity from atmospheric particulate matter. *Environ Sci Technol*. 2008;42:7502-7509

13. Li R, Ning Z, Cui J, Khalsa B, Ai L, Takabe W, Beebe T, Majumdar R, Sioutas C, Hsiai T. Ultrafine particles from diesel engines induce vascular oxidative stress via jnk activation. *Free Radic Biol Med*. 2009;46:775-782

14. Li R, Navab M, Pakbin P, Ning Z, Navab K, Hough G, Morgan TE, Finch CE, Araujo JA, Fogelman AM, Sioutas C, Hsiai T. Ambient ultrafine particles alter lipid metabolism and hdl anti-oxidant capacity in ldlr-null mice. *J Lipid Res*. 2013;54:1608-1615

15. Araujo JA, Barajas B, Kleinman M, Wang X, Bennett BJ, Gong KW, Navab M, Harkema J, Sioutas C, Lusis AJ, Nel AE. Ambient particulate pollutants in the ultrafine range promote early atherosclerosis and systemic oxidative stress. *Circ Res*. 2008;102:589-596

16. Brook RD, Rajagopalan S. Particulate matter air pollution and atherosclerosis. *Current atherosclerosis reports*. 2010;12:291-300

17. Pope CA, 3rd, Burnett RT, Thurston GD, Thun MJ, Calle EE, Krewski D, Godleski JJ. Cardiovascular mortality and long-term exposure to particulate air pollution: Epidemiological evidence of general pathophysiological pathways of disease. *Circulation*. 2004;109:71-77

18. Krebs LT, Xue Y, Norton CR, Shutter JR, Maguire M, Sundberg JP, Gallahan D, Closson V, Kitajewski J, Callahan R, Smith GH, Stark KL, Gridley T. Notch signaling is essential for vascular morphogenesis in mice. *Genes & development*. 2000;14:1343-1352

19. Baonza A, Garcia-Bellido A. Notch signaling directly controls cell proliferation in the drosophila wing disc. *Proceedings of the National Academy of Sciences of the United States of America*. 2000;97:2609-2614

20. Jensen J, Heller RS, Funder-Nielsen T, Pedersen EE, Lindsell C, Weinmaster G, Madsen OD, Serup P. Independent development of pancreatic alpha- and beta-cells from neurogenin3-expressing precursors: A role for the notch pathway in repression of premature differentiation. *Diabetes*. 2000;49:163-176

21. Fre S, Huyghe M, Mourikis P, Robine S, Louvard D, Artavanis-Tsakonas S. Notch signals control the fate of immature progenitor cells in the intestine. *Nature*. 2005;435:964-968

22. Stanger BZ, Datar R, Murtaugh LC, Melton DA. Direct regulation of intestinal fate by notch. *Proceedings of the National Academy of Sciences of the United States of America*. 2005;102:12443-12448

23. Pellegrinet L, Rodilla V, Liu Z, Chen S, Koch U, Espinosa L, Kaestner KH, Kopan R, Lewis J, Radtke F. Dll1- and dll4-mediated notch signaling are required for homeostasis of intestinal stem cells. *Gastroenterology*. 2011;140:1230-1240 e1231-1237

24. Bray SJ. Notch signalling in context. *Nature reviews. Molecular cell biology*. 2016;17:722-735

25. Accili D, Arden KC. Foxos at the crossroads of cellular metabolism, differentiation, and transformation. *Cell*. 2004;117:421-426

26. Wilhelm K, Happel K, Eelen G, Schoors S, Oellerich MF, Lim R, Zimmermann B, Aspalter IM, Franco CA, Boettger T, Braun T, Fruttiger M, Rajewsky K, Keller C, Bruning JC, Gerhardt H, Carmeliet P, Potente M. Foxo1 couples metabolic activity and growth state in the vascular endothelium. *Nature*. 2016;529:216-220

27. Kitamura T, Kitamura YI, Funahashi Y, Shawber CJ, Castrillon DH, Kollipara R, DePinho RA, Kitajewski J, Accili D. A foxo/notch pathway controls myogenic differentiation and fiber type specification. *J Clin Invest*. 2007;117:2477-2485

28. Lee J, Fei P, Sevag Packard RR, Kang H, Xu H, Baek KI, Jen N, Chen J, Yen H, Kuo CC, Chi NC, Ho CM, Li R, Hsiai TK. 4-dimensional light-sheet microscopy to elucidate shear stress modulation of cardiac trabeculation. *J Clin Invest*. 2016;126:3158

29. MacKenzie F, Duriez P, Wong F, Noseda M, Karsan A. Notch4 inhibits endothelial apoptosis via rbp-jkappa-dependent and -independent pathways. *The Journal of biological chemistry*. 2004;279:11657-11663

30. Quillard T, Coupel S, Coulon F, Fitau J, Chatelais M, Cuturi MC, Chiffoleau E, Charreau B. Impaired notch4 activity elicits endothelial cell activation and apoptosis: Implication for transplant arteriosclerosis. *Arteriosclerosis, thrombosis, and vascular biology*. 2008;28:2258-2265

31. Rostama B, Peterson SM, Vary CP, Liaw L. Notch signal integration in the vasculature during remodeling. *Vascular pharmacology*. 2014;63:97-104

32. Walshe TE, Connell P, Cryan L, Ferguson G, Gardiner T, Morrow D, Redmond EM, O'Brien C, Cahill PA. Microvascular retinal endothelial and pericyte cell apoptosis in vitro: Role of hedgehog and notch signaling. *Investigative ophthalmology & visual science*. 2011;52:4472-4483

33. Artavanis-Tsakonas S, Rand MD, Lake RJ. Notch signaling: Cell fate control and signal integration in development. *Science*. 1999;284:770-776

34. Joutel A, Corpechot C, Ducros A, Vahedi K, Chabriat H, Mouton P, Alamowitch S, Domenga V, Cecillion M, Marechal E, Maciazek J, Vayssiere C, Cruaud C, Cabanis EA, Ruchoux MM, Weissenbach J, Bach JF, Bousser MG, Tournier-Lasserve E. Notch3 mutations in cadasil, a hereditary adult-onset condition causing stroke and dementia. *Nature*. 1996;383:707-710

35. Hellstrom M, Phng LK, Hofmann JJ, Wallgard E, Coultas L, Lindblom P, Alva J, Nilsson AK, Karlsson L, Gaiano N, Yoon K, Rossant J, Iruela-Arispe ML, Kalen M, Gerhardt H, Betsholtz C. Dll4 signalling through notch1 regulates formation of tip cells during angiogenesis. *Nature*. 2007;445:776-780

36. Lobov IB, Renard RA, Papadopoulos N, Gale NW, Thurston G, Yancopoulos GD, Wiegand SJ. Delta-like ligand 4 (dll4) is induced by vegf as a negative regulator of angiogenic sprouting. *Proceedings of the National Academy of Sciences of the United States of America*. 2007;104:3219-3224

37. Kim DY, Hwang I, Muller FL, Paik JH. Functional regulation of foxo1 in neural stem cell differentiation. *Cell Death Differ*. 2015;22:2034-2045

38. Brook RD, Franklin B, Cascio W, Hong Y, Howard G, Lipsett M, Luepker R, Mittleman M, Samet J, Smith SC, Jr., Tager I, Expert Panel on P, Prevention Science of the American Heart A. Air pollution and cardiovascular disease: A statement for

healthcare professionals from the expert panel on population and prevention science of the american heart association. *Circulation*. 2004;109:2655-2671

39. Li R, Navab K, Hough G, Daher N, Zhang M, Mittelstein D, Lee K, Pakbin P, Saffari A, Bhetraratana M, Sulaiman D, Beebe T, Wu L, Jen N, Wine E, Tseng CH, Araujo JA, Fogelman A, Sioutas C, Navab M, Hsiai TK. Effect of exposure to atmospheric ultrafine particles on production of free fatty acids and lipid metabolites in the mouse small intestine. *Environ Health Perspect*. 2015;123:34-41

40. Schulz H, Harder V, Ibald-Mulli A, Khandoga A, Koenig W, Krombach F, Radykewicz R, Stampfl A, Thorand B, Peters A. Cardiovascular effects of fine and ultrafine particles. *J Aerosol Med*. 2005;18:1-22

41. Frampton MW. Systemic and cardiovascular effects of airway injury and inflammation: Ultrafine particle exposure in humans. *Environ Health Persp*. 2001;109:529-532

42. Nemmar A, Hoet PHM, Vanquickenborne B, Dinsdale D, Thomeer M, Hoylaerts MF, Vanbilloen H, Mortelmans L, Nemery B. Passage of inhaled particles into the blood circulation in humans. *Circulation*. 2002;105:411-414

43. Peters A, Wichmann HE, Tuch T, Heinrich J, Heyder J. Respiratory effects are associated with the number of ultrafine particles. *American journal of respiratory and critical care medicine*. 1997;155:1376-1383

44. McCreanor J, Cullinan P, Nieuwenhuijsen MJ, Stewart-Evans J, Malliarou E, Jarup L, Harrington R, Svartengren M, Han IK, Ohman-Strickland P, Chung KF, Zhang J. Respiratory effects of exposure to diesel traffic in persons with asthma. *The New England journal of medicine*. 2007;357:2348-2358

45. Pekkanen J, Peters A, Hoek G, Tiittanen P, Brunekreef B, de Hartog J, Heinrich J, Ibald-Mulli A, Kreyling WG, Lanki T, Timonen KL, Vanninen E. Particulate air pollution and risk of st-segment depression during repeated submaximal exercise tests among subjects with coronary heart disease: The exposure and risk assessment for fine and ultrafine particles in ambient air (ultra) study. *Circulation*. 2002;106:933-938

46. Henneberger A, Zareba W, Ibald-Mulli A, Ruckerl R, Cyrys J, Couderc JP, Mykins B, Woelke G, Wichmann HE, Peters A. Repolarization changes induced by air pollution in ischemic heart disease patients. *Environ Health Perspect*. 2005;113:440-446

47. Li R, Ning Z, Majumdar R, Cui J, Takabe W, Jen N, Sioutas C, Hsiai T. Ultrafine particles from diesel vehicle emissions at different driving cycles induce differential vascular pro-inflammatory responses: Implication of chemical components and nf-kappab signaling. *Part Fibre Toxicol*. 2010;7:6

48. Li R, Yang J, Saffari A, Jacobs J, Baek KI, Hough G, Larauche MH, Ma J, Jen N, Moussaoui N, Zhou B, Kang H, Reddy S, Henning SM, Campen MJ, Pisegna J, Li Z, Fogelman AM, Sioutas C, Navab M, Hsiai TK. Ambient ultrafine particle ingestion alters gut microbiota in association with increased atherogenic lipid metabolites. *Scientific reports*. 2017;7:42906

49. Ono K. Micrornas and cardiovascular remodeling. *Adv Exp Med Biol*. 2015;888:197-213

50. Yu B, Zhou S, Wang Y, Qian T, Ding G, Ding F, Gu X. Mir-221 and mir-222 promote schwann cell proliferation and migration by targeting lass2 after sciatic nerve injury. *Journal of cell science*. 2012;125:2675-2683

51. Wu L, Li H, Jia CY, Cheng W, Yu M, Peng M, Zhu Y, Zhao Q, Dong YW, Shao K, Wu A, Wu XZ. Microrna-223 regulates foxo1 expression and cell proliferation. *FEBS letters*. 2012;586:1038-1043

52. Izzotti A, Larghero P, Balansky R, Pfeffer U, Steele VE, De Flora S. Interplay between histopathological alterations, cigarette smoke and chemopreventive agents in defining microrna profiles in mouse lung. *Mutation research*. 2011;717:17-24

53. Ooi AT, Ram S, Kuo A, Gilbert JL, Yan W, Pellegrini M, Nickerson DW, Chatila TA, Gomperts BN. Identification of an interleukin 13-induced epigenetic signature in allergic airway inflammation. *American journal of translational research*. 2012;4:219-228

54. Zhao M, Luo R, Liu Y, Gao L, Fu Z, Fu Q, Luo X, Chen Y, Deng X, Liang Z, Li X, Cheng C, Liu Z, Fang W. Mir-3188 regulates nasopharyngeal carcinoma proliferation and chemosensitivity through a foxo1-modulated positive feedback loop with mtor-p-pi3k/akt-c-jun. *Nature communications*. 2016;7:11309

55. Lian R, Lu B, Jiao L, Li S, Wang H, Miao W, Yu W. Mir-132 plays an oncogenic role in laryngeal squamous cell carcinoma by targeting foxo1 and activating the pi3k/akt pathway. *European journal of pharmacology*. 2016;792:1-6

56. Bleck B, Grunig G, Chiu A, Liu M, Gordon T, Kazeros A, Reibman J. Microrna-375 regulation of thymic stromal lymphopoietin by diesel exhaust particles and ambient particulate matter in human bronchial epithelial cells. *J Immunol*. 2013;190:3757-3763

57. Rodosthenous RS, Coull BA, Lu Q, Vokonas PS, Schwartz JD, Baccarelli AA. Ambient particulate matter and micrornas in extracellular vesicles: A pilot study of older individuals. *Part Fibre Toxicol*. 2016;13:13

58. Yang L, Hou XY, Wei Y, Thai P, Chai F. Biomarkers of the health outcomes associated with ambient particulate matter exposure. *Sci Total Environ*. 2017;579:1446-1459

59. Takabe W, Li R, Ai L, Yu F, Berliner JA, Hsiai TK. Oxidized low-density lipoprotein-activated c-jun nh2-terminal kinase regulates manganese superoxide dismutase ubiquitination: Implication for mitochondrial redox status and apoptosis. *Arterioscler Thromb Vasc Biol*. 2010;30:436-441

60. Huang T, Wang-Johanning F, Zhou F, Kallon H, Wei Y. Micrornas serve as a bridge between oxidative stress and gastric cancer (review). *International journal of oncology*. 2016;49:1791-1800

61. Chavez MN, Aedo G, Fierro FA, Allende ML, Egana JT. Zebrafish as an emerging model organism to study angiogenesis in development and regeneration. *Front Physiol*. 2016;7:56

62. Verma V, Polidori A, Schauer JJ, Shafer MM, Cassee FR, Sioutas C. Physicochemical and toxicological profiles of particulate matter in los angeles during the october 2007 southern california wildfires. *Environ Sci Technol*. 2009;43:954-960

63. Misra C, Kim S, Shen S, Sioutas C. A high flow rate, very low pressure drop impactor for inertial separation of ultrafine from accumulation mode particles. *Journal of Aerosol Science*. 2002;33:735-752

64. Herner JD, Green PG, Kleeman MJ. Measuring the trace elemental composition of size-resolved airborne particles. *Environ Sci Technol*. 2006;40:1925-1933

65. Stone EA, Hedman CJ, Sheesley RJ, Shafer MM, Schauer JJ. Investigating the chemical nature of humic-like substances (hulis) in north american atmospheric aerosols

by liquid chromatography tandem mass spectrometry. *Atmospheric Environment*. 2009;43:4205-4213

66. Li R, Ning Z, Cui J, Yu F, Sioutas C, Hsiai T. Diesel exhaust particles modulate vascular endothelial cell permeability: Implication of zo-1 expression. *Toxicology letters*. 2010;197:163-168

67. Li R, Chen W, Yanes R, Lee S, Berliner JA. Okl38 is an oxidative stress response gene stimulated by oxidized phospholipids. *J Lipid Res*. 2007;48:709-715

# CHAPTER IV

## FLOW-RESPONSIVE VASCULAR ENDOTHELIAL GROWTH FACTOR RECEPTOR-PROTEIN KINASE C ISOFORM EPSILON SIGNALING MEDIATED GLYCOLYTIC METABOLITES FOR VASCULAR REPAIR

Baek KI, Li R, Jen N, Choi H, Kaboodrangi A, Ping P, Liem D, Beebe T, Hsiai TK

Original article, published in ***Antioxidants and redox signaling***, 2018, Jan 1; 28(1): 31-43

## Introduction

Hemodynamic forces modulate mammalian cell metabolism [1]. Unidirectional pulsatile and bi-directional oscillatory flow largely determine the focal but eccentric distribution of vascular oxidative stress [2-4], post-translational protein modifications, and metabolic pathways [1, 3, 5]. Metabolomic analyses have led to the discovery of new metabolic biomarkers and therapeutic targets, including polyamines such as spermine for acute stroke, cinnamoylglycine, nicotinamide, and cysteine-glutathione disulfide for renal cancer, and 3-hydroxykynurenine and oxidized glutathione for Parkinson disease [6-8]. Thus, elucidating flow-mediated metabolomic changes provides an entry point to uncover metabolites participating in endothelial homeostasis [9, 10], migration [11], vascular development [12], and physical activity [13].

Pulsatile (PSS) and oscillatory shear stress (OSS) differentially activate canonical Wnt-β-catenin signaling to modulate vascular development and repair [14, 15]. PSS and OSS promote the differentiation of embryonic stem cells to vascular progenitors in angiogenesis [16, 17]. Laminar flow-dependent VEGF and eNOS phosphorylation induce nitric oxide (·NO)-mediated Protein Kinase C isoform epsilon (PKCε) signaling to confer mitochondrial homeostasis [18, 19]. While VEGF-mediated angiogenesis promotes tumor initiation and progression [20, 21], the mechanisms underlying flow-mediated VEGF-PKCε signaling to modulate endothelial metabolites for vascular repair remain unexplored.

Endothelial glycolysis is mechano-responsive [22]. Glucose uptake in endothelial cells (EC) is metabolized to pyruvate via the glycolytic pathway [23]. Rather than relying on oxidative metabolism for mitochondrial respiration, ECs generate over 80% of their ATP from the glycolytic pathway [23]. ECs increase their glycolytic flux when switching from quiescence to proliferation and migration states [24]. A recent study reports that laminar shear stress

activates Krüppel-like factor 2 (KLF2) to suppress 6-phosphofructo-2-kinase/fructose-2,6-biphosphatase 3 (PFKFB3)-mediated glycolysis in ECs, mitigating angiogenesis and vessel sprouting [25], whereas flow-sensitive VEGFR signaling up-regulates PFKFB3-driven glycolysis [12, 24]. Shear-mediated nitric oxide production induces PKCε [26, 27], which, in turn, attenuates mitochondrial reactive oxygen species following ischemia/reperfusion injury [28, 29]. Flow-responsive VEGF-eNOS-signaling activates PKCε to modulate EC proliferation, lumen formation, and homeostasis [30, 31]. Nevertheless, the mechanotransduction mechanism underlying PKCε-mediated metabolomic pathways to mediate vascular repair remains elusive.

In this context, we sought to elucidate the flow-sensitive VEGFR-PKCε signaling to mediate glycolytic metabolites for vascular repair. Both PSS and OSS promoted VEGFR-dependent PKCε and PFKFB3 expression to promote glycolytic flux. Further, we demonstrated that shear stress-mediated PKCε signaling rescued vascular regeneration in *Tg(flk-1:EGFP)* zebrafish tail amputation model, and the glycolytic metabolite, dihydroxyacetone (DHA), restored tube formation and vascular repair in response to silencing PKCε. Thus, our study indicates that flow-sensitive VEGFR-PKCε-signaling promotes glycolytic metabolites for vascular repair.

## Materials & Methods

### Ethics statement

All animal experiments were performed in compliance with UCLA Institutional Animal Care and Use Committee (IACUC) protocols, under a project license also approved by the UCLA IACUC. Humane care and use of animals were observed to minimize distress and discomfort.

**Vascular Endothelial Cell Culture**

Human aortic endothelial cells (HAEC) were purchased from Cell Applications and cultured in endothelial growth medium (Cell Applications) supplemented with 5% Fetal Bovine Serum (FBS) (Gibco). HAEC were propagated for experiments between passages 5 and 10.

**siRNA Transfection**

siRNA transfection was performed with Lipofectamine RNAiMax (Invitrogen). HAEC were plated in 6 well plates or standard glass slides on the day prior to transfection. The cells were transfected with 50 nM PKCε or KDR siRNA (Qiagen). Transfection media were changed to normal growth media after 4 hours of transfection. Cells were used for confirmation of gene knockdown or assay at 48 hours after transfection.

**Chemical Reagents**

Human recombinant Vascular Endothelial Growth Factor (VEGF) was purchased from Fisher Scientific and dissolved in PBS. Cediranib was purchased from SelleckChem and dissolved in DMSO.

**PKCε activity assay**

PKCε activity assay with the ADP-Glo Kinase assay kit (Promega, WI) was performed to assess activity change of PKCε in response to PSS and OSS. A confluent monolayer of HAEC on glass slides were subjected to 3 flow conditions 1) static, 2) PSS, and 3) OSS as previously described [32]. Following flow exposure, HAEC underwent the kinase reaction by adding a mixture of kinase reaction buffer. After a short incubation, ADP-Glo™ reagent

(Promega, WI) was added to terminate the kinase reaction and to deplete residual ATPs in the lysates. Next, a mixture of kinase detection reagents was added to introduce luciferase and luciferin from newly synthesized ATP, converted from ADP. The specificity was achieved by using PKCε specific peptide as substrate. Luciferase activities were measured using the Glo-Max Luminometer (Promega, WI) as a readout of PKCε activity.

**Quantitative Real-Time PCR Analysis**

Protein Kinase C isoform epsilon (PKCε) and PFKFB3 mRNA expression was measured by quantitative RT-PCR. Total RNA was isolated using Aurum Total RNA Mini Kit (Bio-Rad). RNA was reverse-transcribed using iScript cDNA synthesis kit (Bio-Rad), followed by PCR amplification with iScript RT-PCR Kit with SYBR Green (Bio-Rad). The expression levels were normalized to actin.

The forward primer sequence for PKCε was 5'- GAG CCG CCA CTT CGA GGA CTG -3' and the reverse primer was 5'- TTG TGG CCG TTG ACC TGA TGG -3'. The forward primer sequence for Actin was 5'- ACC CAC ACT GTG CCC ATC TAC -3' and the reverse primer was 5'- TCG GTG AGG ATC TTC ATG AGG -3'. The forward primer sequence for PFKFB3 was 5' – GGA GGC TGT GAA GCA GTA CA – 3' and the reverse primer was 5' – CAG CTA AGG CAC ATT GCT TC – 3'. The differences in $C_T$ values for various intervals versus control were used to determine the relative difference in the levels of PKCε mRNA expression.

**SeaHorse Mitochondrial Function Analysis**

HAEC were infected with either CA-PKCε recombinant adenovirus (Adv-CA-PKCε) or DN-PKCε recombinant adenovirus (Adv-DN-PKCε), followed by treatment with or without

50 μM $H_2O_2$ in DMEM + 1% FBS. Mitochondrial function was analyzed using the Seahorse XF analyzer system as described with a 24-well assay plate format [33]. 20,000 cells were loaded to individual well of the 24 well SeaHorse analysis plate. Glycolysis levels were determined through measurements of the extracellular acidification rate [34]. Basal glycolysis was measured without treatment and maximum glycolysis was determined by treatment of the cells with 4μM carbonyl cyanide p-trifluoromethoxy-phenylhydrazone (FCCP), the mitochondrial uncoupler, after basal measurement.

**Dynamic Flow System to Assess Vascular Endothelial Metabolites**

A dynamic flow system was used to simulate well-defined PSS and OSS as previously described [32]. The flow system was designed to generate physiologic shear stress occurring at human arterial branching points with well-defined slew rates, time-averaged shear stress, frequency, and amplitude. Confluent monolayer of HAEC grown on glass slides were subjected to three flow conditions at 1 Hz for 4 hours: 1) static control at no flow state, 2) pulsatile flow with time-averaged shear stress of 23 dyne·cm$^{-2}$ accompanied by a stress slew rate ($\partial\tau/\partial t$ = 71 dyne · cm$^{-2}$ · s$^{-1}$), and 3) O\oscillating flow (0.1 ± 4 dyne·cm$^{-2}$). Endothelial cells were maintained in DMEM culture media supplemented with 1% FBS at a temperature of 37°C and pH of 7.4 during flow exposure.

**Endothelial Metabolomic Analysis**

Metabolite samples were collected from HAEC treated with PSS ($\tau_{ave}$ = 50 dyne·cm$^{-2}$ accompanied by $\partial\tau/\partial t$ = 71 dyne·cm$^{-2}$·s$^{-1}$ at 1 Hz), OSS (0±3 dyne·cm$^{-2}$ with $\tau_{ave}$=0 dyne·cm$^{-2}$ at 1 Hz), or static conditions for 4 hours (**Fig. S7**). For oscillating flow, minimal

forward flow at a mean shear stress of 0.2 dyne·cm$^{-2}$ was provided every hour to deliver nutrients and to remove waste products. Cells were trypsinized, fixed in 4% PFA, and immediately stored at -80°C prior to shipment in dry ice to the West Coast Metabolomics Center at UC Davis. Gas chromatography time-of-flight mass spectrometry (GC-TOF) analysis was performed to identify 156 known metabolites and 290 unknown compounds [35]. Metabolites were reported with retention index, quantification mass and full mass spectra. Quantification was by peak height without internal standards for absolute concentration.

**Principal Component Analysis (PCA) to assess significant metabolite change**

Principal Component Analyses (PCAs) were carried out using the programming language R, version 2.14.0. Built-in 'ade4' package was utilized to plot factorial maps with representation of point classes which are denoted as Static, PSS, and OSS. In prior to perform PCAs, the concentrations of subjected metabolites were normalized by using Pareto scaling method to put the measurements of different metabolites on the close scale. The x-axis in the figures was depicted as the first principal component (PC1) representing the space with the largest variance in data, whereas the y-axis was depicted as the second principal component (PC2) representing the space with the second largest variance. The ovals are 95% inertia ellipses.

**Immunohistochemistry**

Vascular rings corresponding to the aortic arch and thoracic aorta were cut from rabbit aorta segments, and immersed in 4% paraformaldehyde. They were embedded in paraffin and cut into serial 5-μm sections. Immunostaining was performed with standard

techniques in paraffin embedded vascular tissue. Hematoxylin and eosin staining was used to observe gross vascular morphology, and PKCε and PFKFB3 staining was performed using mouse monoclonal (PKCε, ABCAM) and goat polyclonal (PFKFB3, SCBT) antibodies. Tissue sections were viewed with a microscope and images were captured with a CCD digital camera. Quantification of staining intensity was performed using ImageJ software.

**Tube Formation Assay**

HAEC cells were grown in a 96-well plate at 20,000 cells/well on a 100 μL Matrigel Growth-factor-reduced matrix (BD Biosciences) that was allowed to solidify before seeding cells in DMEM + 5% FBS + 25 ng/mL VEGF. Tube growth was allowed for six hours, and wells were imaged to visualize tube formation with a microscope (Olympus). Images were analyzed using S.CORE image analysis, with tube formation index (TFI) representing a quantification of the images.

**Transgenic *Tg(flk-1:EGFP)* Zebrafish Model to Study Vascular Injury and Repair**

*Tg(flk-1:EGFP)* transgenic zebrafish embryos were generously provided by Prof. Ellen C. Lien (Children's Hospital Los Angeles, Los Angeles, CA) for assessing vascular injury and repair in response to tail amputation. *Flk-1*, VEGF receptor 1, is tissue-specific for vascular endothelial cells. Fish embryos were injected with either a PKCε morpholino (MO) or a control nonsense MO. Injection was validated by qRT-PCR analysis of PKCε gene expression. The following MO sequences were used. Standard Control negative MO: 5'- CCT CTT ACC TCA GTT ACA ATT TAT A-3'; Zebrafish *p53* apoptosis suppression MO (p53MO): 5'- GCG CCA TTG CTT TGC AAG AAT TG -3'; *PKCε* splice

MO: 5'- CTC CAT TAA AAA CCA CCA TGA TGA C -3'; *GATA-1a* MO: 5'-CTGCAAGTGTAGTATTGAAGATGTC-3'; *TNNT-2a* MO: (5'-CGCGTGGACAGATTCAAGAGCCCTC-3'. MOs were dissolved in water to make 0.3mM stock solution with addition of 0.1mM p53 MO. Immediately after collection at 0 hpf, approximately 30-40 embryos were randomly chosen for micro-injections. All of the embryos were maintained in E3 medium at 28˚C.

Injected fish larvae were grown to 72 hpf in standard E3 medium, followed by amputation of the posterior tail segment ~100 μm from the tip of the tail. The larvae were anesthetized in 0.02% tricaine solution to allow for precise placement. Amputation was performed with a surgical scalpel under a stereo microscope (MEIJI Techno EMZ series, MEIJI, Japan) for both control and treatment groups. After amputation, fish were separated to allow for same-fish control. Fish tail sections were imaged (Olympus IX71, Olympus, Japan) to visualize the blood vessels immediately after amputation and every 24 hours thereafter over the next 3 days. Regeneration of blood vessels was compared between the different treatment groups at 0 dpa, 1 dpa, and 3 dpa.

**Cloning of PKCε mRNA for Rescue**

Mouse PKCε cDNA was amplified from a donor plasmid (Addgene) and cloned into the plasmid pCS2+ at the BamH I and EcoR I sites. Clones with the PKCε cDNA insert were selected by PCR screening. The pCS2+PKCε plasmid was verified by transfecting the plasmids into HEK-293 cells, followed by detecting PKCε protein expression by Western blot with anti-PKCε antibody. mRNA was synthesized from the cloned plasmid using the mMessage SP6 kit (Invitrogen, CA). Transcribed PKCε mRNA was purified with the total RNA isolation kit (Bio-Rad) for *in vivo* rescue experiments.

**Blood Shear Stress Modulation**

Shear stress ($\tau$) is characterized as dynamic viscosity ($\mu$) of fluid multiplied by shear rate ($\dot{\gamma}$), defined as a gradient of velocity between two adjacent fluid layers [36].

$$\tau = \mu \cdot \dot{\gamma} = \mu \frac{\partial u_x}{\partial y} \quad (1)$$

where $\frac{\partial u_x}{\partial y}$ is the tangential velocity gradient between two adjacent fluid layers. Since shear stress is a function of viscosity ($\mu$), injection of *GATA-1a* MO to inhibit erythrocytosis reduced viscosity, whereas injection of *EPO* mRNA resulted in the opposite effects to the endothelium. (**Supplemental Videos 1-3**)

**Western Blot Analysis**

Cells were harvested, washed with phosphate-buffered saline and lysed with RIPA buffer. The lysate was centrifuged at 12,000g for 10 minutes, and the resulting supernatants were used as the entire cell lysate. Proteins were separated by 4–20% polyacrylamide gel with SDS and electroblotted onto the polyvinylidene difluoride membranes (GE Healthcare) and were blocked overnight at 4°C in Tris buffered saline-Tween20 (TBS-T) containing 5% non-fat dry milk (BioRad Laboratory). PKCε protein expression was detected with anti-PKCε (Santa Cruz Biotech), and equal loading was verified by blotting with anti-β-tubulin (Millipore Inc). After treatment with peroxidase-conjugated anti-goat (Santa Cruz) or anti-mouse IgG antibody (Jackson ImmunoResearch) for 1 hour at room temperature, chemilluminescence signal was developed with Supersignal Western Pico (Pierce) and recorded with FluorChem FC2 (Alpha Inotech Inc). Antibodies against autophagy-associated genes were purchased from Boster Biological Technologies for

p62. Parallel blots were performed with anti-β-tubulin (Millipore) for loading normalization. Densitometry was performed to quantify blot bands as previously described (34).

**Mitochondrial Superoxide Assay**

Mitochondrial superoxide ($mtO_2^{\cdot-}$) was analyzed both quantitatively by flow cytometry and qualitatively by fluorescent imaging as previously described (74). Briefly, in a 6-well format for FACS analysis, cells were incubated with 10 μM mitoSOX dye (Invitrogen) for 15 minutes, then lysed and rinsed three times with PBS buffer to remove residual dye. Samples were then analyzed using FACS analysis, with gating to remove debris or clusters.

For qualitative imaging of $mtO_2^{\cdot-}$ levels during tube formation, tube formation assay was performed as described above, with media that was absent of phenol red. At 6 hr, cells were incubated with 10 μM mitoSOX dye for 30 minutes, rinsed three times with DPBS, and then fixed with PFA. Cells were imaged using fluorescent microscopy.

**Statistical analysis**

Data were expressed as mean ± SEM unless otherwise stated. Multiple comparisons were performed by one-way analysis of variance (ANOVA), and statistical significance for comparison between two groups was determined by student t-test, two sample proportional z-test, or Wilcoxon rank-sum test (non-parametric analysis) when data was not normally distributed. A $p$-value $< 0.05$ was considered statistically significant.

## Results

### Flow-Responsive PKCε Mediated Endothelial Glycolysis

PSS and OSS differentially increased PKCε mRNA expression by 65% and 134%, respectively, whereas the VEGFR-inhibitor, cediranib at 10 μM or VEGFR2 knockdown with siRNA inhibited shear stress-induced PKCε mRNA and protein expression (**Fig. 1A** and **Fig. S1A**). PSS and OSS further increased PKCε activity by 60% and 65%, respectively (**Fig. 1B**). PSS and OSS also increased PFKFB3 mRNA and protein expression, which was attenuated by siPKCε (**Fig. 1C** and **Fig. S1C**). As a corollary, constitutively active PKCε (CA-PKCε) via recombinant adenovirus (Adv-CA-PKCε) infection increased, whereas dominant negative PKCε (DN-PKCε) decreased PFKFB3 mRNA and protein expression ($p < 0.05$ vs. Adv-LacZ control, n=3) (**Fig. 1D and Fig. S1B**). PKCε and PFKFB3 immuno-staining was present in PSS- and OSS-exposed endothelial lining in the aortic arch and thoracic aorta from the New Zealand White (NZW) rabbits (**Fig. S2**). In addition, PKCε-mediated metabolic activity was quantified by using a SeaHorse Flux Analyzer. CA-PKCε increased basal (3.11-fold, $p < 0.01$, n=4) and maximum extracellular acidification rates (ECAR) (2.52-fold, $p < 0.01$ vs. DN-PKCε, n=4) for proton production as an indicator of glycolytic flux [37]. This elevated glycolytic flux was further validated with $H_2O_2$ (50 μM)-induced oxidative stress (2.13-fold basal ECAR, 2.45-fold maximum ECAR, $p < 0.01$, n=4) (**Figs. 1E, F**).

### Shear Stress Modulated PKCε-Dependent Glycolytic Metabolites

Our metabolomic analysis of 156 HAEC metabolites with known identity (**Supplemental Table 1**) revealed that four metabolites were significantly up-regulated in response to PSS and OSS, including putrescine ($C_4H_{12}N_2$) and dihydroxyacetone ($C_3H_6O_3$), whereas

aspartic acid ($C_4H_7NO_4$) was decreased (**Fig. S3**). To validate flow-mediated glycolytic metabolites, we performed metabolomic analysis in HAEC transfected with scrambled siRNA (Scr) or siPKCε in response to 1) Static, 2) PSS, and 3) OSS conditions. Principal component analysis (PCA) demonstrated significant separation among 16 metabolites in the Scrambled (Scr) group and among 13 in the siPKCε group ($p < 0.05$, n=6) (**Figs. 2A-2D**). Both PSS and OSS up-regulated putrescine, glucose ($C_6H_{12}O_6$), fructose ($C_6H_{12}O_6$), and dihydroxyacetone (DHA). In the presence of siPKCε transfection, OSS attenuated glucose, fructose, and DHA to a greater degree than did PSS. siPKCε transfection also increased glucose and fructose, implicating a reduction in glycolysis and/or fructolysis. Furthermore, siPKCε attenuated both PSS- and OSS-mediated increases in DHA (**Fig. 2E**). Thus, both PSS and OSS modulated PKCε-dependent glucose, fructose and DHA as well as PKCε-independent putrescine.

**PKCε Mediated Tube Formation and Vascular Repair**

In an *in vitro* Matrigel model, siPKCε decreased endothelial tube formation by 40% as quantified by tube lengths ($p < 0.05$ vs. Scr siRNA, n=3) (**Figs. 3A, B**). Consitutively-active PKCε (CA-PKCε) increased tube formation by 2.1-fold ($p < 0.05$ vs. LacZ, n=3) (**Figs. 3C, D**). VEGFR-inhibitor, cediranib, disrupted tube formation in Adv-LacZ-infected HAEC (**Figs. 3C, D**), and this disruption was restored with Adv-CA-PKCε (**Figs. 3C, D**). Glycolysis-relevant metabolites (glucose, fructose, and DHA) promoted HAEC tube formation, whereas a gluconeogenesis-relevant metabolite (aspartic acid) had no effects (**Figs. S4**). In a transgenic *Tg(flk-1:EGFP)* zebrafish model of tail regeneration, control *p53* MO injection supported vascular regeneration as visualized by a closed loop between the dorsal longitudinal anastomotic vessels (DLAV) and dorsal aortas (DA) at 3 days post

amputation (dpa) (**Fig. 3E**). *PKCε* MO injection impaired, whereas *PKCε* mRNA restored vascular regeneration at 3 dpa (**Fig. 3E**). Taken together, PKCε-mediated glycolytic metabolites promoted tube formation and vascular repair.

**Genetic Manipulations of Shear Stress-Mediated Vascular Repair**

Following *GATA-1a* MO injection to reduce viscosity-dependent shear stress (**Supplemental Video 1, 3**), zebrafish embryos failed to develop vascular regeneration at 3 dpa until 5 dpa ($p < 0.05$ vs. control, n=30) (**Fig. 4C**). Following *TNNT-2* MO injection to inhibit myocardial contraction and blood flow, zebrafish embryos also failed to develop tail regeneration at 3 dpa ($p < 0.05$ vs. control, n=5) (**Fig. 4E**), and they failed to thrive at 5 dpa. Following erythropoietin mRNA injection to augment erythrocytosis as a means of restoring viscosity-dependent shear stress (**Supplemental Video 2**), zebrafish embryos developed tail regeneration at 3 and 5 dpa ($p < 0.05$ vs. control, n=30) (**Fig. 4E**). As a corollary, rescue of *GATA-1a* MO injected embryos with *PKCε* mRNA restored vascular regeneration at 3 and 5 dpa ($p < 0.05$ vs. *GATA-1a* MO-alone injected group, n=30) (**Fig. 4F**). Vascular repair was quantitatively compared in response to the genetic manipulations (**Fig. 4G**), supporting the important roles of shear stress and PKCε to promote vascular repair.

**PKCε-Dependent Dihydroxyacetone Rescued Vascular Repair**

In an *in vitro* Matrigel model, siPKCε attenuated tube formation, which was partially rescued by the PKCε-dependent glycolytic metabolite, DHA ($p < 0.05$ vs. Scr siRNA, n=4) (**Figs. 5A, B)**. In the zebrafish tail amputation model, DHA restored vascular repair from 67% to 100% in the control MO-injected fish at 6 dpa ($p < 0.05$ vs. control, n=4). Further,

DHA rescued vascular repair from 30% to 80% in PKCε MO-injected fish ($p < 0.05$ vs. control, n=30) (**Figs. 5C, D**). These findings strengthen the notion that PKCε-dependent DHA promoted endothelial tube formation and vascular repair.

## Discussion

The novelty of this study resides in establishing flow-mediated VEGFR-PKCε-PFKFB3 signaling to promote glycolytic metabolite, dihydroxyacetone (DHA), for vascular repair. Metabolomic analysis revealed that pulsatile (PSS) and oscillatory shear stress (OSS) modulated PKCε-dependent endothelial PFKFB3 expression to mediate glycolytic metabolites. In the NZW rabbit aortic arch and descending aorta, PKCε and PFKFB3 immunostaining was present in the PSS- and OSS-exposed regions. In the zebrafish model of tail amputation, shear stress plays an important epigenetic role with PKCε to mediate vascular regeneration. Thus, we provide a new mechano-metabolomic pathway to increase the glycolytic metabolite, DHA, for vascular regeneration (**Fig. 6**).

Our data support that the characteristics of flow, namely PSS ($\tau_{ave}$ = 50 dyne·cm$^{-2}$ accompanied by a slew rate at $\partial\tau/\partial t$ =71 dyne·cm$^{-2}$·s$^{-1}$ at 1 Hz) and OSS (0±3 dyne·cm$^{-2}$ with $\tau_{ave}$= 0 dyne·cm$^{-2}$ at 1 Hz), modulate VEGF receptor-PKCε-PFKFB3 signaling to increase glycolytic metabolites (**Fig. 1E**). Doddaballapur and Boon *et al.* reported that laminar shear stress (LSS; $\tau_{ave}$ = 20 dyne·cm$^{-2}$ at steady state, $\partial\tau/\partial t$ = 0) reduced KLF2-dependent PFKFB3 promoter activity to reduce glycolysis [25], leading to attenuation in angiogenic sprouting [24, 38]. However, the differential effects of LSS vs. OSS to modulate AMPK and Akt activities are well-recognized to promote glycolysis [39]. Furthermore, Jalali

*et al.* demonstrated the role of p60scr and RAS in shear stress-activated endothelial MAPK signaling [40], while induction of PFKFB3 expression in response to MAPK activation has been previously reported in cancer cells [41]. Taken together, these observations highlight the differential characteristics of shear stress to mediate PFKFB3 expression [3, 32].

Hemodynamic shear forces modulate vascular metabolism to maintain cellular homeostasis [9, 10]. Our metabolomic analyses via gas chromatography time-of-flight mass spectrometry (GC-TOF) revealed that PSS and OSS increased DHA, fructose, glucose, and putrescine (**Fig. 2**). DHA is an intermediate metabolite of fructose metabolism, participating in glycolysis in its phosphate form [42]. As a corollary, the glycolysis-related metabolites (namely alanine, glucose, and lactate) were also elevated in response to ischemia/reperfusion (I/R) in the constitutively-active PKCε (CA-PKC) mouse [29]. Thus, these glycolytic metabolites provide a basis for cellular homeostasis [9, 10] and migration [11], vascular development [12], and physical activity [13].

PFKFB3 is a key regulator of glycolysis to promote angiogenic sprouting [12]. In response to the transition from quiescence to proliferation and migration, vascular endothelial cells developed an increased glycolytic flux [24]. During migration, glycolytic enzymes are translocated to lamellipodia for ATP production [24]. Inhibition of PFKFB3 decreases stalk cell proliferation and tip cell migration [12] to reduce vessel sprouting [38]. We further demonstrated PKCε-dependent PFKFB3 expression (**Figs. 1C, D**) and prominent PKCε and PFKFB3 immunostaining in the shear-exposed NZW aorta (**Fig. S2**), supporting the

notion that flow-mediated VEGFR-PKCε-PFKFB3 signaling promotes vascular regeneration.

PKC isoforms are distributed in numerous tissues and cell types. Three phorbol ester/diacylglycerol-dependent PKC isoforms, α-, δ- and ε-, are highly expressed in myocardium [43]. PKCδ and PKCε are two $Ca^{2+}$-independent isoforms implicated in regulation of growth, differentiation and apoptosis of ventricular cells [44]. PKCε over-expression in the CA-PKCε mouse increased glycolytic metabolites in association with cardioprotection following ischemia/reperfusion injury [29]. CA-PKCε over-expression further attenuated $H_2O_2$ -mediated endothelial mitochondrial super oxide ($O_2^{\cdot -}$) production (**Fig. S5)**. In addition to increasing glycolytic flux (**Fig. S2E**), CA-PKCε reduced p62 protein level to promote autophagic flux (**Fig. S6B**). In this context, we present evidence of flow-mediated PKCε signaling to modulate endothelial homeostasis for tube formation and vascular repair.

Zebrafish (*Danio rerio*) comprise a well-established genetic system for studying cardiovascular development and disease [45-47]. Use of zebrafish allows for genetic manipulations of viscosity to change shear stress (**Fig. 4**) (**Equation 1**). Injection of *GATA*-1a MO significantly inhibits erythropoiesis up to 6 dpf [48], resulting in a reduction in viscosity to decrease shear stress, whereas injection of *EPO* mRNA promotes erythrocytosis [49], resulting in a rise in viscosity to increase shear stress. Thus, use of the zebrafish system enabled us to recapitulate shear stress-mediated vascular repair via PKCε and glycolytic metabolite, DHA.

The New Zealand White (NZW) rabbits are a well-established atherosclerotic model for interrogation of the metabolically active lesions [50, 51]. Similar to humans, NZW rabbits developed oxidized LDL-rich lesions in response to high-fat induced hypercholesterolemia [52-54]; thereby, providing an *ex vivo* model to validate endothelial PKCε and PFKFB3 expression (Fig. S2). In this context, both *in vivo* zebrafish and *ex vivo* NZW rabbit models are complementary and synergistic to strengthen the vascular endothelial phenotypes [55].

Despite differential PKCε mRNA and protein expression in response to PSS and OSS (**Fig. 1A**), we observed similar levels of PKCε activity. PKCε is activated by phosphorylation (**Fig. 1B**), and this non-linear relation may stem from post-translational modifications of PKCε protein to influence the level of PKCε phosphorylation (**Figure 1B**), and subsequent PFKFB3 mRNA expression. In addition, the PSS- and OSS-responsive NADPH oxidase system generates reactive oxygen species (ROS) [3, 32]. Despite an increase in PKCε protein expression (**Fig. 1A**), the concomitant production in ROS may be implicated in ubiquitination and protein degradation of PFKFB3 protein expression [56].

The advent of high-throughput "omics" approaches, including epigenomics, transcriptomics, miRnomics, proteomics, and metabolomics [57] has provided new mechanotrasduction strategy to discover biomarkers with therapeutic targets. Jo *et al.* investigated the disturbed flow-mediated metabolites using the blood plasma samples from ApoE$^{-/-}$ mice, and they demonstrated that 128 metabolites were significantly altered, including sphogomyelin, a common mammalian cell membrane sphingolipid in

association with atherosclerosis [58]. Our findings further support that flow-mediated VEGF receptor-PKCε-PFKFB3 signaling increases endothelial glycolytic metabolites for vascular regeneration. In addition, PKCε over-expression promotes glycolytic metabolites for myocardio-protection. Taken together, we elucidated a mechano-metabolomic pathway to promote DHA as a potential biomarker for vascular therapeutics.

**Acknowledgements**

The authors would like to express gratitude to Dr. Manuel Mayr for providing the metabolomic analysis of PKCε-mediated cardiac metabolites. Human constitutively active PKCε and dominant-negative PKCε adenoviruses were generously provided by Dr. Allen Samarel at the Loyola University Medical Center. This study was supported by the National Institutes of Health HL118650, HL083015, and HL129727 (T.K.H.). Chapter IV is a reprint of the article: Baek KI, Li R, Jen N, Choi H, Kaboodrangi A, Ping P, Liem D, Beebe T, Hsiai TK. Flow-responsive vascular endothelial growth factor-protein kinase c isoform epsilon signaling mediated glycolytic metabolites for vascular repair. Antioxid Redox Signal. 28(1): 31-43, 2018 (https://doi.org/10.1089/ars.2017.7044). Reprint was reproduced with permission from the publisher and all of the co-authors of the publication.

## FIGURES

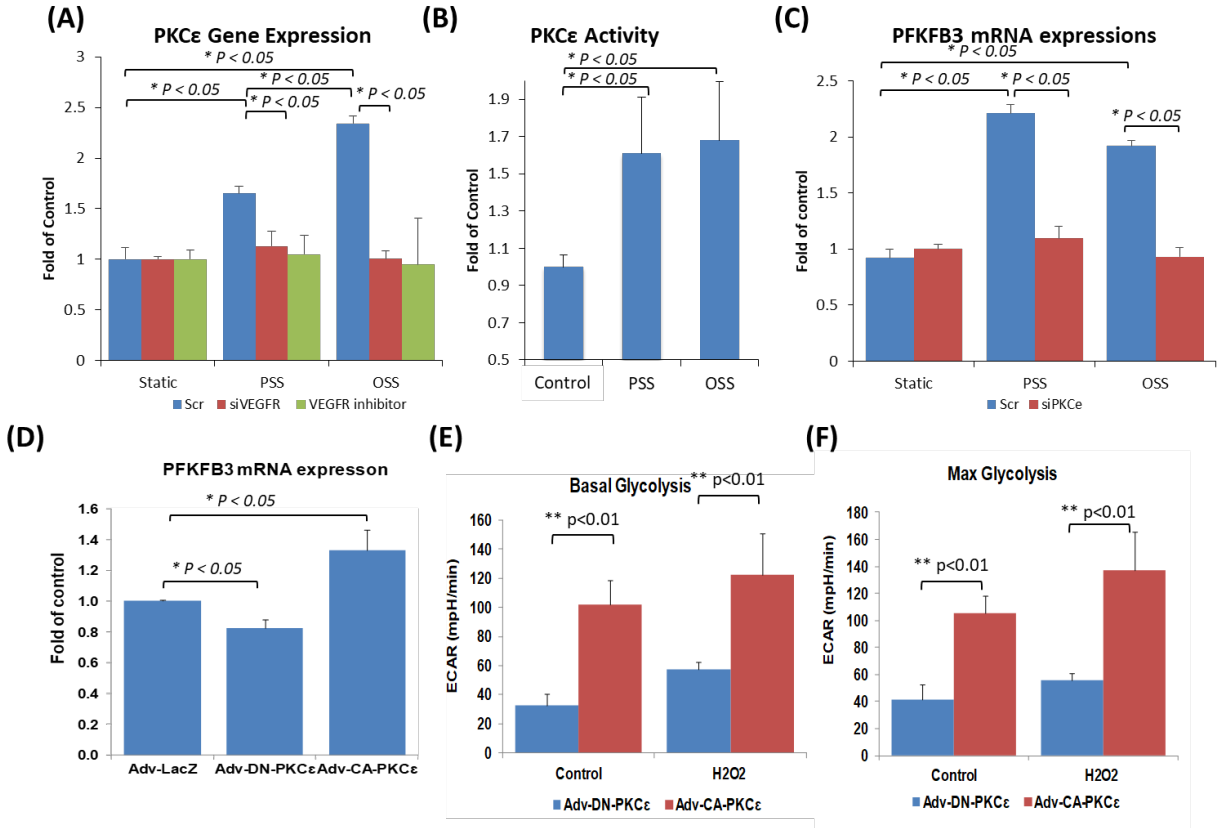


**Figure 1.** Shear Stress-Responsive VEGFR-PKCε-PFKFB3 signaling. **(A)** HAEC were transfected with scrambled siRNA (Scr) or VEGFR2 siRNA (siVEGFR2), or treated with or without VEGFR inhibitor. PSS and OSS differentially up-regulated VEGFR2-dependent PKCε mRNA expressions (* $p < 0.05$, n = 3). **(B)** PSS and OSS also up-regulated PKCε activity (* $p < 0.05$, n = 3). **(C)** PSS and OSS further up-regulated PFKFB3 mRNA expression, which was abrogated in the presence of siPKCε (* $p < 0.05$, n=4). **(D)** CA-PKCε promoted, whereas DN-PKCε reduced the PFKFB3 mRNA expression (* $p < 0.05$ vs. LacZ control, n = 3). **(E-F)** Seahorse assay revealed that CA-PKCε increased both **(E)** basal and **(F)** max extracellular acidification rate (ECAR) as compared to DN-PKCε under baseline conditions and in the presence of $H_2O_2$ at 50 μM (* $p < 0.01$, n=4)

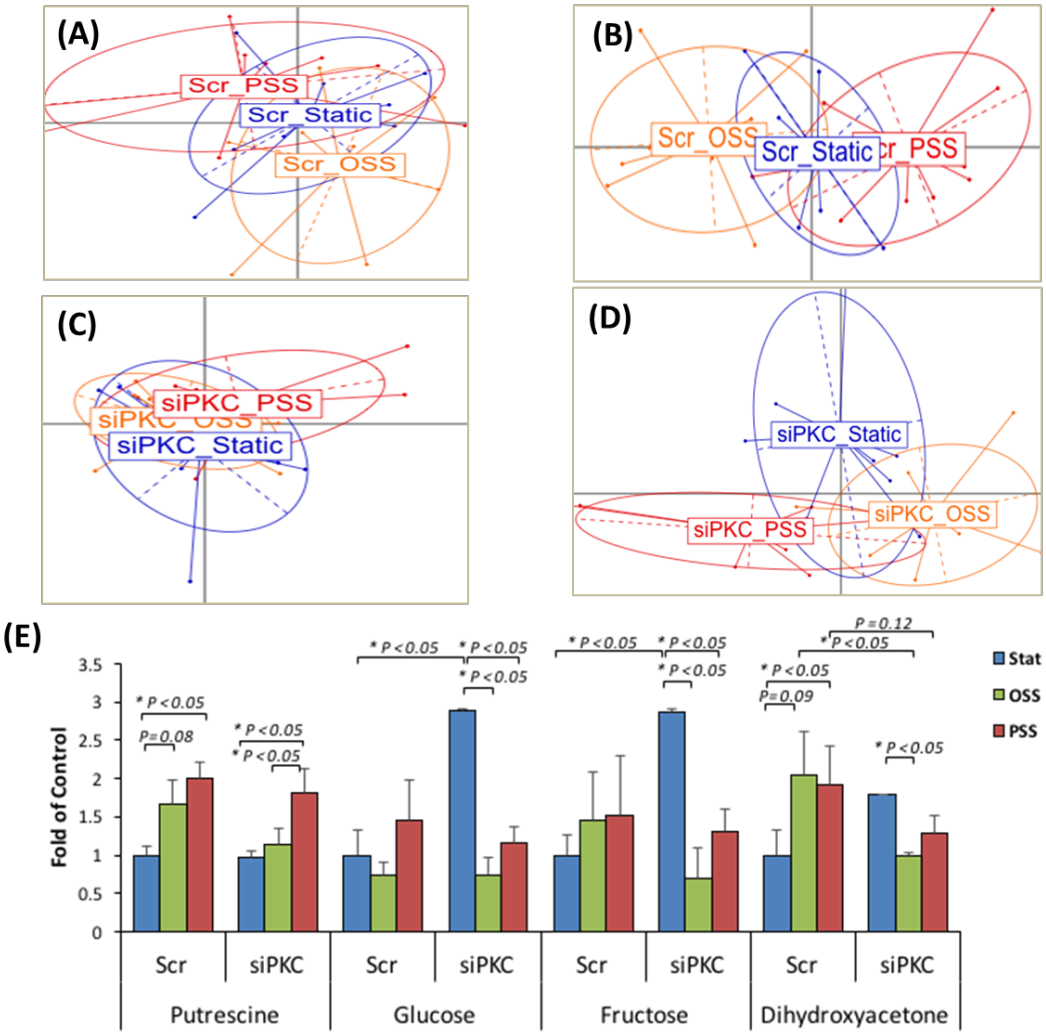


**Figure 2.** Shear Stress-mediated PKCε-dependent metabolites. HAEC were transfected with scramble siRNA (Scr) or PKCε siRNA (siPKC), followed by 3 conditions: 1) Static, 2) PSS, or 3) OSS for 4 hours. **(A, C)** Of the 136 known metabolites, PCA revealed significant overlapping of metabolites following the Static, OSS and PSS conditions in both Scr and siPKCε transfected HAEC. **(B, D)** 16 metabolites in Scr and 13 siPKCε groups underwent significant change in concentration following the 3 conditions (* $p < 0.05$, n=6). PCA further demonstrated a separation of metabolites that were statistically different. **(E)** PSS and OSS significantly modulated the selected metabolites, demonstrating PKCε-dependent Glucose, Frucose, Dihydroxyacetone, and PKCε-independent Putrescine (* $p < 0.05$, n=6).

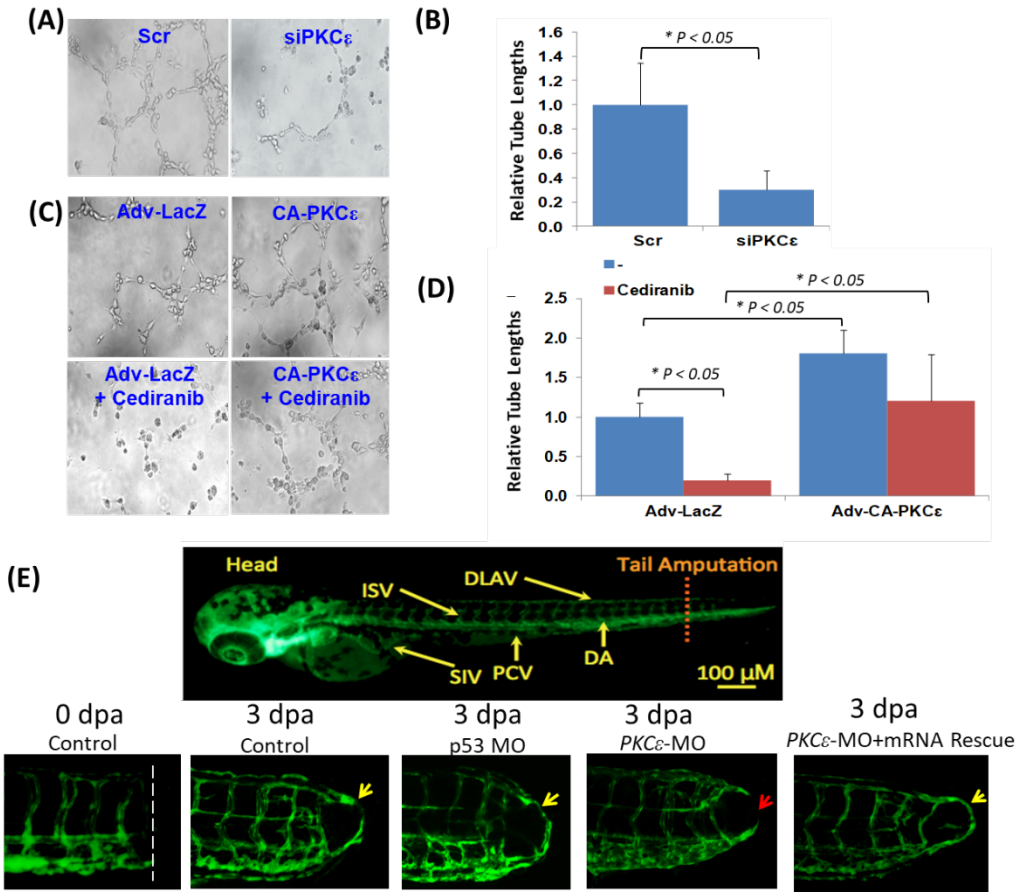


**Figure 3.** PKCε-mediated tube formation and vascular repair. **(A)** HAEC were transfected with scrambled siRNA (Scr) or PKCε siRNA (siPKCε), and **(B)** Silencing PKCε with siRNA attenuated tube formation. Tube formation was quantified by the measurement of relative tube length. **(C-D)** HAEC were infected with recombinant control LacZ or CA-PKCε adenoviruses. Treatment with Cediranib at 10 μM inhibited tube formation (* $p < 0.05$, n = 5), whereas CA-PKCε restored Cediranib-attenuated tube formation (* $p < 0.05$, n = 5). **(E)** *Tg(flk-1:EGFP)* embryos underwent tail amputation as a mode of vascular regeneration. The control group and *p53* MO-injected embryos exhibited vascular repair (yellow arrows) connecting DLAV with DA. *PKCε* MO injection impaired vascular repair (red arrow), whereas co-injecting *PKCε* mRNA restored impaired vascular repair (yellow arrow). SIV: subintestinal vessel; ISV: intersegmental vessel; PCV: posterior cardinal vein; DLAV: dorsal longitudinal anastomotic vessel); DA: Dorsal Aorta.

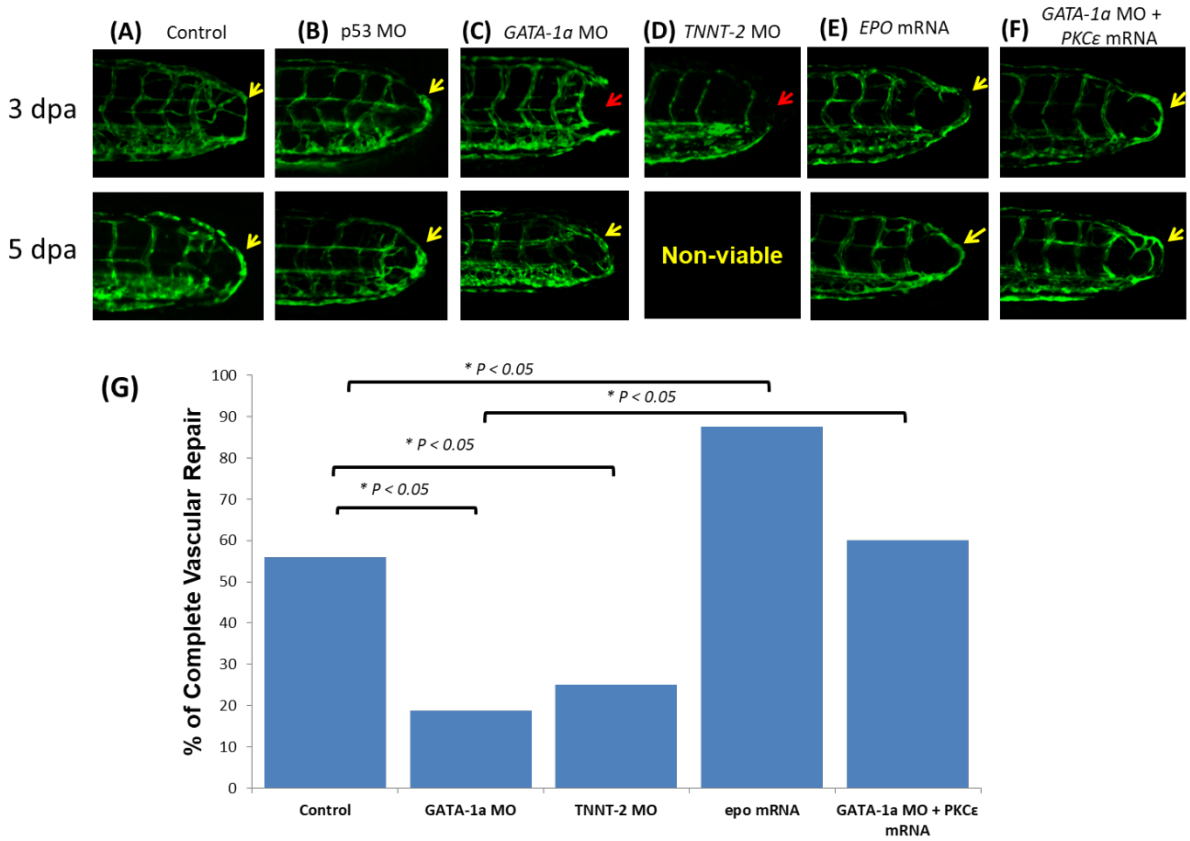


**Figure 4.** Shear stress-mediated vascular repair. **(A-B)** The control and *p53* MO-injected fish developed vascular repair at 3 dpa (yellow arrows). **(C)** *GATA-1a* MO delayed vascular repair at 3 dpa. **(D)** *TNNT-2* MO impaired vascular repair (red arrow) at 3 dpa (* $p < 0.05$, n = 5), and the embryos failed to thrive at 5 dpa. **(E)** *EPO* mRNA injection promoted vascular repair at 3 dpa. **(F)** Co-injection of *GATA-1a* MO with *PKCε* mRNA resulted in vascular repair. **(G)** Quantitative comparison revealed differential percentage of vascular repair (* $p < 0.05$, n = 30; n=5 for *TNNT-2* MO injected group)

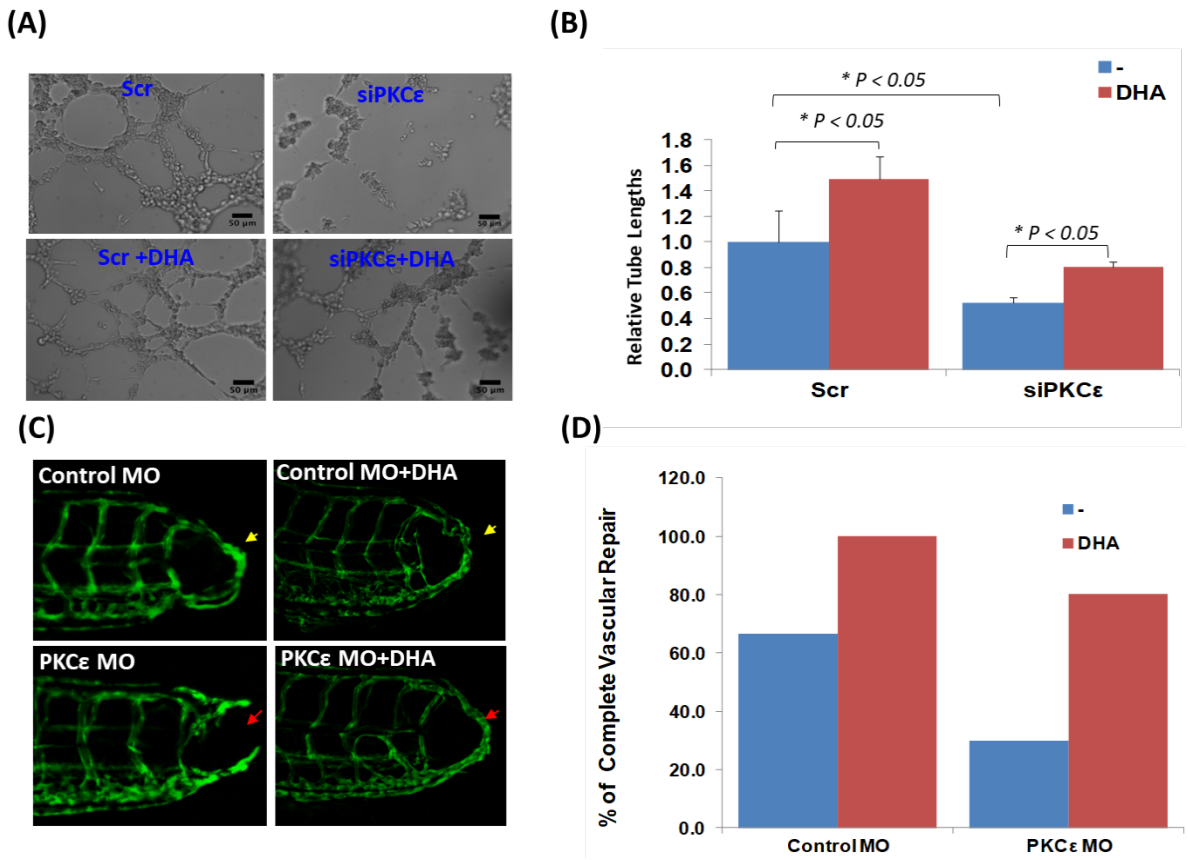


**Figure 5.** Glycolytic metabolite Dihydroxyacetone promoted vascular repair. **(A)** DHA promoted tube formation in HAEC transfected with scramble siRNA (Scr). siPKCε attenuated tube formation, which was rescued with dihydroxyacetone (DHA) at 1 mg/mL (* $p < 0.05$, n=4). **(C)** Transgenic *Tg (flk- 1:EGFP)* embryos injected with *p53* MO or *PKCε* MO underwent tail amputation, and were treated with or without DHA (1mg/mL) for 3 days. DHA treatment rescued impaired vascular repair following *PKCε* MO injection. **(D)** Vascular repair was quantified by the percentage of embryos that developed vascular regeneration (n=20)

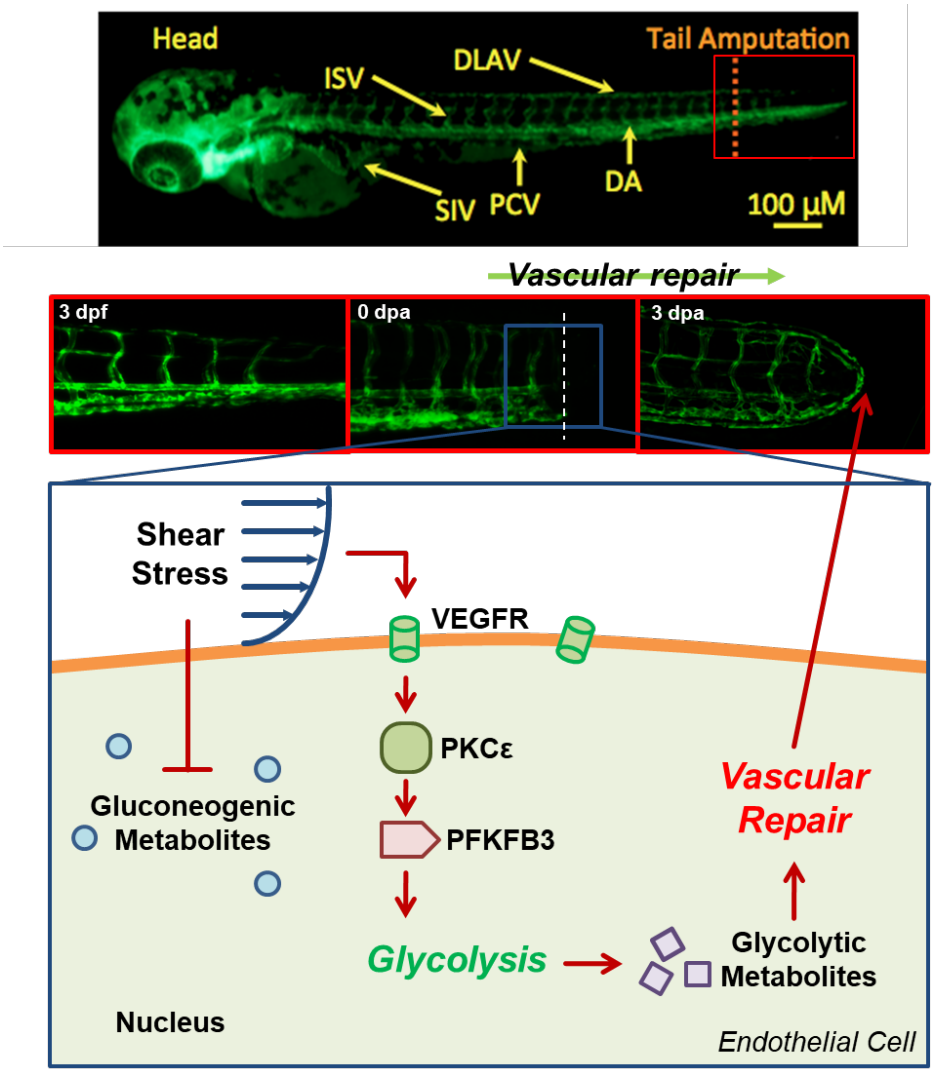


**Figure 6.** A schematic diagram to depict flow-sensitive VEGFR-PKCε-PFKFB3 modulation of glycolytic metabolites for vascular repair.

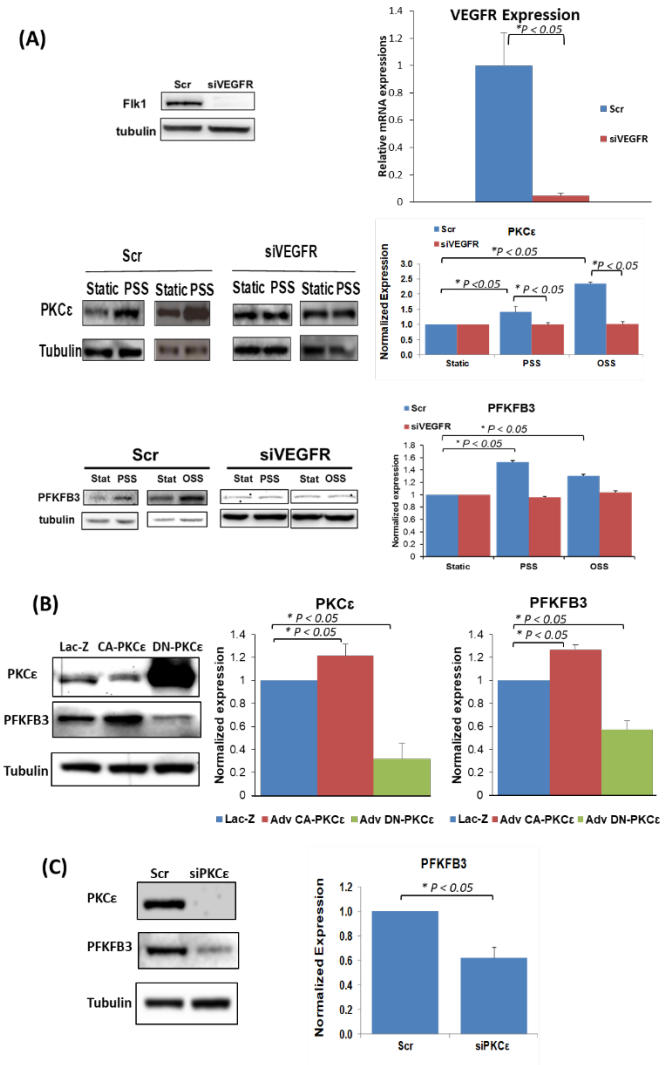


**Figure S1.** Shear stress induced VEGFR-dependent PKCε expression. HAEC were transfected with scrambled siRNA (Scr) or VEGFR2 siRNA (siVEGFR). The density quantification of Western blots was normalized to β-Tubulin. **(A)** PSS and OSS differentially increased VEGFR2-dependent PKCε protein expression (* $p < 0.05$, n=4). **(B)** HAEC were infected with recombinant Adenoviruses LacZ, CA-PKCε or DN-PKCε. CA-PKCε promoted, whereas DN-PKCε reduced PFKFB3 protein expression (* $p < 0.05$ vs. control, $n = 4$). **(C)** HAEC were transfected with scrambled siRNA (Scr) or siPKCε to assess PKCε-dependent PFKFB3 expression. siPKCε mitigated shear stress-induced PFKFB3 protein expression (* $p < 0.05$, $n = 3$).

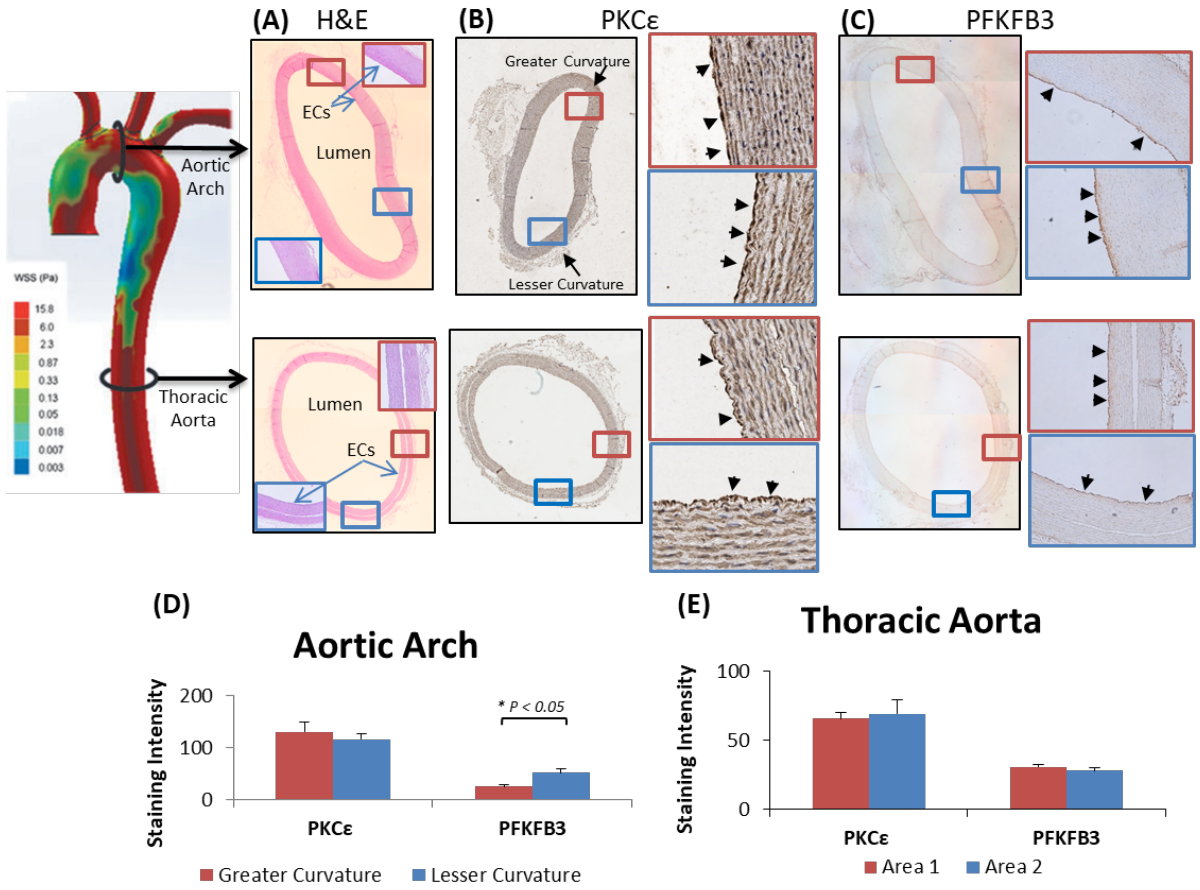


**Figure S2.** PKCε and PFKFB3 immunostaining. **(A)** Endothelial cells (EC) were stained with H&E in the cross-sections of NZW rabbit aortic arch and thoracic aorta. **(B)** PKCε and **(C)** PFKFB3 immunohistochemistry staining was prominent in EC lining. **(D)** In the aortic arch, PFKFB3 were differentially stained at lesser and greater curvatures (red vs. blue) (* $p < 0.01$, n = 3). **(E)** In the thoracic aorta, PKCε and PFKFB3 were equally stained.

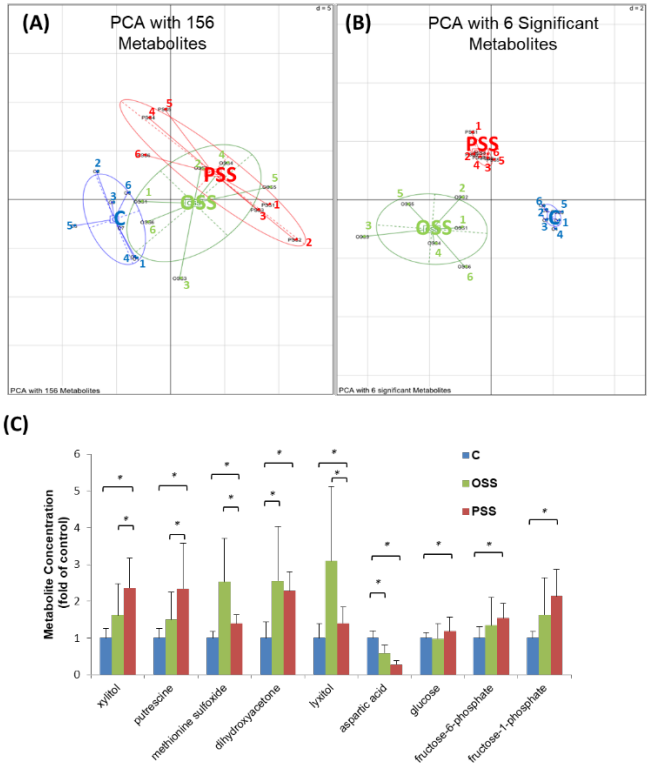


**Figure S3**. Endothelial metabolomic responses to shear stress. Metabolite samples were collected from human aortic endothelial cells (HAEC) exposed to either static condition (C), OSS, or PSS ($n$ = 6 per flow condition). **(A)** Principal component analysis (PCA) was performed on a host of measured metabolites, identifying metabolites which were significantly different among the three conditions. Of the 156 metabolites with known identity, PCA revealed a significant overlap among the three conditions. The individual samples are numerically indicated. **(B)** After identification of 6 statistically different metabolites in response to the three conditions, PCA revealed a distinct separation. **(C)** Selected metabolites were significantly modulated following PSS and OSS conditions ($p < 0.01$ vs. control, $n$ = 6), including an increase in glycolysis-related metabolite, dihydroxyacetone (DHA), but a decrease in gluconeogenic metabolite, aspartic acid.

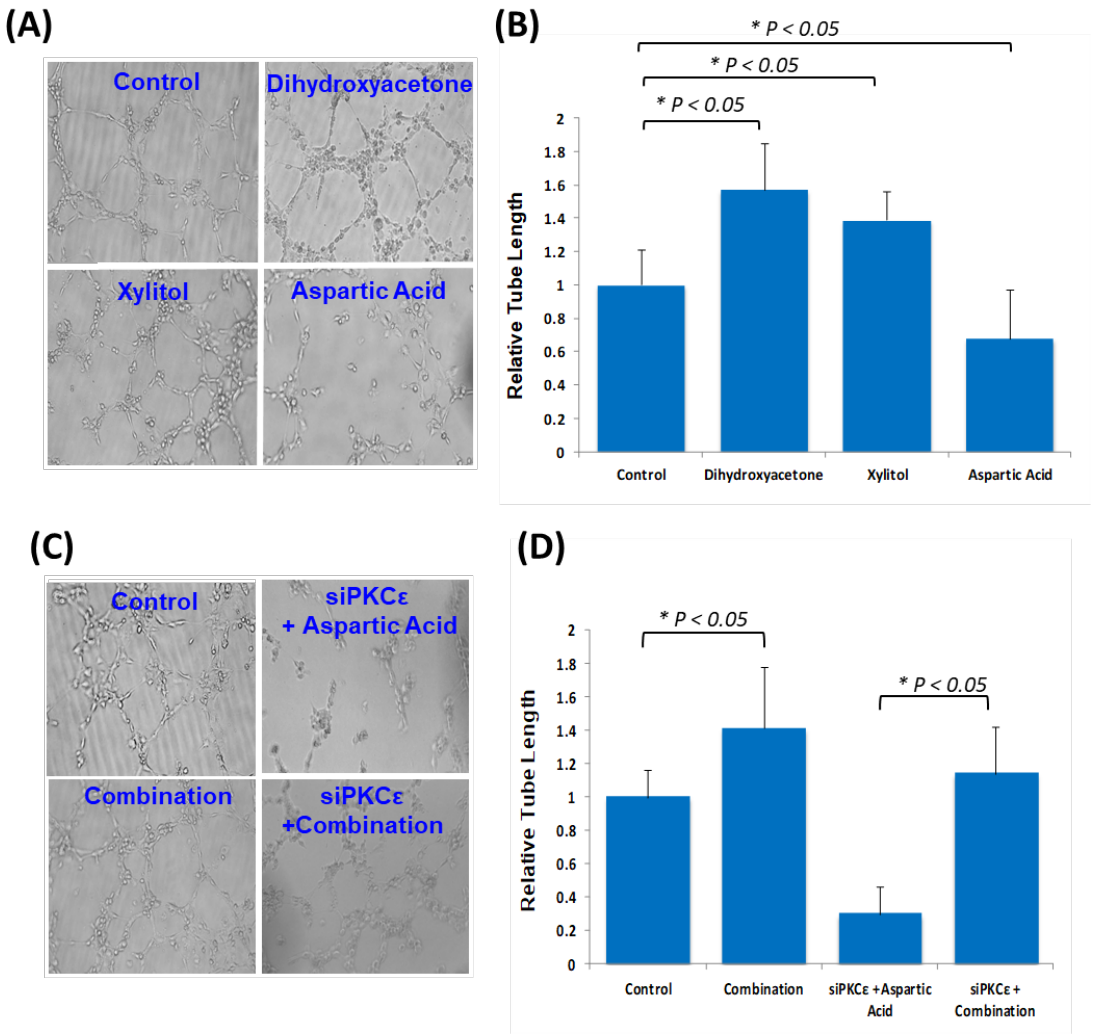


**Figure S4.** Glycolytic metabolites promoted tube formation. **(A-B)** Tube formation of HAEC treated with 1 mg/mL Dihydroxyacetone, 2 mg/mL Xylitol or 250 μg/mL aspartic acid in the presence of 25 μM $H_2O_2$. Dihydroxyacetone and Xylitol partially rescued $H_2O_2$ –attenuated tube formation whereas aspartic acid further inhibited tube formation (* $p < 0.05$ vs. control, n=4). **(C-D)** Under normoxic conditions, a combination of glycolytic metabolites, including glucose, fructose-6-phosphate, fructose-1-phosphate, dihydroxyacetone, and xylitol rescued tube formation in HAEC transfected with PKCε siRNA, whereas aspartic acid had no effect (* $p < 0.05$, $n = 4$).

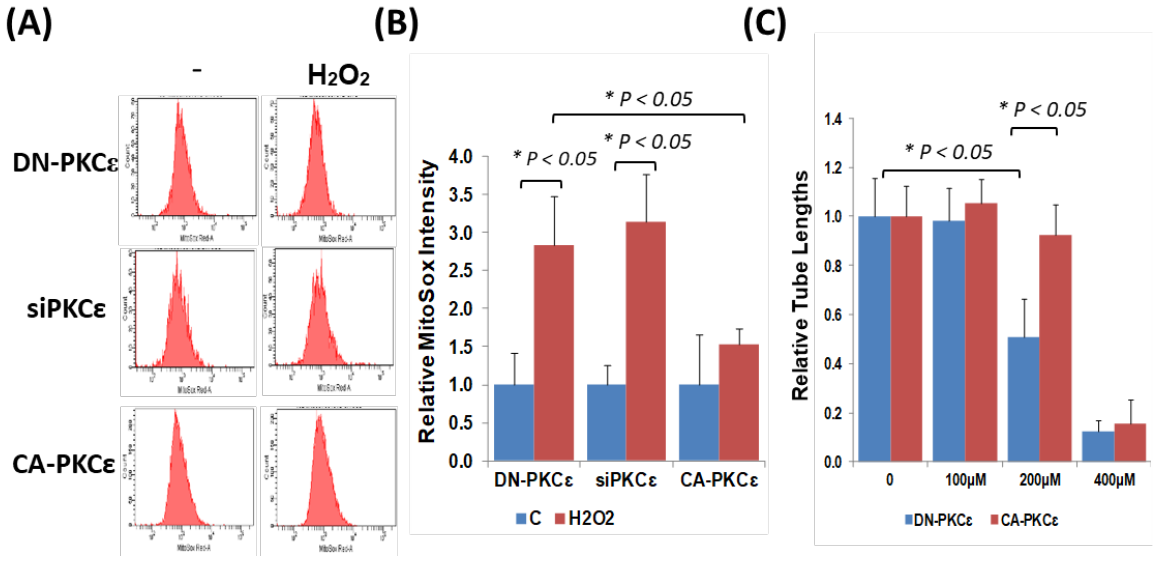


**Figure S5**. PKCε attenuation of mitochondrial super oxide ($O_2^{-}$) production. **(A-B)** CA-PKCε significantly attenuated $H_2O_2$-mediated endothelial mitoSOX intensity in response to $H_2O_2$ at 200 μM for 4 hours. **(C)** $H_2O_2$ at 200 μM significantly attenuated tube length, whereas over-expression of PKCε reversed the $H_2O_2$-mediated oxidative stress ($H_2O_2 + e^- \rightarrow {}^{\bullet}OH + HO^-$). Treatment with Adv PKCε significantly attenuated the mitoSOX intensity during tube formation (*$p < 0.01$, $n = 5$).

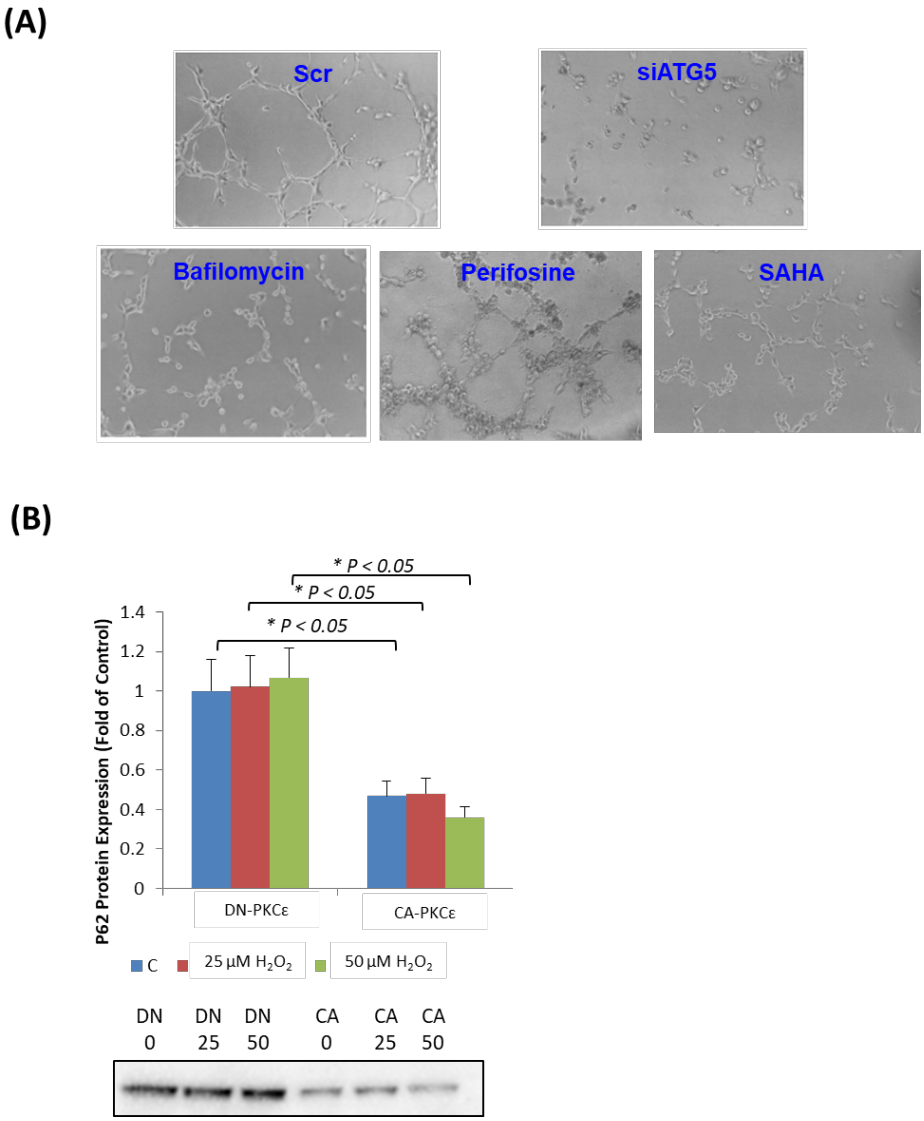


**Figure S6**. PKCε activation of autophagic flux to promote tube formation. **(A)** siATG5 and Bafilomycin inhibited HAEC tube formation, whereas autophagy activators, Perifosine and SAHA, rescued tube formation in the presence of $H_2O_2$. **(B)** DN-PKCε increased, whereas CA-PKCε decreased P62 protein levels to complete the autophagic flux.

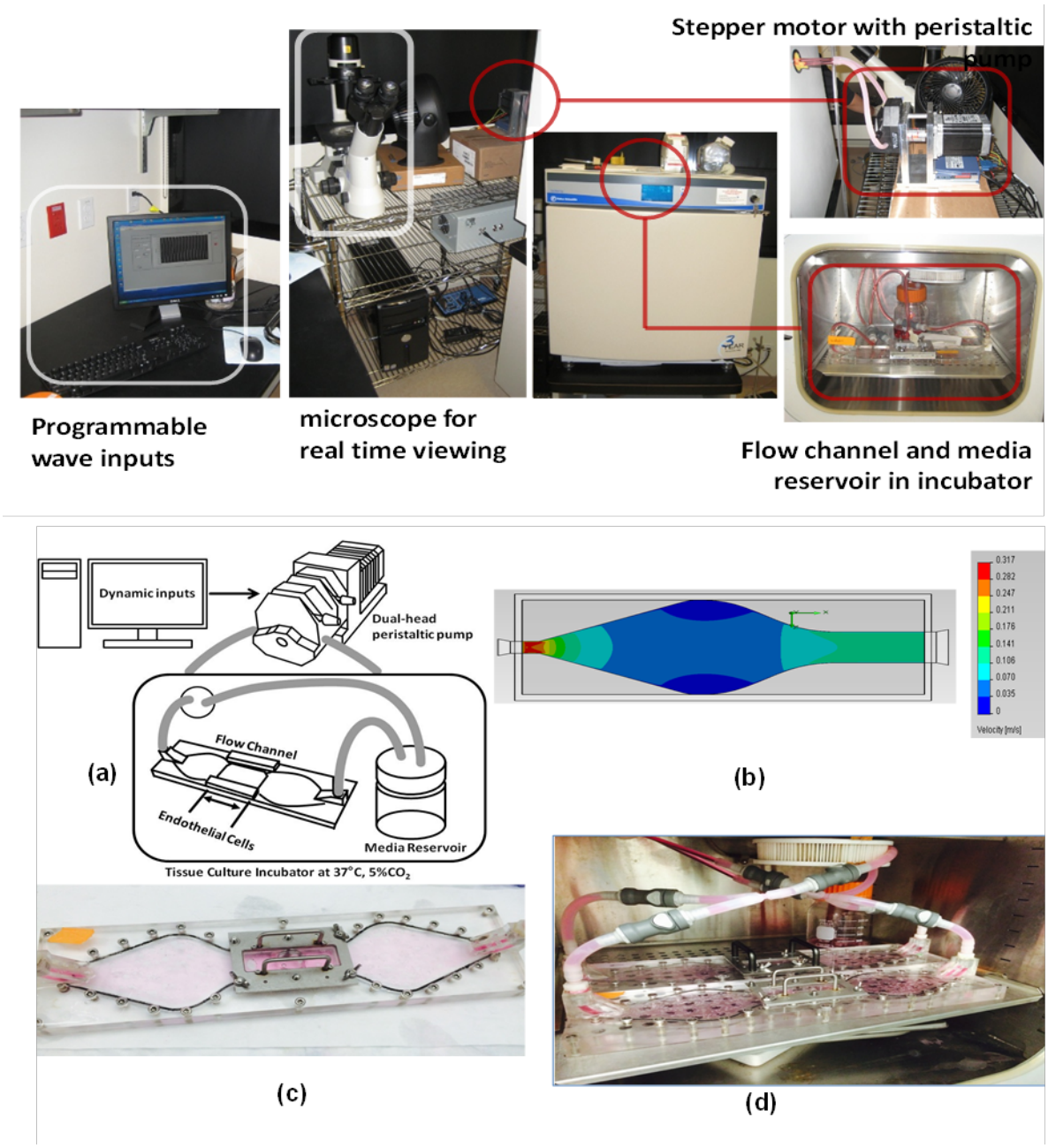


**Figure S7.** The dynamic flow system to simulate defined shear stress. The flow system was designed to simulate physiologic shear stress occurring at the arterial branching points with well-defined slew rates ($\partial\tau/\partial t$), time-averaged shear stress ($\tau_{ave}$), frequency (Hz), and amplitude. The endothelial cells were subjected to PSS or OSS in DMEM culture medium supplemented with 1% FBS at 37°C and pH = 7.4. Confluent monolayers of HAEC grown on glass slides were subjected to three flow conditions at 1 Hz for 4 hours: 1) control at static state, 2) PSS at $\tau_{ave}$ = 50 dyne·cm$^{-2}$

accompanied by $\partial\tau/\partial t$=71 dyne·cm$^{-2}$·s$^{-1}$ at 1 Hz, and 3) OSS at 0±3 dyne·cm$^{-2}$ with $\tau_{ave}$=0 dyne·cm$^{-2}$ at 1 Hz. For OSS condition, minimal forward flow at a mean shear stress of 0.2 dyne·cm$^{-2}$ was provided every hour to deliver nutrients and to remove waste products. The newly upgraded dynamic flow system optimizes our capability to simulate various arterial wave forms under a physiologic condition. The flow channel can be housed in the incubator to maintain at a constant pH and temperature. The Lab-View can be programmed to drive the peristaltic pump, capable of generating distinct flow wave forms at precise temporal gradients, pulse pressure, and frequency (cycle length). **(a)** A schematic diagram of the dynamic flow system highlights the flow loop system. **(b)** Computational fluid dynamics simulated the steady flow profile. **(c)** A photo of the parallel flow channel with the symmetric diffuser and contraction to ensure well-developed flow profiles. **(d)** The channel was placed in the incubator for maintain temperature (37.5°), pH (7), and 5% $CO_2$ control.

## [Supplemental Videos Available Online]

**Videos S1.** Blood flow in zebrafish embryos injected with control p53 MO. Micro-injection with the control p53 MO displayed a normal blood circulation in the DA, PCV, and SIV in Tg(GATA-1a:dsRed) transgenic embryos at 3 dpa. DA, dorsal aorta; dpa, days post-amputation; MO, morpholino oligonucleotide; PCV, posterior cardinal vein; SIV, subintestinal vein.

**Videos S2.** Blood flow in zebrafish embryos injected with EPO mRNA. Micro-injection with EPO mRNA significantly augmented erythrocytosis and blood viscosity in Tg (GATA-1a:dsRed) embryos at 3 dpa. EPO, erythropoietin; mRNA, messenger RNA.

**Videos S3.** Blood flow in zebrafish embryos injected with GATA-1a MO. Micro-injection with GATA-1a MO inhibited hematopoiesis in Tg(GATA-1a:dsRed) embryos at 3 dpa.

## Table 4.1: HAEC metabolites with Known Identity

| BinBase Name | C Avg | C S.D. | OSS Avg | OSS S.D. | PSS Avg | PSS S.D. |
|---|---|---|---|---|---|---|
| xylose | 195.14 | 36.04 | 187.43 | 167.72 | 305.82 | 219.30 |
| xylitol | 396.14 | 100.48 | 641.93 | 338.10 | 933.59 | 321.52 |
| valine | 349776.57 | 102046.36 | 326389.62 | 143718.80 | 297057.54 | 73409.29 |
| uridine-5'-monophosphate | 5330.14 | 1275.90 | 5665.70 | 3147.41 | 6438.20 | 1567.50 |
| uridine | 224.86 | 81.79 | 316.83 | 136.72 | 253.39 | 112.43 |
| urea | 5660.43 | 2239.72 | 6073.53 | 2242.12 | 7360.02 | 2865.12 |
| uracil | 274.14 | 40.68 | 284.24 | 117.78 | 256.54 | 128.92 |
| UDP-N-acetylglucosamine | 2157.14 | 277.14 | 2033.88 | 857.37 | 1873.05 | 592.59 |
| UDP-glucuronic acid | 1388.00 | 500.58 | 1006.94 | 357.17 | 2426.17 | 1636.34 |
| tyrosine | 416579.57 | 16773.98 | 335602.57 | 142167.74 | 390769.82 | 113907.33 |
| tryptophan | 89414.14 | 4102.61 | 76565.80 | 32374.88 | 85346.41 | 23731.14 |
| threonine | 347861.86 | 24602.15 | 293298.45 | 123973.93 | 310772.85 | 86478.50 |
| threonic acid | 205.00 | 31.27 | 240.90 | 127.02 | 269.15 | 157.79 |
| taurine | 6828.00 | 3022.15 | 5477.31 | 2986.27 | 5277.75 | 2541.01 |
| tartaric acid | 232.00 | 102.53 | 278.79 | 153.40 | 262.20 | 120.32 |
| sucrose | 11271.14 | 1902.00 | 10717.14 | 4078.89 | 13248.84 | 5471.02 |
| succinic acid | 1366.71 | 255.60 | 1175.37 | 479.39 | 1425.34 | 498.45 |
| stearic acid | 335072.86 | 85012.89 | 344570.70 | 142888.66 | 360493.09 | 107482.75 |
| spermine | 706.29 | 163.93 | 723.28 | 298.20 | 677.03 | 327.55 |
| spermidine | 2473.29 | 1192.65 | 2409.95 | 1372.11 | 3247.73 | 1647.77 |
| sorbitol | 22323.00 | 4548.03 | 19317.72 | 8513.58 | 18297.51 | 6093.80 |
| shikimic acid | 622.43 | 116.12 | 1012.59 | 1052.19 | 1472.17 | 1819.50 |
| serine | 277966.86 | 30100.99 | 220366.71 | 91555.56 | 224051.22 | 61585.12 |
| sebacic acid, di(2-octyl) ester NIST | 1802.14 | 158.11 | 1987.02 | 894.77 | 2061.97 | 529.77 |

| | | | | | | |
|---|---|---|---|---|---|---|
| saccharic acid | 625.71 | 278.68 | 748.67 | 221.88 | 917.84 | 412.10 |
| ribulose-5-phosphate | 652.43 | 115.76 | 814.25 | 454.38 | 692.20 | 285.74 |
| ribose-5-phosphate | 818.14 | 246.75 | 1042.11 | 441.94 | 1147.13 | 560.02 |
| ribitol | 2922.00 | 602.37 | 2652.91 | 1048.47 | 2227.21 | 730.43 |
| raffinose | 1807.86 | 338.91 | 1747.27 | 635.60 | 2233.09 | 979.78 |
| quinic acid | 183.86 | 35.38 | 432.20 | 539.02 | 641.72 | 918.45 |
| pyruvic acid | 1463.57 | 389.44 | 1612.21 | 602.81 | 1583.83 | 473.40 |
| pyrophosphate | 232980.00 | 51158.25 | 206532.75 | 93659.15 | 240529.16 | 82791.66 |
| putrescine | 6412.57 | 1607.79 | 9675.40 | 4721.94 | 14986.99 | 7925.49 |
| propane-1,3-diol NIST | 2506.29 | 340.91 | 2773.99 | 1363.74 | 3028.39 | 753.48 |
| proline | 52963.57 | 32087.01 | 54872.86 | 44021.84 | 44120.41 | 17633.47 |
| pinitol | 1881.29 | 308.06 | 1788.87 | 669.95 | 1962.14 | 758.25 |
| phosphogluconic acid | 1304.57 | 292.36 | 1475.62 | 655.76 | 1482.11 | 452.35 |
| phosphoethanolamine | 7566.57 | 2771.65 | 5471.38 | 3269.84 | 9578.83 | 7266.90 |
| phosphoenolpyruvate | 1941.43 | 948.03 | 2427.00 | 860.19 | 3197.31 | 1623.72 |
| phosphate | 86453.43 | 13041.84 | 72021.55 | 29910.34 | 89760.76 | 32618.22 |
| phenylalanine | 176729.14 | 11387.20 | 147453.03 | 61008.55 | 169209.94 | 48289.44 |
| pelargonic acid | 15821.00 | 1540.21 | 16265.46 | 7328.81 | 17183.54 | 6091.66 |
| pantothenic acid | 5288.43 | 531.77 | 4898.82 | 2040.17 | 5101.60 | 1426.61 |
| palmitic acid | 42201.00 | 8246.69 | 41954.38 | 16817.68 | 43654.95 | 12676.91 |
| oxoproline | 1069816.86 | 67975.65 | 897070.24 | 378695.94 | 947540.56 | 259352.95 |
| oxalic acid | 259.57 | 139.14 | 645.16 | 424.29 | 647.18 | 394.41 |
| ornithine | 6535.00 | 1054.32 | 5598.76 | 3088.11 | 7467.59 | 3076.01 |
| oleic acid | 719.29 | 174.96 | 831.99 | 333.23 | 1029.18 | 524.71 |
| oleamide NIST | 408.00 | 121.21 | 450.89 | 214.76 | 423.11 | 212.41 |
| octanol NIST | 1724.00 | 274.97 | 1887.57 | 891.09 | 2118.30 | 577.99 |
| octadecanol | 243.86 | 60.89 | 702.56 | 586.83 | 688.83 | 213.05 |

| | | | | | | |
|---|---|---|---|---|---|---|
| nicotinamide | 4696.43 | 658.29 | 4829.61 | 2112.11 | 5284.44 | 1617.03 |
| N-acetylmannosamine | 337.00 | 115.42 | 365.49 | 157.46 | 394.78 | 138.27 |
| N-acetylglutamate | 721.00 | 341.17 | 749.31 | 391.40 | 705.91 | 174.01 |
| N-acetylaspartic acid | 1858.14 | 231.59 | 1768.23 | 747.13 | 1780.30 | 602.50 |
| myristic acid | 14882.43 | 2302.09 | 16358.58 | 6909.56 | 15688.94 | 4109.25 |
| myo-inositol | 36604.57 | 12604.67 | 31388.38 | 12188.10 | 51012.44 | 20908.16 |
| monomyristin | 14532.71 | 1402.20 | 15644.89 | 6901.16 | 16280.31 | 4224.87 |
| methionine sulfoxide | 8813.43 | 1545.49 | 22289.21 | 10385.22 | 12237.17 | 2112.82 |
| methionine | 42760.57 | 14335.06 | 31283.29 | 14335.40 | 26470.34 | 5545.71 |
| methanolphosphate | 3081.29 | 782.27 | 2854.75 | 1924.43 | 3731.63 | 1025.95 |
| mannose | 712.43 | 557.94 | 971.28 | 647.62 | 1280.09 | 669.95 |
| maltose | 635.14 | 120.04 | 507.86 | 232.12 | 427.45 | 208.43 |
| malonic acid | 228.00 | 107.00 | 277.14 | 137.86 | 247.12 | 91.65 |
| malic acid | 2099.86 | 300.08 | 2080.58 | 869.00 | 1459.14 | 796.06 |
| maleimide | 1664.43 | 151.44 | 1934.49 | 945.91 | 2033.84 | 924.56 |
| lyxitol | 1242.00 | 479.92 | 3840.13 | 2508.07 | 1739.44 | 543.48 |
| lysine | 278726.43 | 56743.55 | 201610.08 | 71881.80 | 268909.97 | 115700.76 |
| linoleic acid | 269.43 | 54.82 | 329.40 | 139.26 | 340.75 | 142.44 |
| levoglucosan | 1044.29 | 300.44 | 1024.92 | 434.50 | 1081.21 | 512.74 |
| leucine | 311474.14 | 139806.07 | 294745.87 | 170006.88 | 236228.27 | 40171.56 |
| lauric acid | 14287.71 | 2772.07 | 19281.30 | 10941.62 | 17948.23 | 6662.38 |
| lactic acid | 54847.71 | 13704.94 | 51370.28 | 18581.77 | 59919.97 | 26476.69 |
| isothreonic acid | 589.29 | 144.19 | 680.46 | 272.08 | 679.87 | 291.81 |
| isoleucine | 531613.57 | 35778.49 | 468455.07 | 193197.82 | 535087.69 | 153665.44 |
| isocitric acid | 459.29 | 35.45 | 429.35 | 222.68 | 417.67 | 155.30 |
| inosine-5'-monophosphate | 630.71 | 389.79 | 1263.54 | 1311.90 | 616.84 | 394.72 |
| inosine | 592.86 | 240.84 | 1065.69 | 682.55 | 1148.22 | 856.67 |

| | | | | | | |
|---|---|---|---|---|---|---|
| hypoxanthine | 1520.29 | 508.98 | 1543.71 | 748.92 | 1248.70 | 888.47 |
| hydroxylamine | 34416.00 | 9613.31 | 31136.33 | 16401.23 | 37144.46 | 16691.65 |
| hydroxycarbamate NIST | 8053.57 | 3254.11 | 6369.44 | 3044.60 | 7237.80 | 3943.33 |
| histidine | 90230.57 | 3677.25 | 63495.04 | 28281.37 | 77347.91 | 22777.38 |
| hexose NIST | 984283.71 | 160264.47 | 690577.07 | 465138.07 | 557152.87 | 300956.11 |
| hexitol | 1841.71 | 938.06 | 1609.58 | 1044.02 | 1679.57 | 566.79 |
| hexadecylglycerol NIST | 484.00 | 111.96 | 538.99 | 233.02 | 393.57 | 87.23 |
| heptadecanoic acid | 3689.14 | 735.55 | 3876.08 | 1546.93 | 3954.56 | 1137.63 |
| guanosine | 245.29 | 72.81 | 287.54 | 191.86 | 276.69 | 69.72 |
| guanine | 255.14 | 40.19 | 325.88 | 173.76 | 338.68 | 134.57 |
| glycolic acid | 2952.71 | 828.81 | 2322.97 | 1274.66 | 3225.81 | 1329.84 |
| glycine | 178203.57 | 48321.11 | 172535.73 | 68577.76 | 161239.97 | 53663.30 |
| glycerol-alpha-phosphate | 69722.29 | 12795.43 | 52967.92 | 19251.50 | 54742.93 | 21056.87 |
| glycerol-3-galactoside | 1031.00 | 388.37 | 1905.77 | 1474.33 | 2635.62 | 2832.62 |
| glycerol | 31933.29 | 6105.71 | 38100.96 | 22330.15 | 52444.74 | 28812.61 |
| glyceric acid | 474.57 | 63.68 | 466.81 | 364.57 | 728.80 | 763.50 |
| glutamine | 1165560.86 | 92804.23 | 869889.60 | 423071.39 | 989545.48 | 257709.52 |
| glutamic acid | 510605.00 | 136130.26 | 389296.18 | 136342.47 | 363218.21 | 164608.73 |
| glucose-6-phosphate | 587.14 | 388.06 | 904.01 | 343.22 | 996.89 | 465.80 |
| glucose-1-phosphate | 3006.57 | 599.56 | 3833.37 | 1976.70 | 4135.53 | 1720.62 |
| glucose | 642227.43 | 97475.58 | 628368.37 | 266201.40 | 757936.06 | 243237.74 |
| gluconic acid | 299.57 | 105.62 | 560.52 | 262.81 | 1171.12 | 1346.16 |
| galactose-6-phosphate | 131.29 | 57.90 | 175.99 | 85.96 | 210.28 | 70.45 |
| galactinol | 461.00 | 75.88 | 488.27 | 330.02 | 584.57 | 252.43 |
| fumaric acid | 1809.57 | 446.17 | 1688.31 | 645.15 | 1461.45 | 768.08 |
| fructose-6-phosphate | 369.57 | 113.98 | 498.00 | 280.42 | 568.35 | 150.49 |
| fructose-1-phosphate | 369.57 | 63.08 | 602.87 | 370.50 | 791.50 | 267.72 |

| | | | | | | |
|---|---|---|---|---|---|---|
| fructose-1,6-bisphosphate | 711.86 | 392.63 | 2297.95 | 1345.92 | 2743.85 | 1972.25 |
| fructose | 10546.29 | 3148.16 | 11573.02 | 6922.33 | 15797.90 | 9805.66 |
| ethanolamine | 3702.14 | 1099.68 | 4717.38 | 3010.44 | 5123.06 | 3222.00 |
| erythrose | 284.29 | 29.44 | 423.49 | 204.64 | 293.52 | 57.33 |
| erythritol | 1490.71 | 312.72 | 1403.39 | 501.17 | 1455.60 | 593.81 |
| dihydroxyacetone | 1038.14 | 449.40 | 2649.49 | 1536.32 | 2373.05 | 536.03 |
| diglycerol | 47563.71 | 27192.02 | 43965.00 | 22042.58 | 59390.23 | 20828.61 |
| cytidine-5-monophosphate | 829.14 | 473.64 | 834.52 | 305.10 | 945.30 | 407.50 |
| cystine | 8230.57 | 4835.66 | 8343.81 | 4219.16 | 12172.45 | 6036.03 |
| cysteine-glycine | 915.71 | 257.52 | 626.36 | 259.71 | 718.10 | 270.66 |
| cysteine | 34834.00 | 10896.49 | 33427.50 | 22913.64 | 26349.66 | 3933.75 |
| creatinine | 4671.00 | 3468.29 | 4251.47 | 1618.16 | 7136.88 | 5408.56 |
| conduritol-beta-epoxide | 717.86 | 74.04 | 700.72 | 292.83 | 853.83 | 298.35 |
| citrulline | 1719.43 | 422.78 | 1326.97 | 424.40 | 1497.63 | 552.73 |
| citric acid | 19679.29 | 2984.24 | 18653.46 | 9624.64 | 21401.81 | 8164.34 |
| cholesterol | 317029.71 | 72050.67 | 363881.10 | 142955.42 | 326404.20 | 123625.92 |
| cholestan-3-ol | 516.86 | 89.57 | 391.94 | 212.40 | 502.06 | 161.93 |
| cellobiose | 298894.86 | 36881.31 | 349225.33 | 156847.17 | 313043.02 | 96839.08 |
| caprylic acid | 2879.14 | 326.30 | 2735.90 | 1213.29 | 3430.18 | 1089.62 |
| capric acid | 869.57 | 101.34 | 966.62 | 504.74 | 1128.11 | 464.01 |
| bisphosphoglycerol NIST | 480.86 | 68.76 | 453.54 | 224.77 | 486.40 | 158.49 |
| beta-sitosterol | 568.57 | 95.60 | 513.94 | 201.61 | 528.23 | 212.49 |
| beta-glycerolphosphate | 606.14 | 68.48 | 547.93 | 258.31 | 433.33 | 209.52 |
| beta-alanine | 1147.43 | 393.58 | 1632.37 | 1205.73 | 1493.68 | 549.32 |
| benzoic acid | 7910.71 | 425.40 | 8043.77 | 3763.78 | 8420.25 | 2124.10 |
| behenic acid | 2344.43 | 617.10 | 2931.16 | 1102.19 | 2915.31 | 1386.87 |
| azelaic acid | 243.71 | 76.23 | 380.89 | 260.19 | 493.88 | 131.07 |

| | | | | | | |
|---|---|---|---|---|---|---|
| aspartic acid | 83390.14 | 16388.72 | 48884.53 | 18569.96 | 23706.85 | 8795.95 |
| asparagine | 2714.71 | 1110.00 | 3494.29 | 1732.27 | 2610.61 | 1744.78 |
| arachidonic acid | 846.86 | 373.99 | 989.00 | 349.23 | 1238.89 | 449.74 |
| arachidic acid | 4393.57 | 1050.46 | 4788.64 | 2029.63 | 4975.95 | 1456.47 |
| arabitol | 1178.00 | 233.18 | 1141.31 | 579.56 | 1131.79 | 436.89 |
| aminomalonate | 8994.71 | 1876.73 | 5667.82 | 3198.18 | 5594.60 | 1679.00 |
| alpha-ketoglutarate | 304.71 | 62.95 | 406.99 | 191.33 | 355.05 | 116.00 |
| alanine | 28897.14 | 14177.64 | 32256.38 | 17027.90 | 20829.13 | 11100.73 |
| adipic acid | 497.00 | 142.23 | 709.03 | 363.20 | 784.46 | 288.15 |
| adenosine-5-monophosphate | 31055.14 | 5676.30 | 30984.90 | 12525.09 | 34975.73 | 15696.92 |
| adenosine | 1537.86 | 298.35 | 1456.62 | 666.35 | 2046.34 | 1175.71 |
| adenine | 1533.14 | 318.13 | 1567.30 | 827.86 | 1865.98 | 685.39 |
| aconitic acid | 230.14 | 41.17 | 255.45 | 116.72 | 328.82 | 149.62 |
| 5'-deoxy-5'-methylthioadenosine | 652.86 | 116.55 | 711.36 | 316.59 | 646.08 | 219.12 |
| 5-aminovaleric acid | 4120.57 | 1006.29 | 4164.90 | 2362.80 | 2808.83 | 585.97 |
| 3-phosphoglycerate | 1912.86 | 655.35 | 3541.05 | 1658.28 | 3058.75 | 1676.93 |
| 2-monostearin NIST | 122800.43 | 25421.51 | 166637.64 | 124174.70 | 175599.67 | 53124.87 |
| 2-monopalmitin | 65249.71 | 9939.73 | 84795.25 | 47987.51 | 85630.22 | 21934.05 |
| 2-hydroxyglutaric acid | 188.00 | 104.87 | 206.98 | 79.07 | 245.72 | 161.36 |
| 2,3-dihydroxypyridine | 213.00 | 33.68 | 163.24 | 105.60 | 210.66 | 98.06 |
| 1-monopalmitin | 171927.86 | 47506.48 | 234451.93 | 121254.23 | 248447.75 | 68646.52 |
| 1-monoolein | 939.71 | 417.48 | 1294.64 | 567.91 | 1198.27 | 440.78 |
| 1-monoheptadecanoyl glyceride NIST | 14431.43 | 1283.12 | 15396.02 | 6878.65 | 15641.66 | 3897.57 |
| 2,5-dihydroxypyrazine NIST | 15037.43 | 2714.31 | 12167.47 | 4950.58 | 12389.23 | 4927.23 |

## References


1. Frangos JA, McIntire LV, Eskin SG. Shear stress induced stimulation of mammalian cell metabolism. *Biotechnology and bioengineering*. 1988;32:1053-1060
2. Chiu JJ, Wang DL, Chien S, Skalak R, Usami S. Effects of disturbed flow on endothelial cells. *Journal of biomechanical engineering*. 1998;120:2-8
3. Hwang J, Ing MH, Salazar A, Lassegue B, Griendling K, Navab M, Sevanian A, Hsiai TK. Pulsatile versus oscillatory shear stress regulates nadph oxidase subunit expression: Implication for native ldl oxidation. *Circ Res*. 2003;93:1225-1232
4. Morbiducci U, Kok AM, Kwak BR, Stone PH, Steinman DA, Wentzel JJ. Atherosclerosis at arterial bifurcations: Evidence for the role of haemodynamics and geometry. *Thromb Haemost*. 2016;115:484-492
5. Dunn J, Qiu H, Kim S, Jjingo D, Hoffman R, Kim CW, Jang I, Son DJ, Kim D, Pan C, Fan Y, Jordan IK, Jo H. Flow-dependent epigenetic DNA methylation regulates endothelial gene expression and atherosclerosis. *The Journal of clinical investigation*. 2014;124:3187-3199
6. Parkinson disease: Metablomics study reveals novel biomarkers for pd. *Nat Rev Neurol*. 2013;9:484-484
7. Stroke: Molecular markers could help predict stroke risk after tia. *Nat Rev Neurol*. 2015;11:3-3
8. Clyne M. Kidney cancer: Metabolomics for targeted therapy. *Nat Rev Urol*. 2012;9:355-355
9. Kluge MA, Fetterman JL, Vita JA. Mitochondria and endothelial function. *Circ Res*. 2013;112:1171-1188

10. Sun X, Feinberg MW. Regulation of endothelial cell metabolism: Just go with the flow. *Arteriosclerosis, thrombosis, and vascular biology*. 2015;35:13-15

11. Wang Y, Zang QS, Liu Z, Wu Q, Maass D, Dulan G, Shaul PW, Melito L, Frantz DE, Kilgore JA, Williams NS, Terada LS, Nwariaku FE. Regulation of vegf-induced endothelial cell migration by mitochondrial reactive oxygen species. *American journal of physiology. Cell physiology*. 2011;301:C695-704

12. De Bock K, Georgiadou M, Carmeliet P. Role of endothelial cell metabolism in vessel sprouting. *Cell Metab*. 2013;18:634-647

13. Neufer PD, Bamman MM, Muoio DM, Bouchard C, Cooper DM, Goodpaster BH, Booth FW, Kohrt WM, Gerszten RE, Mattson MP, Hepple RT, Kraus WE, Reid MB, Bodine SC, Jakicic JM, Fleg JL, Williams JP, Joseph L, Evans M, Maruvada P, Rodgers M, Roary M, Boyce AT, Drugan JK, Koenig JI, Ingraham RH, Krotoski D, Garcia-Cazarin M, McGowan JA, Laughlin MR. Understanding the cellular and molecular mechanisms of physical activity-induced health benefits. *Cell Metab*. 2015;22:4-11

14. Li R, Beebe T, Jen N, Yu F, Takabe W, Harrison M, Cao H, Lee J, Yang H, Han P, Wang K, Shimizu H, Chen J, Lien CL, Chi NC, Hsiai TK. Shear stress-activated wnt-angiopoietin-2 signaling recapitulates vascular repair in zebrafish embryos. *Arteriosclerosis, thrombosis, and vascular biology*. 2014;34:2268-2275

15. Dejana E. The role of wnt signaling in physiological and pathological angiogenesis. *Circulation research*. 2010;107:943-952

16. Boselli F, Freund JB, Vermot J. Blood flow mechanics in cardiovascular development. *Cellular and molecular life sciences : CMLS*. 2015;72:2545-2559

17. Roman BL, Pekkan K. Mechanotransduction in embryonic vascular development. *Biomechanics and modeling in mechanobiology*. 2012;11:1149-1168

18. Boo YC, Sorescu G, Boyd N, Shiojima I, Walsh K, Du J, Jo H. Shear stress stimulates phosphorylation of endothelial nitric-oxide synthase at ser1179 by akt-independent mechanisms: Role of protein kinase a. *The Journal of biological chemistry*. 2002;277:3388-3396

19. Wang Y, Ashraf M. Role of protein kinase c in mitochondrial katp channel-mediated protection against ca2+ overload injury in rat myocardium. *Circulation research*. 1999;84:1156-1165

20. Bakker JL, Meijers-Heijboer H, Verheul H. Novel strategies towards the use of anti-angiogenic agents in breast cancer. *European journal of pharmacology*. 2013;717:36-39

21. Prokopiou EM, Ryder SA, Walsh JJ. Tumour vasculature targeting agents in hybrid/conjugate drugs. *Angiogenesis*. 2013;16:503-524

22. Suarez J, Rubio R. Regulation of glycolytic flux by coronary flow in guinea pig heart. Role of vascular endothelial cell glycocalyx. *The American journal of physiology*. 1991;261:H1994-2000

23. Culic O, Gruwel ML, Schrader J. Energy turnover of vascular endothelial cells. *The American journal of physiology*. 1997;273:C205-213

24. De Bock K, Georgiadou M, Schoors S, Kuchnio A, Wong BW, Cantelmo AR, Quaegebeur A, Ghesquiere B, Cauwenberghs S, Eelen G, Phng LK, Betz I, Tembuyser B, Brepoels K, Welti J, Geudens I, Segura I, Cruys B, Bifari F, Decimo I, Blanco R, Wyns S, Vangindertael J, Rocha S, Collins RT, Munck S, Daelemans D, Imamura H, Devlieger R, Rider M, Van Veldhoven PP, Schuit F, Bartrons R,

Hofkens J, Fraisl P, Telang S, Deberardinis RJ, Schoonjans L, Vinckier S, Chesney J, Gerhardt H, Dewerchin M, Carmeliet P. Role of pfkfb3-driven glycolysis in vessel sprouting. *Cell*. 2013;154:651-663

25. Doddaballapur A, Michalik KM, Manavski Y, Lucas T, Houtkooper RH, You X, Chen W, Zeiher AM, Potente M, Dimmeler S, Boon RA. Laminar shear stress inhibits endothelial cell metabolism via klf2-mediated repression of pfkfb3. *Arteriosclerosis, thrombosis, and vascular biology*. 2015;35:137-145

26. Wang S, Iring A, Strilic B, Albarran Juarez J, Kaur H, Troidl K, Tonack S, Burbiel JC, Muller CE, Fleming I, Lundberg JO, Wettschureck N, Offermanns S. P2y2 and gq/g11 control blood pressure by mediating endothelial mechanotransduction. *The Journal of clinical investigation*. 2015;125:3077-3086

27. Jones R, Baker MB, Weber M, Harrison DG, Bao G, Searles CD. Molecular beacons can assess changes in expression and 3'-polyadenylation of human enos mrna. *American journal of physiology. Cell physiology*. 2009;296:C498-504

28. Budas G, Costa HM, Jr., Ferreira JC, Teixeira da Silva Ferreira A, Perales J, Krieger JE, Mochly-Rosen D, Schechtman D. Identification of epsilonpkc targets during cardiac ischemic injury. *Circulation journal : official journal of the Japanese Circulation Society*. 2012;76:1476-1485

29. Mayr M, Liem D, Zhang J, Li X, Avliyakulov NK, Yang JI, Young G, Vondriska TM, Ladroue C, Madhu B, Griffiths JR, Gomes A, Xu Q, Ping P. Proteomic and metabolomic analysis of cardioprotection: Interplay between protein kinase c epsilon and delta in regulating glucose metabolism of murine hearts. *Journal of molecular and cellular cardiology*. 2009;46:268-277

30. Koh W, Sachidanandam K, Stratman AN, Sacharidou A, Mayo AM, Murphy EA, Cheresh DA, Davis GE. Formation of endothelial lumens requires a coordinated pkcepsilon-, src-, pak- and raf-kinase-dependent signaling cascade downstream of cdc42 activation. *Journal of cell science*. 2009;122:1812-1822

31. Rask-Madsen C, King GL. Differential regulation of vegf signaling by pkc-alpha and pkc-epsilon in endothelial cells. *Arteriosclerosis, thrombosis, and vascular biology*. 2008;28:919-924

32. Li R, Jen N, Wu L, Lee J, Fang K, Quigley K, Lee K, Wang S, Zhou B, Vergnes L, Chen YR, Li Z, Reue K, Ann DK, Hsiai TK. Disturbed flow induces autophagy, but impairs autophagic flux to perturb mitochondrial homeostasis. *Antioxid Redox Signal*. 2015;23:1207-1219

33. Subramaniam SR, Vergnes L, Franich NR, Reue K, Chesselet M-F. Region specific mitochondrial impairment in mice with widespread overexpression of alpha-synuclein. *Neurobiology of Disease*. 2014;70:204-213

34. TeSlaa T, Teitell MA. Techniques to monitor glycolysis. *Methods Enzymol*. 2014;542:91-114

35. Fiehn O, Wohlgemuth G, Scholz M, Kind T, Lee do Y, Lu Y, Moon S, Nikolau B. Quality control for plant metabolomics: Reporting msi-compliant studies. *The Plant journal : for cell and molecular biology*. 2008;53:691-704

36. Lee J, Packard RR, Hsiai TK. Blood flow modulation of vascular dynamics. *Curr Opin Lipidol*. 2015;26:376-383

37. Wu M, Neilson A, Swift AL, Moran R, Tamagnine J, Parslow D, Armistead S, Lemire K, Orrell J, Teich J, Chomicz S, Ferrick DA. Multiparameter metabolic analysis reveals a close link between attenuated mitochondrial bioenergetic

function and enhanced glycolysis dependency in human tumor cells. *American journal of physiology. Cell physiology*. 2007;292:C125-136

38. Schoors S, De Bock K, Cantelmo AR, Georgiadou M, Ghesquiere B, Cauwenberghs S, Kuchnio A, Wong BW, Quaegebeur A, Goveia J, Bifari F, Wang X, Blanco R, Tembuyser B, Cornelissen I, Bouche A, Vinckier S, Diaz-Moralli S, Gerhardt H, Telang S, Cascante M, Chesney J, Dewerchin M, Carmeliet P. Partial and transient reduction of glycolysis by pfkfb3 blockade reduces pathological angiogenesis. *Cell Metab*. 2014;19:37-48

39. Guo D, Chien S, Shyy JY. Regulation of endothelial cell cycle by laminar versus oscillatory flow: Distinct modes of interactions of amp-activated protein kinase and akt pathways. *Circulation research*. 2007;100:564-571

40. Jalali S, Li YS, Sotoudeh M, Yuan S, Li S, Chien S, Shyy JY. Shear stress activates p60src-ras-mapk signaling pathways in vascular endothelial cells. *Arteriosclerosis, thrombosis, and vascular biology*. 1998;18:227-234

41. Novellasdemunt L, Tato I, Navarro-Sabate A, Ruiz-Meana M, Mendez-Lucas A, Perales JC, Garcia-Dorado D, Ventura F, Bartrons R, Rosa JL. Akt-dependent activation of the heart 6-phosphofructo-2-kinase/fructose-2,6-bisphosphatase (pfkfb2) isoenzyme by amino acids. *The Journal of biological chemistry*. 2013;288:10640-10651

42. Painter RM, Pearson DM, Waymouth RM. Selective catalytic oxidation of glycerol to dihydroxyacetone. *Angewandte Chemie (International ed. in English)*. 2010;49:9456-9459

43. Kang M, Walker JW. Protein kinase c delta and epsilon mediate positive inotropy in adult ventricular myocytes. *Journal of molecular and cellular cardiology*. 2005;38:753-764

44. Dorn GW, 2nd, Mochly-Rosen D. Intracellular transport mechanisms of signal transducers. *Annual review of physiology*. 2002;64:407-429

45. Kumar S, Hedges SB. A molecular timescale for vertebrate evolution. *Nature*. 1998;392:917-920

46. Sedmera D, Reckova M, deAlmeida A, Sedmerova M, Biermann M, Volejnik J, Sarre A, Raddatz E, McCarthy RA, Gourdie RG, Thompson RP. Functional and morphological evidence for a ventricular conduction system in zebrafish and xenopus hearts. *American journal of physiology. Heart and circulatory physiology*. 2003;284:H1152-1160

47. Milan DJ, Jones IL, Ellinor PT, MacRae CA. In vivo recording of adult zebrafish electrocardiogram and assessment of drug-induced qt prolongation. *American journal of physiology. Heart and circulatory physiology*. 2006;291:H269-273

48. Kulkeaw K, Sugiyama D. Zebrafish erythropoiesis and the utility of fish as models of anemia. *Stem Cell Research & Therapy*. 2012;3:55-55

49. Chu CY, Cheng CH, Chen GD, Chen YC, Hung CC, Huang KY, Huang CJ. The zebrafish erythropoietin: Functional identification and biochemical characterization. *FEBS letters*. 2007;581:4265-4271

50. Ma J, Luo Y, Sevag Packard RR, Ma T, Ding Y, Abiri P, Tai YC, Zhou Q, Shung KK, Li R, Hsiai T. Ultrasonic transducer-guided electrochemical impedance spectroscopy to assess lipid-laden plaques. *Sens Actuators B Chem*. 2016;235:154-161

51. Packard RR, Zhang X, Luo Y, Ma T, Jen N, Ma J, Demer LL, Zhou Q, Sayre JW, Li R, Tai YC, Hsiai TK. Two-point stretchable electrode array for endoluminal electrochemical impedance spectroscopy measurements of lipid-laden atherosclerotic plaques. *Ann Biomed Eng*. 2016;44:2695-2706

52. Cao H, Yu F, Zhao Y, Scianmarello N, Lee J, Dai W, Jen N, Beebe T, Li R, Ebrahimi R, Chang DS, Mody FV, Pacella J, Tai YC, Hsiai T. Stretchable electrochemical impedance sensors for intravascular detection of lipid-rich lesions in new zealand white rabbits. *Biosens Bioelectron*. 2014;54:610-616

53. Jen N, Yu F, Lee J, Wasmund S, Dai X, Chen C, Chawareeyawong P, Yang Y, Li R, Hamdan MH, Hsiai TK. Atrial fibrillation pacing decreases intravascular shear stress in a new zealand white rabbit model: Implications in endothelial function. *Biomechanics and modeling in mechanobiology*. 2013;12:735-745

54. Yu F, Lee J, Jen N, Li X, Zhang Q, Tang R, Zhou Q, Kim ES, Hsiai TK. Elevated electrochemical impedance in the endoluminal regions with high shear stress: Implication for assessing lipid-rich atherosclerotic lesions. *Biosens Bioelectron*. 2013;43:237-244

55. Lee J, Fei P, Sevag Packard RR, Kang H, Xu H, Baek KI, Jen N, Chen J, Yen H, Kuo CC, Chi NC, Ho CM, Li R, Hsiai TK. 4-dimensional light-sheet microscopy to elucidate shear stress modulation of cardiac trabeculation. *The Journal of clinical investigation*. 2016;126:3158

56. Takabe W, Li R, Ai L, Yu F, Berliner JA, Hsiai TK. Oxidized low-density lipoprotein-activated c-jun nh2-terminal kinase regulates manganese superoxide dismutase ubiquitination: Implication for mitochondrial redox status and apoptosis. *Arteriosclerosis, thrombosis, and vascular biology*. 2010;30:436-441

57. Simmons RD, Kumar S, Jo H. The role of endothelial mechanosensitive genes in atherosclerosis and omics approaches. *Arch Biochem Biophys*. 2016;591:111-131

58. Go YM, Kim CW, Walker DI, Kang DW, Kumar S, Orr M, Uppal K, Quyyumi AA, Jo H, Jones DP. Disturbed flow induces systemic changes in metabolites in mouse plasma: A metabolomics study using apoe(-)/(-) mice with partial carotid ligation. *Am J Physiol Regul Integr Comp Physiol*. 2015;308:R62-72